

MODELING RUNOFF LEVELS OVER IMPERVIOUS SURFACES IN THE LAKE  
TAHOE BASIN USING VARYING DATA RESOLUTION

By

Celeste E. Melosh

A Thesis Presented to

The Faculty of Humboldt State University

In Partial Fulfillment of the Requirements for the Degree

Master of Science in Natural Resources: Forestry Watershed and Wildland Sciences

Committee Membership

Dr. Andrew Stubblefield, Committee Chair

Dr. Mahesh Rao, Committee Member

Dr. Margaret Lang, Committee Member

Dr. Allison O'Dowd, Graduate Coordinator

December 2015

## ABSTRACT

### MODELING RUNOFF LEVELS OVER IMPERVIOUS SURACES IN THE LAKE TAHOE BASIN USING VARYING DATA RESOLUTION

Celeste E. Melosh

Directly connected impervious areas collect and deliver unfiltered runoff to modified and impacted urban waterways. Modeling flow over the landscape is an effective method of observing drainage patterns and predicting peak runoff levels. Model improvements can increase our ability to identify key areas with high runoff and pollutant output. This is a crucial issue in the Lake Tahoe Basin where lakeshore urban development has increased and lake clarity has been declining for years. This study aims to evaluate an integrated LiDAR and GIS-based modeling approach that uses a fine-scaled ground surface and impervious surface connectivity to predict the runoff volumes in the Lake Tahoe Basin.

This study produced two rainfall-runoff models for each of three small urban basins in South Lake Tahoe with various levels of impervious surface. A land use classification was generated using NAIP color infrared and LiDAR data. In addition to land use, hydrological characteristics, basins and drainages derived from LiDAR and 10-meter digital elevation models were used in the models. The US Army Corps of Engineers Hydrologic Engineering Center's Hydrologic Modeling System version 3.5 was used to model runoff peaks and volumes for 10-meter and LiDAR derived inputs for

each site. The flow modeled for LiDAR inputs was compared to flow modeled with lower-resolution 10-meter layers as well as observed monitoring data.

Flow was successfully modeled for most storms; producing runoff that mimicked observed flow patterns. The most common errors found were lower modeled peak flows in thunderstorms, modeled volumes inconsistent with observed volumes during winter storms and periods of flow found in either the modeled or observed data but not both. In general, the LiDAR and 10-meter models produced similar flow outputs to each other. The 10-meter models produced slightly better peak flow values while the LiDAR produced better volume outputs. However, these differences were small and fell within the margin of error.

Although the models did not benefit from the added data resolution, LiDAR will still prove to be a valuable management tool. The LiDAR flow network analysis for this study demonstrates an impressive increase in the visualization of micro scale flow patterns across the urban landscape. This improved ability to pinpoint where and over what surface water flows as it makes its way from the sky to the stream will aid urban basin managers in identifying key pollutant inputs and placing retention sites and diversions.

## ACKNOWLEDGEMENTS

Thank you to J. Shane Romsos from the Tahoe Regional Planning Agency for providing the LiDAR data used in this study. Thank you to Dr. Alan Heyvaert of the Desert Research Institute for providing the observed flow and precipitation data for the stormwater basin sites used. Thank you to Robert Erlich from the South Lake Tahoe Public Works Engineering Division for providing access to and help with city stormwater and urban basin maps. Thank you to my committee, Dr. Andrew Stubblefield, Dr. Mahesh Rao, and Dr. Margaret Lang, for your time, effort and advice. Thank you to all my friends and family that provided technical, editorial and emotional support throughout the process.

## TABLE OF CONTENTS

ABSTRACT.....	ii
ACKNOWLEDGEMENTS.....	iv
LIST OF TABLES.....	viii
LIST OF FIGURES.....	x
LIST OF APPENDICES.....	xi
INTRODUCTION.....	1
Objectives.....	3
Hypotheses.....	4
LITERATURE REVIEW.....	5
Effect of Urbanization on Streams.....	5
Impervious Surfaces.....	8
Remote Sensing.....	10
Digital Elevation Models.....	12
Stream Network and Flow Modeling.....	13
Hydrological Modeling.....	14
HEC–HMS Model.....	15
METHODS.....	22
Study Site.....	22
Classification.....	27
Image Processing.....	27
Land-Use Classification.....	31
Accuracy Assessment.....	37

Terrain Processing.....	37
HEC-HMS Model.....	39
Model Setup.....	43
Model Methods and Parameter Calculations .....	44
Storm Selection.....	48
Optimization .....	49
Model Evaluation.....	50
RESULTS .....	52
Land-Use Analysis .....	52
Classification.....	52
Accuracy Assessment .....	56
Flow Analysis.....	58
Outlet Location .....	58
Flow Patterns and Basin Characteristics.....	58
Modeling .....	63
Model Optimization.....	63
Model Outputs .....	69
Individual Storms.....	70
DISCUSSION.....	78
Classification .....	78
Flow Analysis.....	79
Flow Patterns .....	81
Basin Differences.....	82

Modeling .....	84
10-meter vs. LiDAR.....	84
Individual Storm Assessment .....	86
Sources of Error .....	99
CONCLUSIONS.....	102
LITERATURE CITED .....	106
Appendix A.....	111
Appendix B .....	113
Appendix C .....	121

## LIST OF TABLES

Table 1: SCS soil groups and infiltration rates .....	17
Table 2: Description, source and analytical use of data sets used in the study.....	29
Table 3: Georeferencing details, control points, RMS error and methods used for the NAIP imagery .....	30
Table 4: Initial classes, number of training polygons and the number of pixels used for the supervised classification of the South Lake Tahoe .....	33
Table 5: Road classes, estimated widths and buffer values used in the supervised classification .....	36
Table 6: Albers Equal Area Conic projection values used in the HEC-HMS model .....	38
Table 7: Distance in meters between pourpoints used for basin delineation and the GPS location identified during on-site drainage outlet identification.....	40
Table 8: Model attributes, calculation methods and their inputs .....	43
Table 9: Distance in meters between model basin centroids and the associated precipitation gage.....	44
Table 10: Methods and parameters used for HEC-HMS models .....	45
Table 11: Maximum and minimum parameter values in HEC-HMS optimization.....	50
Table 12: Area and percentage of basin for each class in the supervised classification for study sites.....	55
Table 13: Accuracy assessment for all classes in the supervised classification .....	57
Table 14: Accuracy assessment for pervious and impervious classes combined from supervised classification .....	57
Table 15: Differences in values determined with outlet coordinates reported by DRI/TGR and those recorded in the field .....	58
Table 16: Total drainage length per square meter for each site .....	59

Table 17: 10-meter and LiDAR basin attributes including area, drainage length and density, slope calculated as percent rise, and percent DCIA .....	62
Table 18: Percent error for peak flow rates and volume outputs for LiDAR and 10-meter model outputs.....	65
Table 19: Nash-Sutcliffe Efficiency $E$ and $E_{ln}$ values for models .....	67
Table 20: Maximum and minimum daily temperature for relevant dates recorded at South Lake Tahoe Airport.....	91

## LIST OF FIGURES

Figure 1: Diagram showing the thesis concept, including model inputs and output .....	4
Figure 2: Impervious surface cover reduces infiltration and evapotranspiration rates and increase overland runoff levels .....	7
Figure 3: Hypothetical hydrographs for developed and undeveloped streams. Urban stream has a higher peak and earlier response time than undeveloped stream .....	7
Figure 4: Highest hit surface model derived from LiDAR point cloud. Building rooftops, trees and even cars are easily distinguishable .....	11
Figure 5: Hillshades of LiDAR and 10-meter ground surface models at site SY and O3 located in South Lake Tahoe, CA .....	13
Figure 6: Site location overview map .....	23
Figure 7: Average monthly temperatures and precipitation for South Lake Tahoe Airport station from 1968 to 2010 .....	24
Figure 8: Study basins located in South Lake Tahoe include South Lake Tahoe Y, Glorene and Eighth and Osgood Ave .....	26
Figure 9: Outline of processing steps used for classification and model analysis .....	27
Figure 10: Terrain processing flow chart depicting methods used to create drainage lines, basins and other necessary layers for the HEC-HMS model .....	39
Figure 11: LiDAR and 10-meter study site basins overlaid on urban storm water drainage map from the South Lake Tahoe Department of Transportation .....	42
Figure 12: Unsupervised classification at study sites South Lake Tahoe Y, Osgood Ave and Glorene and Eighth showing LiDAR derived basins, South Lake Tahoe, CA .....	53
Figure 13: Final supervised classification for study sites South Lake Tahoe Y, Osgood Ave and Glorene and Eighth showing derived basins and pourpoints used .....	54
Figure 14: Flow lines derived from LiDAR and 10-meter DEMs .....	60
Figure 15: LiDAR and 10-meter DEM derived flow patterns over classified image near site SY .....	61

## LIST OF APPENDICES

Appendix A: Diagram and threshold rules applied with the Knowledge Engineer to improve supervised classification .....	111
Appendix B: Initial and optimized parameters for HEC-HMS model methods .....	113
Appendix C: Precipitation, observed and modeled hydrographs, peak flow rates and volume outputs for all storm events .....	121

## INTRODUCTION

In recent decades humans have had a dramatic effect on the environment and its processes (Wagener et al., 2010). Hydraulic and human systems are intrinsically linked and although water quality is affected by numerous natural influences (soil type, vegetation, climate, and geology), the anthropogenic influences are usually more lasting and damaging (Coats et al., 2008). Land-use, especially near a stream, river or lake, has a large influence on which pollutants reach the water (Paul and Meyer, 2001). Urban areas have a large ecological footprint despite their relatively small sizes and are second only to agriculture as a cause of stream impairment (Paul and Meyer, 2001). A mechanistic understanding of the links between urban land-use and stream degradation is essential to the implementation of restoration and policy (Paul and Meyer, 2001; Yang and Liu, 2005).

Impervious surfaces are often considered synonymous to urbanization because they play such an influential role in how urban environments affect their surroundings (Coats et al., 2008; Lee and Heaney, 2003; Paul and Meyer, 2001). Directly connected impervious area (DCIA) is hydraulically connected to the stream network which means runoff, and therefore sediments and pollutants from these surfaces reach the streams without interruption (Alley and Veenhuis, 1983; Coats et al., 2008; Lee and Heaney, 2003). Modeling hydraulic flow over a landscape is a cost- and time-effective method of observing drainage patterns and predicting pollutant and sediment loadings (Tarboton and

Ames, 2001). Improvements in the models through high-resolution elevation data could prove useful for managers to identify areas with the greatest pollutant output.

Model improvement is particularly important in areas with known water quality issues, such as Lake Tahoe. Over the past 43 years there has been a noted decline in water clarity in Lake Tahoe from 30.5m (100ft) depth (measured in 1968) of clarity to its record low of 19.5m (64.1ft) (measured in 1997) (TERC, 2011). Since then, lake has improved slightly and averages around 21.3 m (70ft). Lake Tahoe water clarity is being affected by the loss of wetlands that serve as retention for sediments, increased erosion from urban development in steep locals, septic tank and sewage line discharge, and the runoff of accumulated sediments and chemicals from streets and other impervious surfaces (Forney et al., 2001; TRPA, 1997). The lake's popularity as a tourist location makes it an iconic location in the fight for environmental restoration. Knowing which surfaces influence Tahoe's streams the most will allow managers to better strategize methods of reducing pollutant loading to the lake. This study attempts to produce a fine-scaled surface model of small urban basins at risk of sediment and pollutant loading by integrating Light Detection and Ranging (LiDAR) and Geographical Information Science (GIS) data. Furthermore it attempts to determine how the resolution of input data into the HEC-HMS model affects runoff values at basin outlets by comparing the high-resolution LiDAR inputs to those produced with a 10-meter digital elevation model.

## Objectives

The main objective of this study is to evaluate an integrated LiDAR and GIS-based modeling approach that uses a fine-scaled ground surface and impervious surface connectivity to predict the runoff volume in the Lake Tahoe Basin. A diagram depicting the thesis concept design can be found in Figure 1. To complete and assess this model, the following objectives were achieved.

- Map impervious surface and other ground cover types of the study area using integrated LiDAR, multispectral data and GIS techniques.
- Evaluate the surface layer accuracy with field ground-truthing data.
- Use a fine-scaled LiDAR DEM for the area of interest to map hydrologic flow over the area of interest.
- Use the impervious surface layer, the DEM and other GIS data to identify the spatial extent and location of DCIA.
- Perform a hydrological assessment of the areas of interest in the Lake Tahoe Basin using the Hydrologic Engineering Center's Hydrologic Modeling System (HEC-HMS).
- Compare the runoff histograms, peaks and volumes from the HEC-HMS LiDAR models and 10-meter DEM models with field data to evaluate the effect of LiDAR data on model accuracy.

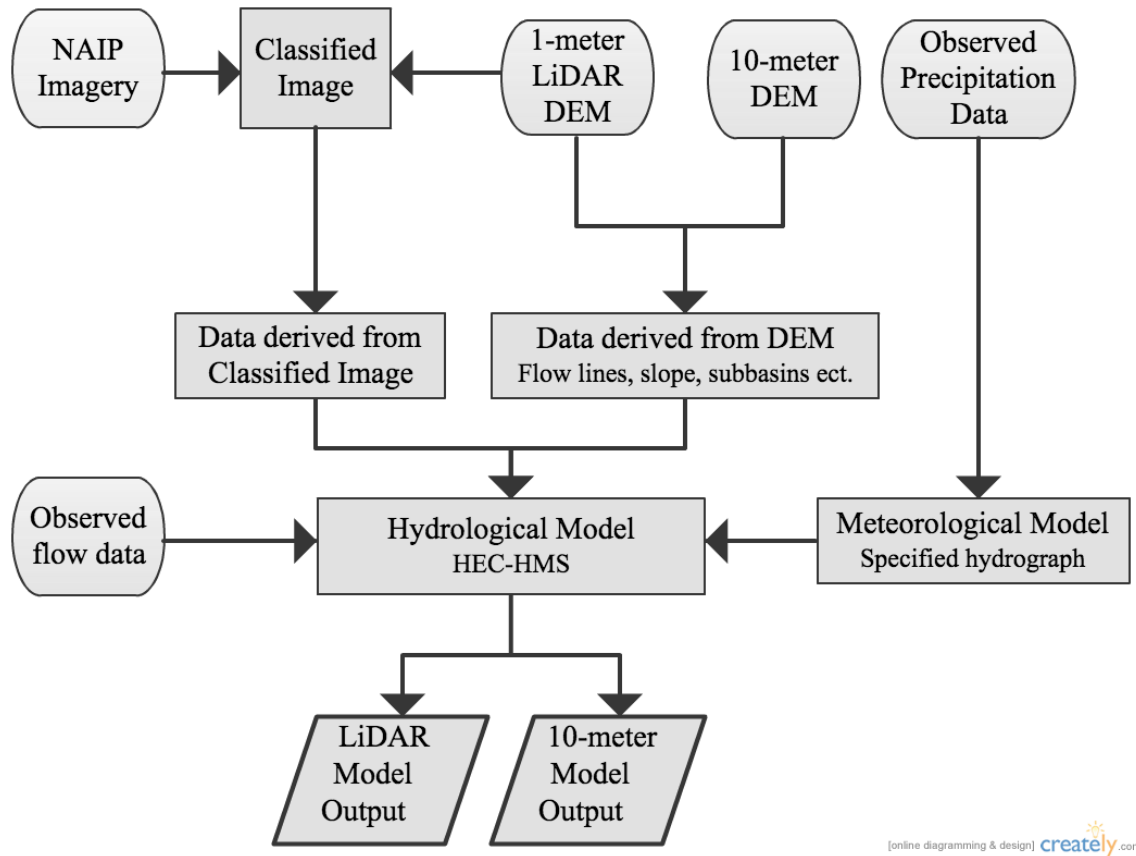


Figure 1: Diagram showing the thesis concept, including model inputs and output.

### Hypotheses

An integrated method using LiDAR, multispectral imagery and GIS data can be used to develop accurate terrain models, hydrologic routing and DCIA layers for Lake Tahoe basin. Improved precision of the DCIA data in the HEC-HMS model will improve the accuracy of the model's representation of runoff.

## LITERATURE REVIEW

### Effect of Urbanization on Streams

Urbanization alters streams chemically, biologically, and physically (Coats et al., 2008; Paul and Meyer, 2001). Urban streams have higher chemical levels, pesticides and heavy metals than non-urban streams (Coats et al., 2008; Paul and Meyer, 2001).

Amongst the chemicals, nitrogen and phosphorous levels are particularly important because they naturally limit growth within an ecosystem (Naiman and Bilby, 1998; Paul and Meyer, 2001). Increased nitrogen and phosphorous levels can cause algae blooms that cover the surface of the water, reduce light penetration, and decrease dissolved oxygen levels. Pesticide levels are often higher in urban streams than in streams associated with agricultural fields (Paul and Meyer, 2001). Increases in these chemicals stem mostly from non-point sources, such as fertilized lawns, wastewater treatment, streets and other impervious surfaces (Coats et al., 2008; Paul and Meyer, 2001).

Biological and ecological effects of urbanization on streams are less studied. Bacteria and algae decrease in diversity and increase in abundance with urbanization (Paul and Meyer, 2001). Invertebrate species, which are sometimes used as indicator species for ecosystem health, decrease in diversity and abundance (EPA, 2011; Paul and Meyer, 2001). Even low urbanization levels (0 – 5 %) can cause the loss of sensitive fish species while urbanization greater than 15 percent can cause toxicity, organic enrichment

and severe degradation of fish species (Klein, 1979; Paul and Meyer, 2001). Species homogeneity weakens the integrity of the ecosystem (Naiman and Bilby, 1998).

Physical characteristics of the water and geomorphological characteristics of the stream channel are defined by the flow regime (Konrad and Booth, 2005). Changes to the flow regime affect ecosystem health by changing disturbance patterns, sediment levels and water temperature. Disturbance patterns maintain diversity by preventing the total elimination of inferior competitor species (Connell, 1978). Changes to the timing or rate of high- and low-flows affect the diversity and abundance of lotic species by changing the convergence with the appropriate point in the species life-histories (Connell, 1978; Konrad and Booth, 2005; Power et al., 1988; Resh et al., 1988) Disturbance frequencies and timings are impacted by runoff type and amount.

Overland runoff increases rapidly with an increase in impervious urban surfaces (Figure 2) (Paul and Meyer, 2001). Water that was once intercepted by vegetation or stored in the soil now travels rapidly into the stream network (Konrad and Booth, 2005). During storms, stream levels rise and fall more rapidly and reach a higher peak flow than in non-urban streams, producing flashy floods and potentially lowering base-flow (Figure 3) (Konrad and Booth, 2005; Lee and Heaney, 2003; Paul and Meyer, 2001; Roy and Shuster, 2009). There are shorter periods between disturbances and an increase in the disturbance season (Konrad and Booth, 2005).

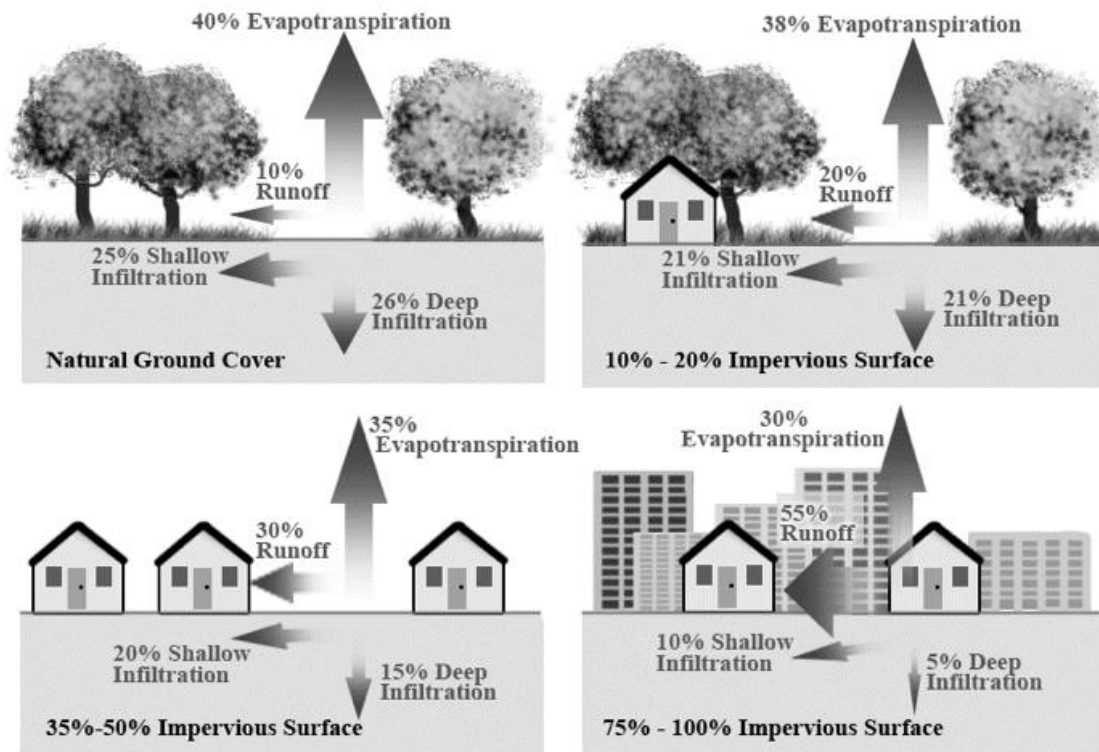


Figure 2: Impervious surface cover reduces infiltration and evapotranspiration rates and increase overland runoff levels. Figure modified from the EPA's website (EPA, 2008).

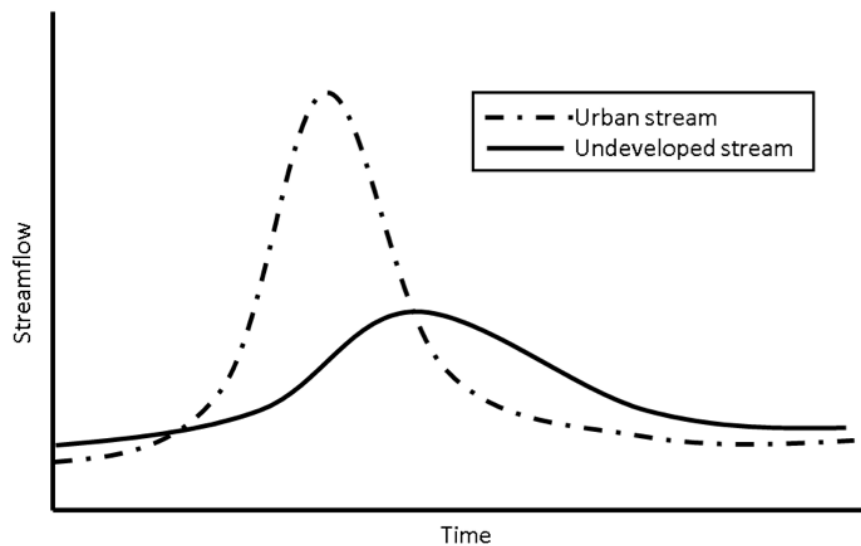


Figure 3: Hypothetical hydrographs for developed and undeveloped streams. Urban stream has a higher peak and earlier response time than undeveloped stream. Figure modified from EPA's website (EPA, 2012).

Sediment levels also can change as a result of urbanization. The type and amount of sediments found in the stream is altered depending on the type of land-use (Paul and Meyer, 2001). Additional sediments are washed into the stream from roads and construction sites (Paul and Meyer, 2001). Ideal fish spawning sites consist of small clean gravel reaches but the addition of fine sediments can clog up gravels and destroy the spawning sites (Naiman and Bilby, 1998). Even temporary increases in sediment levels can cause aggradation, flooding, erosion, and the eventual re-stabilization of the stream channel in a new shape, often with a narrower channel (Paul and Meyer, 2001). Narrower channels decrease habitat heterogeneity and diminish available refugia for species (Naiman and Bilby, 1998).

Water temperatures can be altered through changes in stream discharge or through the removal of riparian vegetation. Higher water temperature can be detrimental to some fish species during crucial points in their life history. Vegetation removal also causes a reduction in the heterogeneity of fish habitat and can decrease nutrient availability within the stream (Naiman and Bilby, 1998; Paul and Meyer, 2001).

### Impervious Surfaces

Impervious surfaces are areas where water cannot be absorbed into the ground and instead flows overland towards the stream network. Imperviousness is one of the main reasons urban areas have such a large influence on their surrounding environments (Coats et al., 2008; Lee and Heaney, 2003; Paul and Meyer, 2001). Impervious surfaces, lot-density and road density were the three most important factors increasing suspended

sediments, nitrogen and phosphorus in urban streams in the Tahoe Basin (Coats et al., 2008; Paul and Meyer, 2001).

The connectedness of these impervious areas to the stream network also plays a large role. Gutters and storm drains often connect impervious area directly to the stream. Directly connected impervious area (DCIA) merits more focus than total impervious area (TIA) because it is the primary contributor of runoff for smaller storms, the primary concern for water quality and is responsible for the majority of stream alteration in urban areas (Lee and Heaney, 2003; Roy and Shuster, 2009). It is also highly correlated with turbidity, algal levels, fish and invertebrate assemblages (Roy and Shuster, 2009). Impervious surfaces, and especially DCIA, are a proxy for vehicle emissions, the application of traction sands, oils, animal wastes, fertilizers, and accelerated decomposition of the forest floor due to increased foot and vehicle traffic, all of which affect stream quality (Coats et al., 2008).

Additionally, DCIA is strongly correlated to runoff levels (Corbett et al., 1997; Lee and Heaney, 2003). Runoff doubles with an increase in directly connected impervious surfaces of only 10 to 20 percent (Paul and Meyer, 2001). It triples with 35 to 50 percent increase and is increased by a factor of five with a 70 to 100 percent increase (Figure 2) (Paul and Meyer, 2001). Unfortunately, quantifying DCIA without labor-intensive fieldwork is difficult.

Due to the added difficulty in identifying DCIA from remote sensing data, most studies and models attempt to associate it with TIA to generate an estimate of DCIA (Alley and Veenhuis, 1983; Lee and Heaney, 2003; Roy and Shuster, 2009). One

example is the empirical relationship between TIA and DICA developed by Alley and Veenhuis (1983):

$$DCIA = 0.15(TIA)^{1.41} \quad [ 1 ]$$

This formula was developed for a highly urban area in Denver and does not necessarily transfer to other dissimilar areas. These ratios do not estimate DCIA accurately, especially in residential areas, or areas of mixed land-use (Alley and Veenhuis, 1983; Lee and Heaney, 2003; Roy and Shuster, 2009). In residential areas spatial analysis estimates of impervious surfaces have shown two to three percent more predicted than actual impervious area (Lee and Heaney, 2003). Additionally, with an increase in land-use intensity, DCIA increases more rapidly than TIA, which can cause an underestimation of DCIA in high-intensity land-use areas by up to six percent (Alley and Veenhuis, 1983). Field surveys and outside GIS data are time consuming but can help to improve accurate assessment of DCIA (Roy and Shuster, 2009).

### Remote Sensing

Remote sensing and analysis is a cost-effective way of identifying urban growth on a large scale (Yang and Liu, 2005). The evolution of data acquisition and processing capabilities has allowed automated classifications with significant accuracy (Yang and Liu, 2005). Outside data sources, such as GIS, compliment remotely acquired images in the classification process (Greenhill et al., 2003). Incorporating high-resolution data is more effective in improving classifications than using a combination of lower resolution

data (Lu and Weng, 2005). Therefore the more recent access to high resolution Light Detection and Ranging (LiDAR) data could improve classification accuracy even more.

Although LiDAR is still a relatively young technology, it has already proven to be very useful in a variety of forestry applications (Andersen et al., 2006; Reutebuch et al., 2005). Figure 4 has an example of a highest hit surface model derived from a LiDAR point cloud dataset. LiDAR is not limited to ground or canopy modeling. It has been used to analyze streambeds (Allouis et al., 2010), make canopy structure measurements (Andersen et al., 2005), model potential forest fire behavior (Andersen et al., 2005) and create high-resolution digital elevation maps despite canopy cover (Andersen et al. 2006). LiDAR's high-resolution 3D data could prove to be an excellent aid in the identification and modeling of impervious surfaces.

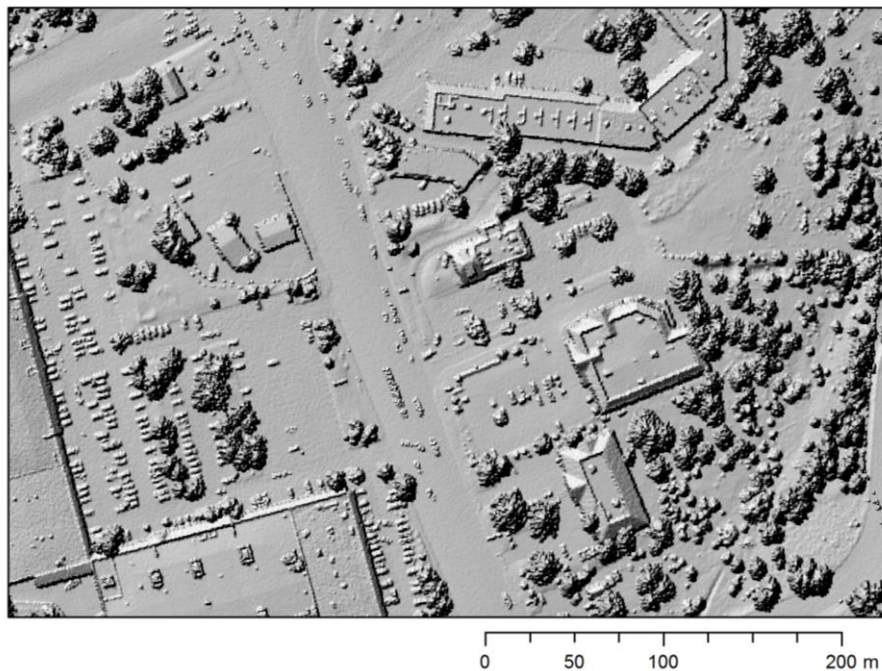


Figure 4: Highest hit surface model derived from LiDAR point cloud. Building rooftops, trees and even cars are easily distinguishable.

## Digital Elevation Models

Digital elevation models (DEMs) are useful for many purposes such as the extraction of river networks or the delineation of watersheds (Li and Wong, 2010). High DEM resolution provides superior results in the extraction of river networks and results in steeper slopes and more simulated runoff in models (Li and Wong, 2010). They are most commonly generated from USGS elevation datasets (Li and Wong, 2010).

LiDAR is being used to create DEMs with improved horizontal and vertical resolutions (French, 2003; Li and Wong, 2010). Examples of LiDAR and 10-meter DEMs are displayed using hillshades in Figure 5. LiDAR averages high-density elevation data for each point while USGS elevation averages are based on a few widespread survey points (French, 2003). Therefore, even with resampling done to mitigate the large computational time LiDAR datasets require, LiDAR can improve elevation data (Andersen et al., 2006; French, 2003). Accuracy can be further improved by using a supervised classification and filtering routine to remove buildings and vegetation without losing ground points (Jones et al., 2007).

LiDAR can create accurate topography at a resolution close to the limits of current models and is particularly useful in areas where topographic relief is small (French, 2003). However, there is a threshold data density for the desired spatial scale under which LiDAR data remains accurate and usable (Andersen et al. 2006). The study of low relief landscapes is less sensitive to resolution changes than the study of micro-scale topographic influences on landscapes (Andersen et al., 2006; Li and Wong, 2010).

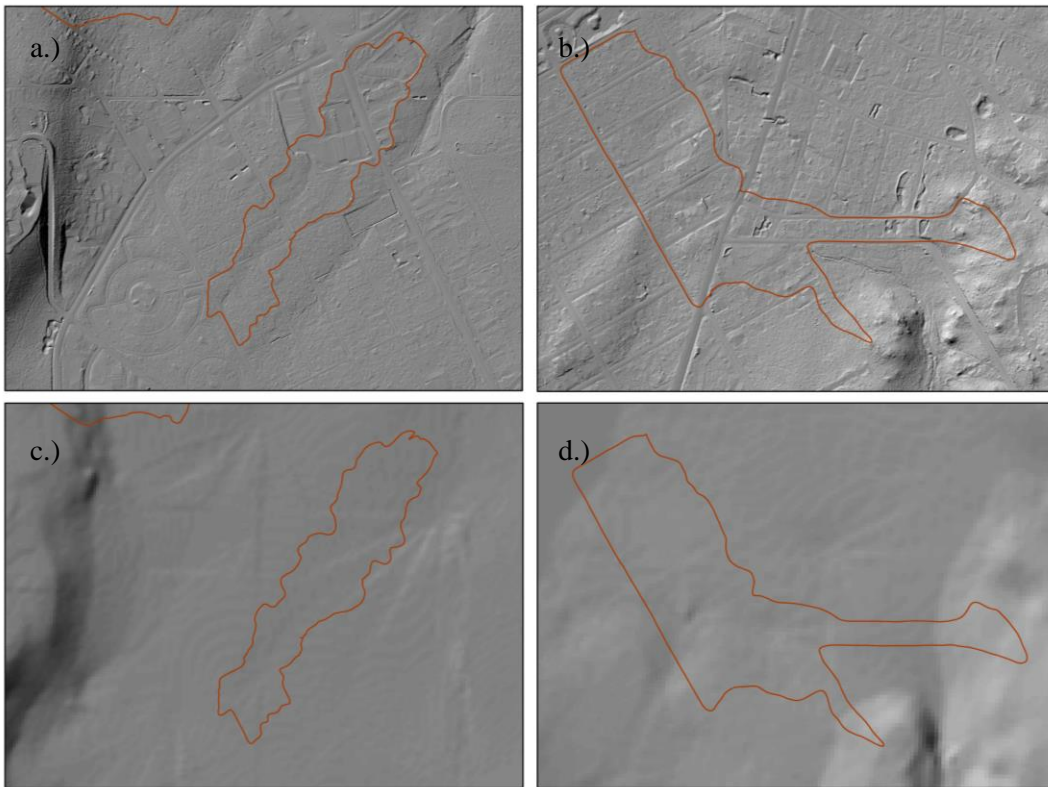


Figure 5: Hillshades of LiDAR (a and b) and 10-meter (c and d) ground surface models at site SY and O3 located in South Lake Tahoe, CA. LiDAR derived basins included for comparison purposes.

### Stream Network and Flow Modeling

The modeling of stream networks and flow paths has a variety of applications. Erosion and the transport of other particulates can be related to water flow over a hillslope (Cochrane and Glanagan, 1999). Stream networks with broad regional coverage help identify stream shape attributes useful for modeling various sediment, pollutant, exotic species and fire scenarios (Davies et al., 2007). This improves the selection of restoration sites and strategies (Davies et al., 2007). Furthermore, the network allows

rapid classification of channel slope and width over a large area (Davies et al., 2007). The model accuracy is affected by the methods used.

Traditional methods of modeling flow and generating stream networks use USGS topographic maps to manually estimate drainages for the region which results in analyst based inconsistencies and estimation errors (Davies et al., 2007). Additionally, the time and expenses involved make this method impractical to use on a regular basis (Davies et al., 2007). Since then, computers have become more commonly used and technological improvements have allowed for greater accuracy and less time consumption in the creation of network modeling.

Currently, the most common method of extracting river networks is through DEMs (Li and Wong, 2010). Higher resolution DEMs provide superior results in the extraction of river networks and thus should be used when site-specific analysis is required (Davies et al., 2007; Li and Wong, 2010). High-resolution LiDAR data also allows for the mapping of small channels and gullies, even beneath forest canopy (James et al. 2007). Standard DEMs lack the spatial resolution to map these small headwaters accurately and airborne photography is limited below dense forest cover making LiDAR coverage beneficial despite inaccuracies that arise due to low point density (James et al. 2007).

### Hydrological Modeling

There are several options and selection in choosing the best hydrologic model. Models can be event or continuous, lumped or distributed, empirical or conceptual and

measured- or fitted-parameter (HEC, 2000). Continuous models use long term precipitation data while event models use smaller, storm based events to predict outflow (HEC, 2000). In a lumped model the basin characteristics and rainfall are averaged within each basin (Kumar and Bhattacharjya, 2011). Distributed models used gridded precipitation and consider spatial variation explicitly (HEC, 2000). A distributed model should be used if there is a large variation in rainfall or other characteristics across the basin. In this case a lumped model will not provide accurate results basin (Kumar and Bhattacharjya, 2011). If variation within the basin is small, a lumped model will suffice.

An empirical model is built on observed inputs and outputs and does not try to mathematically represent the processes occurring in the system. In other words, the model is blind to the processes. A conceptual model uses a base of knowledge of watershed processes to predict outcomes (HEC, 2000). A measured-parameter model uses parameter values that can be determined either through direct observation or indirect calculations using observable values. A fitted-parameter model includes values that cannot be measured (HEC, 2000). This study uses lumped event based models that are empirical and uses fitted-parameters.

### **HEC–HMS Model**

This study uses the Hydrologic Engineering Center’s Hydrologic Modeling System 3.5 (HEC-HMS) to model drainage flow in study site basins. HEC-HMS combines a basin model with a meteorological model, control specifications and run options (Kumar and Bhattacharjya, 2011). The basin connectivity and physical

characteristics are stored in the basin model and the precipitation is stored in the meteorological model (Kumar and Bhattacharjya, 2011). Control specifications and run options control model timings (HEC, 2010). The modeling process itself uses four separate models to represent different components of the runoff process (Kumar and Bhattacharjya, 2011).

A runoff-volume or loss method model evaluates the amount of rainfall that is intercepted, infiltrated or converted into runoff (ASCE, 1996). The amount of infiltration depends largely on land use and soil capacity (Kumar and Bhattacharjya, 2011). HEC-HMS does not model vertical movement of water or water storage in the soil layers (Kumar and Bhattacharjya, 2011).

HEC-HMS allows the user to select among different runoff-volume models. For this study, the initial and constant method was chosen to model runoff-volume because it has a small number of parameters, is easy to set up, is used in many other studies, and is appropriate with a lack of detailed soil data (HEC, 2000). The initial and constant method has an initial loss value and a maximum potential loss rate that remains constant over time (HEC, 2000). The initial loss value represents interception, depression storage and the antecedent condition of the soil (HEC, 2000). Runoff starts after precipitation exceeds the initial loss value. The constant rate depends on the infiltration capacity of the soil type (Table 1) (HEC, 2000). In addition, land use is denoted as either pervious or directly connected impervious area (Kumar and Bhattacharjya, 2011). No loss calculations are implemented in areas denoted as DCIA and all precipitation occurring here becomes excess runoff (HEC, 2000).

Table 1: SCS soil groups and infiltration rates. Table from HEC-HMS Technical Reference manual (2000).

Soil Group	Description	Loss Rates (in/hr)
A	Deep sand, deep loess, aggregated silts	0.30 - 0.45
B	Shallow loess, sandy loam	0.15 - 0.30
C	Clay loams, shallow sandy loam, soils low in organic content, and soils usually high in clay	0.05 - 0.15
D	Soils that swell significantly when wet, heavy plastic clays and certain saline soils	0.00 - 0.05

The initial and constant loss method is a mature model used in many studies, some examples of these include Cunderlik and Simonovic (2007) Pistocchi and Mazzoli (2002) Yusop et al. (2007). It is easy to set up and uses a small number of parameters which keeps it simple (HEC, 2000). This is an appropriate model to use when there is a lack of detailed soil information (HEC, 2000). However it is difficult to apply to ungauged areas since there is no direct physical relationship between watershed characteristics and model parameters (HEC, 2000). Additionally, although the model predicts overall loss well, it is too simplistic to predict losses within an event.

The direct runoff or transform method uses the runoff values produced from the loss method and transports it across the landscape into the drainage system (HEC, 2000). It implicitly combines near surface flow and overland flow to model the direct runoff (Kumar and Bhattacharjya, 2011).

Many studies have used unit hydrographs as a transform method for models (HEC, 2000). A unit hydrograph establishes a link between excess precipitation and

runoff without having to go into detailed processes (HEC, 2000). A unit hydrograph depicts the basin outflow from one unit of direct runoff generated by uniform precipitation at a uniform rate within the basin over a specified amount of time (HEC, 2000). They have limited physical significance and instead are optimized through goodness-of-fit criteria (HEC, 2000).

The HEC-HMS also allows the user to select among several different transform models. For this study, Snyder's unit hydrograph method was selected because it is simple, has a small number of parameters, and has been used in many other studies. Snyder's unit hydrograph method uses lag time, total time and peak flow. For this method, lag time is considered the principle drainage basin characteristic (Snyder, 1938). The lag is the time between the center of the precipitation that produces surface runoff and the peak flow (Snyder, 1938). Hence, peak rate is expressed as a unit of lag. Lag time can be affected by the basin shape, topography, channel slope, stream density and channel storage (Snyder, 1938). This method should not be used on watersheds that produce multiple peaks for a single input of precipitation (HEC, 2000). Additionally, unit-hydrographs created for small storms with less than two inches of runoff should not be used for storms with more than 3 inches and vice-versa (Snyder, 1938). This method assumes that the lag time is constant for the basin, flow values are proportional to the total amount of surface runoff and match the unit-graph shape, and that most subsurface flow can be included with surface flow (Snyder, 1938). The Snyder's unit hydrograph study (1938) was conducted in a mountainous regions.

The baseflow method describes the flow occurring within the stream before the storm begins and generally relates to subsurface runoff entering streams from previous storms (HEC, 2000). The constant monthly method is the simplest baseflow method available (HEC, 2000). It is single user specified value for baseflow that can vary monthly usually estimated from empirical data for the basin. In large watersheds with groundwater contributions, baseflow can be a significant source of flow. However, in most urban channels and small streams baseflow contributions are minor or nonexistent.

Finally, once the excess runoff reaches the stream, a routing method is used to transport the water along the stream to the next subbasin and eventually the basin outlet. The lag method is the simplest routing method available in HEC-HMS. For this method outflow and inflow are equal; the hydrograph shape remains the same. The flow is simply delayed by a specified time (HEC, 2000). This method has been used widely in urban drainage channels (HEC, 2000).

### *Optimization*

Success of the model depends on the model calibration, which in turn depends on the technical capability of the model and the quality of the data (Kumar and Bhattacharjya, 2011). Optimization trials in HEC-HMS can be run using two local search algorithms, the Nelder-Mead simplex and univariate gradient (HEC, 2000). Local search functions can be divided further into gradient and direct methods (Madsen, 2000). Gradient search methods, like the univariate gradient method, use information on the gradient of the objective function as well as the information on its value (Madsen, 2000).

The univariate gradient search method evaluates a single parameter at a time locking other parameters while it works (Kumar and Bhattacharjya, 2011).

Direct search functions, like the Nelder-Mead simplex use only information on the objective function itself (Madsen, 2000). The Nelder-Mead simplex method evaluates all the parameters simultaneously and determines which should be adjusted (Kumar and Bhattacharjya, 2011). In this method, the least amount of information is kept at each state and no account of past positions is kept (Nelder and Mead, 1965). The only assumption made about the surface is that it is continuous and has a local minimum in the area of search (Nelder and Mead, 1965). When the hydrograph changes rapidly, the simplex does well in comparison with other methods. However it might not do so well in the neighborhood of a minimum, with less rapidly changing curves (Nelder and Mead, 1965). The simplex will converge even when it straddles two or more valleys (Nelder and Mead, 1965). However, like other minimization methods, it could produce a false minimum, converging on the local minimum rather than the global minimum (Kumar and Bhattacharjya, 2011; Nelder and Mead, 1965). The Nelder-Mead simplex method is popular and used in many studies (Barati, 2011; Lagarias et al., 1998; Madsen, 2000).

The purpose of the search algorithms is to find the best fit objective function and optimize the parameter values (Kumar and Bhattacharjya, 2011). The objective function is a mathematical tool that measures the goodness of fit between observed and modeled hydrographs (Kumar and Bhattacharjya, 2011). There are seven available objective functions in HEC-HMS are peak-weighted root mean square error, percent error in peak,

percent error in volume, root mean square log error, sum of absolute residuals, sum of squared residuals and time-weighted error (HEC, 2000; Kumar and Bhattacharjya, 2011).

Hydrological modeling and calibration has four main objectives: matching the overall water balance, shape, peak flows and low flows (Kumar and Bhattacharjya, 2011; Madsen, 2000). Tradeoffs exist between objectives and no optimization is able to characterize all of them correctly (Madsen, 2000). Often, improved peak flow optimization means poor low flow optimization (Madsen, 2000). Thus, using a single optimization method is often inadequate (Madsen et al., 2002). However, auto-calibrations usually require use of a single objective function. In this case, the function used should be chosen based on the desired data output (Diskin and Simon, 1977; Yapo et al., 1998). When peak values are more important than low flow values or volumes, a peak-weighted function should be used. Additionally, the data set used in optimization should be similar to those intended for model use (Diskin and Simon, 1977).

## METHODS

### Study Site

The Lake Tahoe Basin is located in the Sierra Nevada Range and is situated along the border of California and Nevada (Smith and Blackwell, 1980) (Figure 6). The basin covers an area of 800 km<sup>2</sup> (312 mi<sup>2</sup>) and has sixty-three watersheds that flow into the lake (TERC, 2014). The lake is 495 km<sup>2</sup> (191 mi<sup>2</sup>), sits at an elevation of 1,897 m (6,225 ft) and empties out into the Truckee River (Forney et al., 2001; USGS, 2008). The lake is naturally occurring but was converted to a reservoir with the installation of a small dam at the lake's outlet. It was originally built in 1874 and most recently updated in 1913 (Forney et al., 2001; TRPA, 1997). Reaching a depth of 501 m (1,645 ft); it is the second deepest lake in the United States and the 11<sup>th</sup> deepest in the world (Forney et al., 2001; USGS, 2008). It is classified as an oligotrophic lake, which means it naturally has a deficiency of plant nutrients and productivity, high dissolved oxygen and clear water; a fact that has inspired historic acclaim (Forney et al., 2001). Water clarity is a function of suspended sediments and primary productivity; which is a function of nutrient loading (Forney et al., 2001). There has been a recorded decline in lake clarity at a rate of over one foot per year since readings started in the 1960's (Forney et al., 2001; USGS, 2008). Early recorded clarity depths reached annual averages of 30.5 m (100 ft) but by 1997 clarity had fallen to an annual average of 19.5 m (64.1 ft). In the past decade, clarity has improved somewhat averaging around 21.3 m (70 ft) (TERC, 2014).



Figure 6: Site location overview map. Study site basins are represented by bright green. The yellow square represents the extent of a closer site-specific view show in Figure 8.

Vegetation of the Basin is primarily coniferous forest and shrubland (Forney et al., 2001). Alders, aspen and willows are common along streams (Forney et al., 2001). Precipitation occurs mostly as snow in the winter months and varies across the basin with an average of 80 in/yr (203 cm/yr) on the western side and only 30 in/yr (76 cm/yr) on the eastern side of the Basin (TRPA, 1997). Historically most precipitation falls between November and March (TERC, 2014). The average percentage of precipitation that falls as snow dropped from 51% to 35% between 1910 and 2013 (TERC, 2014). Temperatures in South Lake Tahoe average 15.9 °C (60.6 °F) in July and -1.8 °C (28.8 °F) in January (Figure 7).

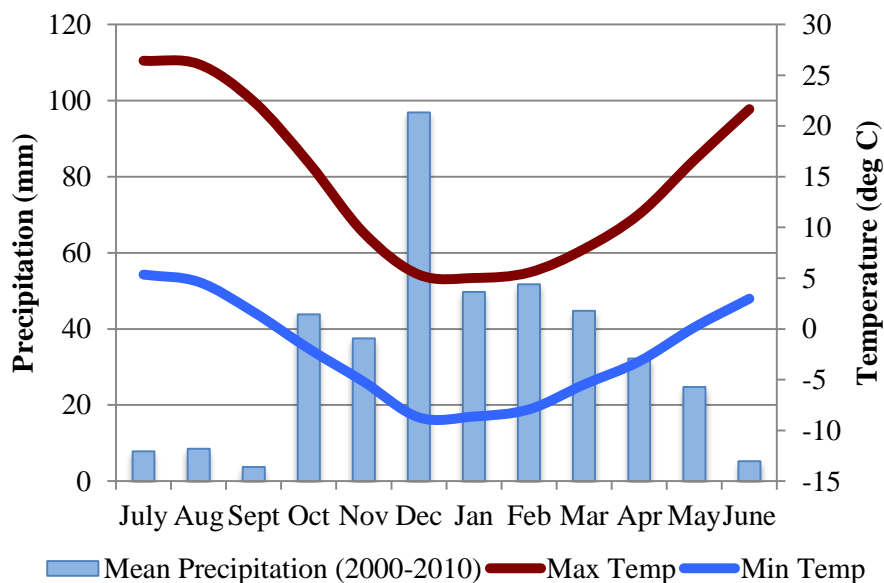


Figure 7: Average monthly temperatures and precipitation for South Lake Tahoe Airport station from 1968 to 2010 (NCDC, 2010).

Permanent population in the Tahoe basin increased from 10,000 to 55,000 between 1960 and 2010 (TERC, 2014; TRPA, 1997). In South Lake Tahoe (one of the larger cities located along the lake), population increased by nearly 77 percent from 1970

to 1998 (Forney et al., 2001). In addition, three million people visit Lake Tahoe annually to take advantage of recreational opportunities (TERC, 2014).

Due to the location and climate of Lake Tahoe Basin, particular watershed issues include urbanization of wetlands which formerly served as areas of retention for sediment and nutrient runoff, erosion from urban development on steep slopes, septic tank and sewer line discharge, airborne discharge from vehicles and wood-burning stoves, and the runoff of accumulated of sediments and chemicals on roads and other impervious surfaces (Forney et al., 2001; TRPA, 1997).

Three urban stormdrain outlets and their associated basins located in South Lake Tahoe were selected for this study (Figure 8). These sites were selected for suitability based on an estimated amount of impervious surface cover and suitable amounts of available precipitation and flow data.

Outlet gage data was obtained from a previous stormwater monitoring study performed in 2003 and 2004 by the Tahoe Research Group (TRG) at University of California at Davis and Desert Research Institute (DRI) for the Lahontan Regional Water Quality Control Board. The stormwater monitoring study contained nineteen sites located around the Lake Tahoe Basin including the three sites identified for this study. Outlets were identified by onsite visual detection and GPS coordinates given with the data. A second XY data point was collected using a Trimble GPS to verify the site location.

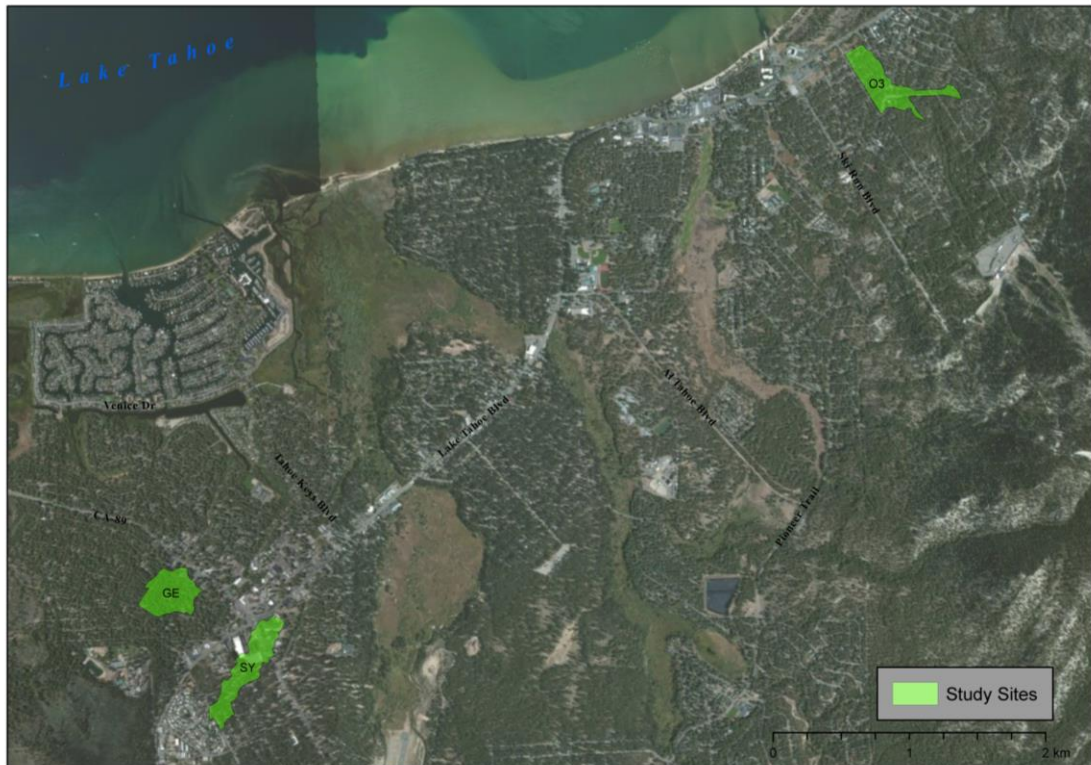


Figure 8: Study basins located in South Lake Tahoe include South Lake Tahoe Y (SY), Glorene and Eighth (GE) and Osgood Ave (O3). Basemap source: Esri, DigitalGlobe, GeoEye, i-cubed, USDA, AEX, Getmapping, Aerogrid, IGN, IGP, swisstopo, and GIS user community.

For each selected site, the contributing area was identified based on the drainage area identified by geospatial analysis of the DEM and a map of city storm drainage system obtained from the City of South Lake Tahoe public works engineering division. The city drainage map was used for estimation purposes only as it displayed only an approximation of drainage locations.

Once sites were selected, image and data processing began. Figure 9 shows an outline of the processing steps used on the data for the classification, terrain analysis and model setup. Further details on each process are described below.

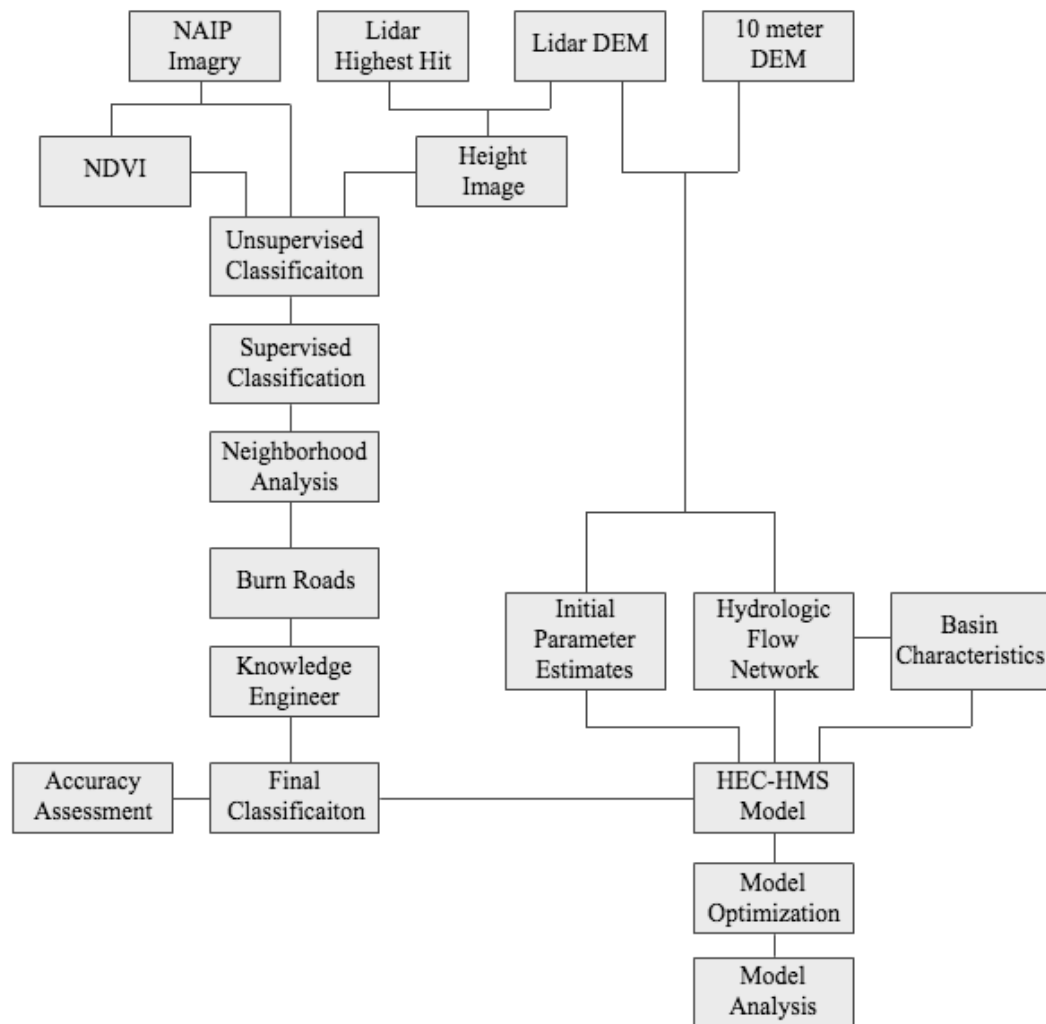


Figure 9: Outline of processing steps used for classification and model analysis.

## Classification

### Image Processing

The first step in image processing was to ensure that all data images and other data sets were aligned, in the same coordinate system and that similar data was contained in a single data set. Table 2 lists all the datasets used, their source and the analysis they

were used in. In all datasets, a single all-encompassing area of interest (AOI) was used to maintain continuity and relative geographic correspondence between sites.

An AOI including all study sites covered an area of nine LiDAR tiles that were mosaicked together using the Mosaic Pro toolset in ERDAS. The mosaic was run using bilinear interpolation and weighted seamlines. This same area was covered by four color-infrared aerial images from the National Agriculture Imagery Program. Three of the images needed to be georeferenced before they were mosaicked. Georeferencing was done in ERDAS and details on control points, RMS errors and methods can be found in Table 3. The images were referenced into the UTM NAD 83 Zone 10 North. All images were then mosaicked using cubic convolution and a weighted seamline. Light reflection off of Lake Tahoe was greatly varied in hue and intensity so this area was excluded from the mosaic calculations to prevent color distortion.

#### *Color Infrared Imagery*

National Agriculture Imagery Program (NAIP) color infrared four-band images from 2010 were obtained for the study site from two separate locations. Images were obtained for both California and Nevada to ensure full continuous coverage throughout the area of interest. The NAIP images had a one-meter resolution and were in an 8-bit format.

Table 2: Description, source and analytical use of data sets used in the study.

<b>Dataset Description</b>	<b>Source</b>	<b>Analysis</b>	<b>Original Projection</b>
LiDAR DEM	SNPLMA	DEM creation for modeling and impervious surface identification	UTM NAD 83 zone 10
NED 10-meter DEM	Nat'l Map Seamless Server	Generate model for comparison	Not Projected, NAD83 Datum
California NAIP Color Infrared Images	CA Atlas	Visual identification, NDVI, Classification	
Nevada NAIP Color Infrared Images	keck.library.unr.edu	Visual identification, NDVI, Classification	NAD 83 UTM Zone 11N
Field GPS locations	In the field	Outlet identification, Accuracy assessment	
Census		Property lines	
NLCD Land Cover (2001)	epa.gov/mrlc	Compare with generated impervious layer	USA Contiguous Albers Equal Area Conic USGS
Outlet Gage Data	Dr. Alan Heyvaert, Desert Research Institute	Model optimization and comparison	
Soils	Soil Data Mart - NRCS, USDA	Infiltration estimates in the model	Not Projected, NAD83 Datum
Precipitation	Dr. Alan Heyvaert, Desert Research Institute	Model optimization and runs	
Lake Tahoe Roads	Tahoe Data Clearinghouse	Classification of roads, georeferencing of NAIP	NAD 27 UTM Zone 10N

Table 3: Georeferencing details, control points, RMS error and methods used for the NAIP imagery.

Image ID	Referenced to	Control points	Check points	Low/High RMS error for control	Low/High RMS error for check	Method used
119H8NW	Georeferenced Image NV901	5	6	0.708/0.997	0.586/1.332	Cubic Convolution
119H8NE	Georeferenced Image NV901	6	6	0.505/1.232	0.195/1.870	Cubic Convolution
119H8SW	Tahoe Streets	6	4	0.089/0.262	0.373/0.923	Cubic Convolution

California images were acquired from the CA Atlas website and were in a Universal Transverse Mercator (UTM) North American Datum (NAD) 83 Zone 10 North projection (NAIP, 2011). Nevada images were acquired from the W.M. Keck Information center maintained by the University of Nevada at Reno and needed to be georeferenced.

The NAIP imagery was also used to create a normalized difference vegetation index (NDVI) by using the near infrared and red bands ([ 2 ]). The image was then converted to an unsigned 8-bit image to insure all layers would be weighted equally in classification attempts ([ 3 ]).

$$\frac{\text{Near Infrared} - \text{Red}}{\text{Near Infrared} + \text{Red}} \quad [ 2 ]$$

$$\frac{(\text{Input} - \text{Global Min} [\text{Input}])}{\text{Global Max} [\text{Input}] - \text{Global Min} [\text{Input}]} \times 255 \quad [ 3 ]$$

### *LiDAR*

High-resolution LiDAR data was obtained through the Round 10 Lake Tahoe Southern Nevada Public Land Management (SNPLMA) capital program. Watershed Sciences, Inc. (WSI) flew the LiDAR in the summer of 2010 and the resulting point cloud data was made available for this study. Ground resolution for the LiDAR was 11.82 points/m<sup>2</sup> and vertical accuracy was 3.5 cm. Further details on the methods and accuracy of the LiDAR data can be found in the data collection report produced by Watershed Sciences, Inc. (2011).

In addition to the raw LiDAR data, Watershed Sciences Inc. preprocessed and supplied hydro-enforced digital elevation models and highest-hit canopy models for the basin. Both of these datasets were used for analysis. They were received in tiles of approximately 5.6 km by 7.1 km with a resolution of 0.5 m.

Elevation values on the mosaicked DEM and highest hit model were converted to height values using the raster calculator tool in ArcMap to subtract the surface elevation from the highest hit elevation. **Error! Reference source not found.** [ 3 ] was run to convert the height information into an unsigned 8-bit dataset to maintain continuity with other datasets used in the classification. The height image was then resampled from 0.5 m to 1 m resolution to match the available resolution in the other datasets.

### **Land-Use Classification**

In preparation for the classification, the NAIP image (four layers), the NDVI image (one layer), and the height image (one layer) were compiled in ERDAS into a

single six-layer image. All layers were in an unsigned 8-bit format with a one-meter resolution. An unsupervised classification seeking twenty classes was run in ERDAS. The number of classes was chosen to cover the full spectrum of possible classes. The output cluster image and signature set created a starting point for the supervised classification.

The supervised classification was run for a more detailed and accurate separation of classes. The supervised classification used a total of 250 training polygons spread over 41 identified classes (Table 4). Many of these classes represented similar types of land cover that did not need to be distinguished from each other in the final classification but were initially classified separately due to distinct differences in their spectral signature. For example, buildings with different colored roofs were separated in the initial stages but later included in a single class. Since these distinctions are not relevant to the end classification, the number of classes was eventually condensed to nine (Table 4).

#### *Knowledge Engineer*

In post processing the number of classes was reduced using a recode operation that condensed multiple similar classes into a single class. Table 4 shows which classes were condensed and the final class value used. Once the recode was complete, clump and eliminate operations were run. The clump operation grouped pixels using all eight connected neighbors. The eliminate operation pulled out clumps smaller than 10 pixels (representing 10 m<sup>2</sup>) and replaced them with nearby values using a majority filter.

Table 4: Initial classes, number of training polygons and the number of pixels used for the supervised classification of the South Lake Tahoe.

<b>Class</b>	<b>Training polygons</b>	<b>Number of pixels</b>	<b>Final Class Value Used</b>
Snow	4	4059	1
Water (1, 2, 3)	14	353851	2
River (1, 2, 3)	16	20946	2
Algae Water	6	37649	2
Discolored Water	1	17885	2
Pools (1, 2)	6	1981	2
Dirt (1, 2)	12	170944	4
Sand (1, 2, 3, 4)	25	102654	4
Poor Grass	10	426294	6
Bright Grass (1, 2)	18	573239	6
Bushes	18	155643	7
Trees (1, 2, 3)	28	18931	8
Light-colored Roads	10	10186	9
Roads (1, 2, 3, 4)	22	292942	9
Buildings (1, 2, 3, 4, 5, 6)	30	252457	10
Shadow (1, 2, 3, 4, 5, 6)	30	9648	11

In the supervised classification there were some significant problems with the identification of certain classes. The most significant of these was confusion between the building, road and bare dirt classes and between the water and shadow classes. The Knowledge Engineer tool in ERDAS was used to increase identification accuracy. For

most classes (snow, sand, brush, pool, tree, and grass) the class was simply maintained with no additional classification rules. However the road, dirt, building, water and shadow classes were given additional rules based on slope, height and distance from a road. The thresholds for the rules were chosen through observation of slope and height in known areas in each class. These rules and a full diagram of the knowledge engineer can be found in Appendix A.

The LiDAR image was detailed enough to distinguish cars (Figure 4). Objects identifiable as cars were very often classified as buildings in the supervised classification when they should have been included in the road class. Most cars stood at a height of less than two meters off the ground surface which varied in the height image between eight and nine meters. Cars were moved to the road class by using combining both urban classes and then using a ten meter threshold to distinguish them.

To improve distinction between urban areas and the rock outcrops or dirt common in the high Sierras, the road network was used. Human development generally happens near access roads and thus nearness to the road network can be considered an indication of urban development. Luckily, South Lake Tahoe has a fairly detailed road network shapefile available. Urban areas were redefined with a threshold of 250 m from a known road. This was chosen based on observation of known urban areas. Although rock would be considered impervious surface, in general, the rock outcrops were disconnected from the streams and occurred in relatively small areas within the study sites. Therefore they were not distinguished from the dirt class.

Water and shadow classes were intermixed in the supervised classification. Some separation between the classes was provided using thresholds in the Knowledge Engineer. Rivers and water bodies generally have low slope and are even with the ground surface. Water was distinguished from shadow by using a slope threshold of 0.3 percent rise and a height threshold of nine meters (which put it at ground level).

While separating water from shadow is helpful, separating out the water class was only one of the necessary steps to reduce the shadow class. Much of the shadowed area fell across roads. The road network shapefile for South Lake Tahoe was used to further improve the road class and reduce the influence of shadows. The road layer is older than either the NAIP or LiDAR images. To insure accuracy, a close inspection of the road layer compared to the NAIP imagery and a DEM and slope image derived from the LiDAR data was conducted. Special care was taken within the study sites. Roads that were slightly misaligned with the image were edited in ArcMap to better match the NAIP and LiDAR data. Best judgment was used to decide where the centerline of the road should fall. A few roads were not included in the shape file while others were labeled as dirt when they were paved. Where errors were found, the layer was edited to include the road or change the label to represent current conditions as of 2010. Most of these errors occurred outside of the study site and do not affect the model results.

Once verified, the roads were given a buffer width based on their identified type. Each road type was measured from the NAIP imagery in multiple places using the ruler tool in ArcMap. The average road width value was used as the buffer width for that type of road (Table 5).

Table 5: Road classes, estimated widths and buffer values used in the supervised classification.

<b>Road Type</b>	<b>Buffer Value</b>	<b>Road Width (m)</b>
Major highway	8	16
2-lane highway	4	8
4-lane, divided city street	8	16
Major city street	5	10
Minor city street	4	8

In order to burn the road layer into the classified image, the layer was converted to a raster image. Roads were given a value of 100 and all other areas were given a value of zero. Each pixel in this image was then added to the corresponding pixel in the classified image with the raster calculator. This resulted in a classified image with several classes with values between zero and eleven and a second set of classes above 100. Any pixel with a value above 100 was recoded into the road class. This process dealt with a good portion of the shadowed area.

Remaining shadows were reduced using a neighborhood analysis. The analysis used a majority filter with a three by three window and was run on the shadow class only. This was designed to systematically reduce the area classified as shadow by converting it to nearby class values. As the filter has most effect on small areas or edges of larger area, it was necessary to run it seven times in order to remove most of the remaining large shadows.

In the final classification buildings and roads are the two main classes that were considered impervious. In addition, the small number of shadowed areas that remained fell mostly over impervious areas and therefore it was included in the impervious category. However, the study sites had only a very small amount of either the remaining shadow or water classes. All other classes were considered to be pervious areas.

### **Accuracy Assessment**

An accuracy assessment was conducted on the finished classified image. Although the assessment was originally focused only on the selected study sites, at the time, several sites were included that have since been removed from the study. A total of 170 points were randomly generated with approximately 15 points located in each basin. Points were located at least 30 meters apart from each other. They were given a buffer of 15 m to create 30 m<sup>2</sup> circles for analysis. Within the circle, the dominant land use was identified and recorded by observing NAIP images of the area and using slope and height images to help clarify difficult areas. The dominant classification for the area was also noted. The two values were compared to obtain accuracy values for the classified image.

### **Terrain Processing**

The HEC-HMS model should be run using an equal area projection so that area values remain true (HEC, 2010). The DEMs were reprojected from UTM NAD 83 Zone 10 into an Albers Equal Area Conic projection (Table 6).

Table 6: Albers Equal Area Conic projection values used in the HEC-HMS model.

<b>Projection Attribute</b>	<b>Value</b>	<b>Projection Attribute</b>	<b>Value</b>
Central meridian	-120	Unit	<i>Meter</i>
Standard parallel 1	30	Geographic coordinate system	<i>North America 1983</i>
Standard parallel 2	40	Datum	<i>North America 1983</i>
Latitude of origin	28	Spheroid	<i>GRS 1980</i>

The basins, subbasins and streams were generated using the GeoHEC-HMS toolset in ArcMap. The process outline can be found in Figure 10 and is described in great detail in the HEC-HMS User's Manual (HEC, 2010). First, sinks, or small dips in the DEM were filled in order to calculate water flowing continuously in a stream network. With the filled DEM, the flow direction was calculated and each pixel was given a value based on which of eight possible directions water would flow off of it.

Flow accumulation was calculated from the flow direction layer based on how many pixels flowed into each pixel. When enough flow accumulated, it was defined as a drainage. In this model, we are interested in overland runoff paths in much smaller urban basins. These basins do not have any natural streams. Instead they contain manmade drainages and consequently drainages were much denser than found in a natural network.

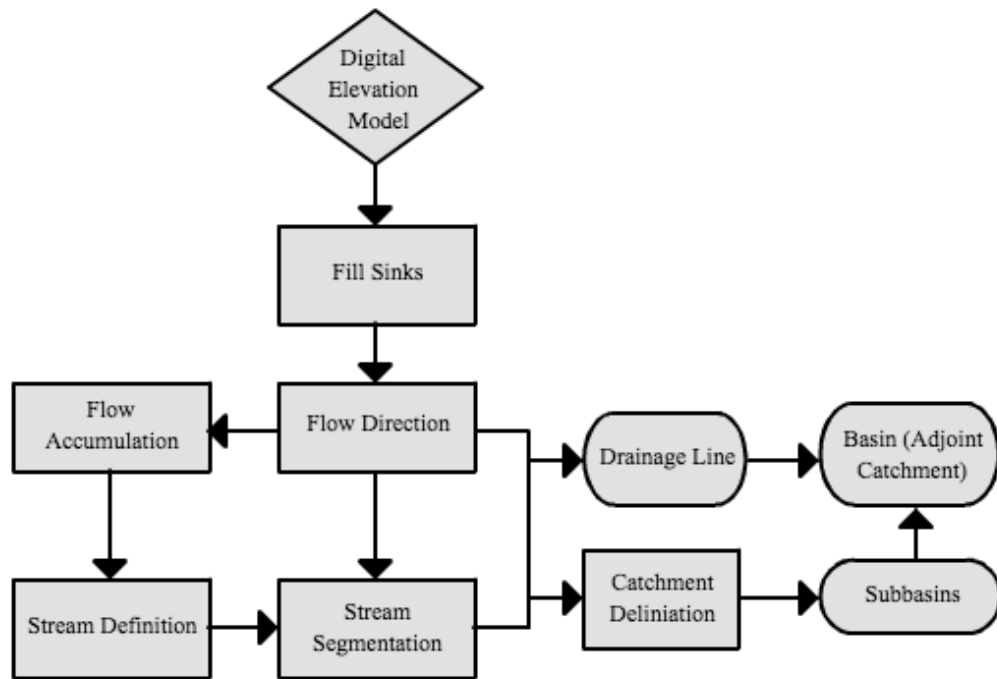


Figure 10: Terrain processing flow chart depicting methods used to create drainage lines, basins and other necessary layers for the HEC-HMS model.

Once defined, drainages were split into reaches using the stream segmentation tool and based on flow direction and confluences. The segmented stream raster was converted to a line shapefile used in the model as the drainage line. It is also utilized to identify catchment areas for the model. Similar techniques were used for both the LiDAR and 10-meter DEM.

### HEC-HMS Model

For each study area two models were created using the USGS 10-meter and LiDAR 1-meter DEMs. The corresponding DEM and the classified image were used to identify basin area, flow patterns and model parameters estimates for each model. Models were created in the GeoHEC-HMS toolset for ArcMap 10.1 and later open and run in

HEC-HMS 3.5. Terrain analysis, detailed above, acted as a starting point for each project created in HEC-HMS. The model used a single pour point located at the stormdrain outlet where observed data was collected. For analysis purposes, it was necessary to place the pourpoint over a flow line for that basin. This did not always fall on the GPS marked location of the stormdrain outlet. The pourpoint was therefore located over the flow line at the point nearest to the GPS location. Table 7 notes the distance in meters between the GPS location of the outlet and the pourpoint used to create the basin models. These distances vary both by site and by DEM used.

Table 7: Distance in meters between pourpoints used for basin delineation and the GPS location identified during on-site drainage outlet identification.

<b>Site</b>	<b>10-m Model Distance (m)</b>	<b>LiDAR Model Distance (m)</b>
SY	116.8	109.4
O3	8.4	32.4
GE	35.2	16.6

The HEC-HMS model delineates the basins using the terrain analysis and subdivides them based on confluences in the drainage network. In most cases it was necessary to merge or split subbasins and the drainage network in order to maintain simplicity and mimic the understood nature of that particular urban basin as much as possible. Human influences on the basins, in the form of alterations to the drainage pattern or diversion of water from one basin to another, were accounted for at this time. Influence on the basin was mostly determined by observing a map of the known

stormdrain system developed for the City of South Lake Tahoe Engineering Department by Kennedy/Jenks Consultants (2010) (Figure 11). Not all areas have been quality controlled and best judgment was applied when choosing where to split, stop or change the subbasin and drainage network.

Once the basins and drainage network were defined, basin, drainage line and DEM characteristics were calculated. Table 8 displays the attributes found and their method of calculation. All values were calculated in the projection units (meters) and were later converted into English units for use in the model. English units were used in the model because the observed flow and precipitation data obtained were in English units. Additionally, in some cases the size of the storm was small enough that basin output included periods with less than  $0.1 \text{ m}^3/\text{s}$ . Values below 0.1 were rounded up to 0.1 by the HEC-HMS program thus creating a distortion in the data that did not occur in those same storms when cubic feet per second was used.



Figure 11: LiDAR and 10-meter study site basins overlaid on urban storm water drainage map from the South Lake Tahoe Department of Transportation. Sites located in South Lake Tahoe, CA.

Table 8: Model attributes, calculation methods and their inputs

Attribute Value	Unit	Method	Inputs
<b>River Length</b>	Meters	Length	Drainage Line
<b>River Slope</b>		$\frac{\text{Up Elevation} - \text{Down Elevation}}{\text{Length}}$	Drainage Line, DEM
<b>Slope</b>		Percent rise	DEM
<b>Basin Area</b>	Meters	Area	Subbasins
<b>Basin Slope</b>		Basin average slope	Slope
<b>Longest Flow Path</b>	Meters	Longest length of flow from basin divide to basin outlet	Flow direction, DEM, Subbasins
<b>Centroid</b>	Latitude, Longitude	Center of Gravity	Subbasins
<b>Centroid Elevation</b>	Meters	Elevation of point	Centroid, DEM
<b>Centroidal Longest Flow Path</b>	Meters	Longest length of flow from a point parallel to the basin centroid to the basin outlet	Centroid, Longest Flow Path, Subbasins

### Model Setup

The HEC-HMS program uses a basin model to depict drainage shapes and size and a meteorologic model to implement precipitation values (HEC, 2000; Kumar and Bhattacharjya, 2011). The basin model was created using methods described above and exported into the HEC-HMS format. The meteorological model used was a user defined specified hyetograph. Since the study sites covered a small area, a large variation in rain pattern and amount within the basins was unlikely and only the nearest rain gauge precipitation values were used. Sites SY and GE used the same gage station, City Lab,

and site O3 used the Sierra House gage station. Table 9 shows the distance in meters from the basin centroid to the associated gage station for each site and model.

Table 9: Distance in meters between model basin centroids and the associated precipitation gage.

<b>Site</b>	<b>Precipitation Gage</b>	<b>10-m Model Distance (m)</b>	<b>LiDAR Model Distance (m)</b>
SY	City Lab	610.0	703.5
O3	Sierra House	4657.0	4618.9
GE	City Lab	744.0	846.3

### **Model Methods and Parameter Calculations**

The HEC-HMS model uses four separate methods to predict water movement from rainfall to the outlet (HEC, 2000). The loss rate method is defined as the amount of precipitation lost to infiltration, interception and depression storage and predicts excess runoff (ASCE, 1996). The transform method represents how excess runoff reaches the drainage (HEC, 2000). Baseflow method describes drainage baseflow values and the routing method deals with in-stream transport of water to the outlet (HEC, 2000). Table 10 lists the methods used in the models for this study and their associated parameters. All processes remained the same over the various models for consistency. Initial estimates of model parameters were calculated in excel from attributes exported from the GIS data. Initial parameter estimates for each model can be found in Appendix B.

Table 10: Methods and parameters used for HEC-HMS models.

<b>Process</b>	<b>Method</b>	<b>Parameters</b>
Loss Method	Initial and Constant	Initial loss, Constant loss rate, Percent impervious area
Transform Method	Snyder Unit Hydrograph	Snyder lag time, peaking coefficient
Baseflow method	Constant Monthly	Baseflow value per month
Routing Method	Lag	Lag

### *Loss Method*

The initial and constant rate method was chosen for its simplicity in set up, ability of use with a lack of detailed soil information and its extensive use in previous studies (ASCE, 1996; HEC, 2000). Some such studies include Cunderlik and Simonovic (2007), Pistocchi and Mazzoli (2002) and Yusop et al. (2007). It expresses loss as an initial value representing interception and depression storage followed by a constant potential rate of loss due to infiltration (ASCE, 1996; HEC, 2000).

The initial loss is the amount of precipitation that can fall before runoff begins. It is controlled by land use, soil type, soil condition and terrain (HEC, 2000). This parameter is best found through optimization but a previously set standard suggests that 10 to 20 percent of precipitation should be used in forested areas and 0.1 to 0.2 inches should be used for urban areas (Saleh et al., 2011). Suburban areas in the study sites are have some forested landscape, however it is still in an urban setting. Therefore a value of 0.2 was used as a starting point for all subbasins in the study. This value was then optimized to improve and individualize it at each study site.

The constant rate is influenced by physical soil properties and land use (HEC, 2000). The Soil Conservation Service (1986) classification of soil based on infiltration capacity and Skaggs and Khaleel (1982) estimates of infiltration rates for those soils were used for initial estimates (Table 1) (HEC, 2000). When a subbasin contained multiple soil types, the basin average infiltration rate was calculated using the percent area of each soil type. In addition, during the subbasin delineation process the basins were split to try and group soil types. Calculations were made for both the low and high end of the known infiltration range to obtain a range for each subbasin. The average infiltration rate was used as an initial estimate. In some cases it did not appear to adequately represent the infiltration in preliminary runs and the higher infiltration rate was used instead.

No loss calculations are carried out on area designated as impervious. An estimate of percent impervious area was found using the impervious classes identified in the classification process. In ArcMap, a polygon layer was created from just the impervious classes (buildings and roads). The lines between adjacent polygons were then dissolved. The road network, and the ditches that run along side it, are the main connection between impervious area and the site outlets. Therefore, all areas of this impervious layer that did not connect to the road network were discarded. The remaining area was used to calculate percent impervious area for each subbasin.

### *Transform Method*

Snyder's Unit Hydrograph is a good model for short period floodcasting (Halwatura and Najim, 2013). It uses lag, peak flow, and total time to calculate runoff reaching the drainage. Snyder lag time was estimated by the equation:

$$t_p = C_t(L \times L_c)^{0.3} \quad [ 4 ]$$

where  $t_p$  is the lag time,  $C_t$  is the basin coefficient,  $L$  is the length of the stream from the outlet to the divide and  $L_c$  is the length along the stream from the point nearest the centroid to the outlet. The basin coefficient is best found through calibration but is typically between 1.8 and 2.2 (HEC, 2000). It has been found as low as 0.4 in mountainous areas (HEC, 2000). In this model it was originally set at 0.2 because equation output values seemed reasonable compared to the lag seen in observed hydrographs using this coefficient value. The small size of the basins and high density of drainages could have something to do with why the basin coefficient values were so far below typical. Lag time is considered a constant and therefore is not influence by the intensity of the storm (Halwatura and Najim, 2013). Peaking coefficient ranges from 0.4 to 0.8 with larger values associated with smaller values of  $C_t$  (HEC, 2000). Despite that, the initial value for the peaking coefficient was set at 0.1 because early optimization attempts suggested the parameter was likely to end up near there.

### *Baseflow Method*

The constant monthly baseflow method is the simplest model. It uses a constant value for baseflow that can vary monthly (HEC, 2000). It does not account for any

change in baseflow during an event. In most urban channels and smaller streams in the west and southwest U.S. baseflow is negligible (HEC, 2000). Field observations indicate that the study drainage network did not have any flow outside of storm runoff.

Additionally, flow measurements drop to zero or near zero between storms at all sites.

Therefore the baseflow constant was considered null and set to zero for all months.

### *Routing Method*

The lag routing model is the simplest routing model to use. Outflow is identical to the inflow hydrograph but delayed by a specified duration. The hydrograph does not change shape. This method is widely used in urban drainage channels (HEC, 2000). Observing lag between peak or area centroid of inflow and outflow hydrographs can identify initial estimates. There was no suggested method of identifying routing lag time other than model optimization (HEC, 2000). However after some early optimization runs, initial estimates of 3.5, 5 and 7.5 minutes was found to be an adequate starting point for lag time.

### **Storm Selection**

Observed storm data was obtained from the Tahoe Research Group (TRG) and the Desert Research Institute (DRI) and included precipitation and flow values. Storms were grouped for a modeling run based on similarity of output volume, maximum peak flow and storm type. Site O3 and GE each used one group of storms for optimization and model runs. Storms at site SY were grouped into two groups due to the extensive availability of storms. Storms were not included if they lacked precipitation data or other

precipitation/flow errors were noticeable. Limitation of available storms at site GE forced the inclusion of some less than optimal storm data. This means the inclusion of some storms where snow was either precipitated during the storm or was on the ground prior to the storm.

### **Optimization**

Each model required an optimization trial to fine-tune the estimated parameters. Observed storm data from one storm in each modeling group was used for optimization. The storm selected for optimization fell in the middle of the storm group with data that had no major gaps and flow mirrored the precipitation well.

HEC-HMS offers two search methods and seven objective functions for model optimization (HEC, 2000). In order to select the best possible method several trial runs were conducted using the May 27<sup>th</sup> optimization storm from site SY set A. For these trials the number of parameters and other selections were kept constant and only the method of optimization changed. The final optimization method selected was the Nelder-Mead simplex method using the peak-weighted root mean square error objective function.

Optimizable parameters included lag time for each reach and constant loss rate, initial loss rate, Snyder peaking coefficient and Snyder time to peak for each subbasin. All parameters involved were included in the optimization of the model output due to the roughness of the initial estimates of variables. Maximums and minimums for the parameters were left at their default values (Table 11).

Table 11: Maximum and minimum parameter values in HEC-HMS optimization.

<b>Parameter</b>	<b>Min</b>	<b>Max</b>
Reach Lag	0.001	30,000
Initial Loss	0.001	19.69
Constant Loss rate	0.001	11.811
Snyder time to Peak	0.1	500
Snyder peaking coefficient	0.1	1

Once optimized, models were run with precipitation values for the other storm events. Precipitation input values were the same for corresponding LiDAR and 10-meter models. Flow outputs were exported to excel for visual and statistical comparison.

### Model Evaluation

LiDAR data outputs were compared to 10-meter DEM layer models as well as observed monitoring data for the key aspects of the hydrograph. Overall shape was compared visually as well as with Nash-Sutcliffe efficiency values. The Nash-Sutcliffe efficiency ( $E$ ) can be found using the equation:

$$E = 1 - \frac{\sum_{i=1}^n (O_i - P_i)^2}{\sum_{i=1}^n (O_i - \bar{O})^2} \quad [ 5 ]$$

where  $O_i$  is the observed data,  $P_i$  is the modeled data,  $\bar{O}$  is the mean of the observed data. The range of  $E$  falls between one, which indicates a perfect fit, and  $-\infty$ . When the value falls to zero it indicates that the mean of the observed flow would have been a better predictor than the model (Krause et al., 2005). The disadvantage of using  $E$  is that

the differences between observed and predicted values are squared resulting in overestimation in larger values while underestimating low flow values. Therefore it is not very sensitive to systematic model over/under prediction (Krause et al., 2005).

Using logarithmic values helps prevent the over- and underestimation of peaks and low flows by flattening peaks while keeping low flows more or less the same (Krause et al., 2005). The logarithmic efficiency ( $E_{ln}$ ) can be found with the equation:

$$E_{ln} = 1 - \frac{\sum_{i=1}^n (\ln O_i - \ln P_i)^2}{\sum_{i=1}^n (\ln O_i - \bar{O}_{lnO})^2} \quad [6]$$

where  $\ln O_i$  is the natural log of the observed value and  $\bar{O}_{lnO}$  is the mean of  $\ln O_i$  for all events considered.  $E_{ln}$  also falls between one and  $-\infty$  with one representing a perfect fit. In comparing  $E$  with  $E_{ln}$ , Krause et al. (2005) found that  $E$  primarily focused on peaks and high flow at the expense of low flow and  $E_{ln}$  reacted less to peak flows but was better at quantifying error in low flows. Krause et al. (2005) recommend that a combination of different efficiency criteria should be applied along with an absolute or relative volume error assessment. Therefore both  $E$  and  $E_{ln}$  were used to analyze models.

In addition to Nash-Sutcliffe efficiency and visual observation, overall volume and peak rate values were obtained from the dataset and compared relative to the observed dataset using percent error. Peak timing was shown to have some significant errors within a number of the storm datasets. In addition the optimization did not focus on peak timing. Therefore no analysis was done on the timing of peak events.

## RESULTS

### Land-Use Analysis

#### **Classification**

##### *Unsupervised*

The unsupervised classification resulted in seven classes that could be separately identified (Figure 12). Water and shadow were not distinguished from each other in this classification. In addition there was significant overlap in spectral signatures between bare dirt and roads and between urban features (noted as roads and buildings in figure). Trees and vegetation were the most straightforward resulting classes. This preliminary classification suggests that site SY has the least tree cover and the greatest percentage of urban development of the three sites. Site GE appears to have the most tree cover and the least urban development.

##### *Supervised*

Final supervised classification outputs of all three sites can be found in Figure 13. Supervised classification shows an improvement in the water, road, building, and dirt classes compared with the unsupervised classification. Area of each class found in the LiDAR and 10-meter basins is listed in Table 12. Percent area of urban classes (buildings and roads) is greatest at site SY and least at site GE. As basin size and shape differed between LiDAR and 10-meter models, percent area of urban classes within the basin also differed. These values can also be found in Table 12.

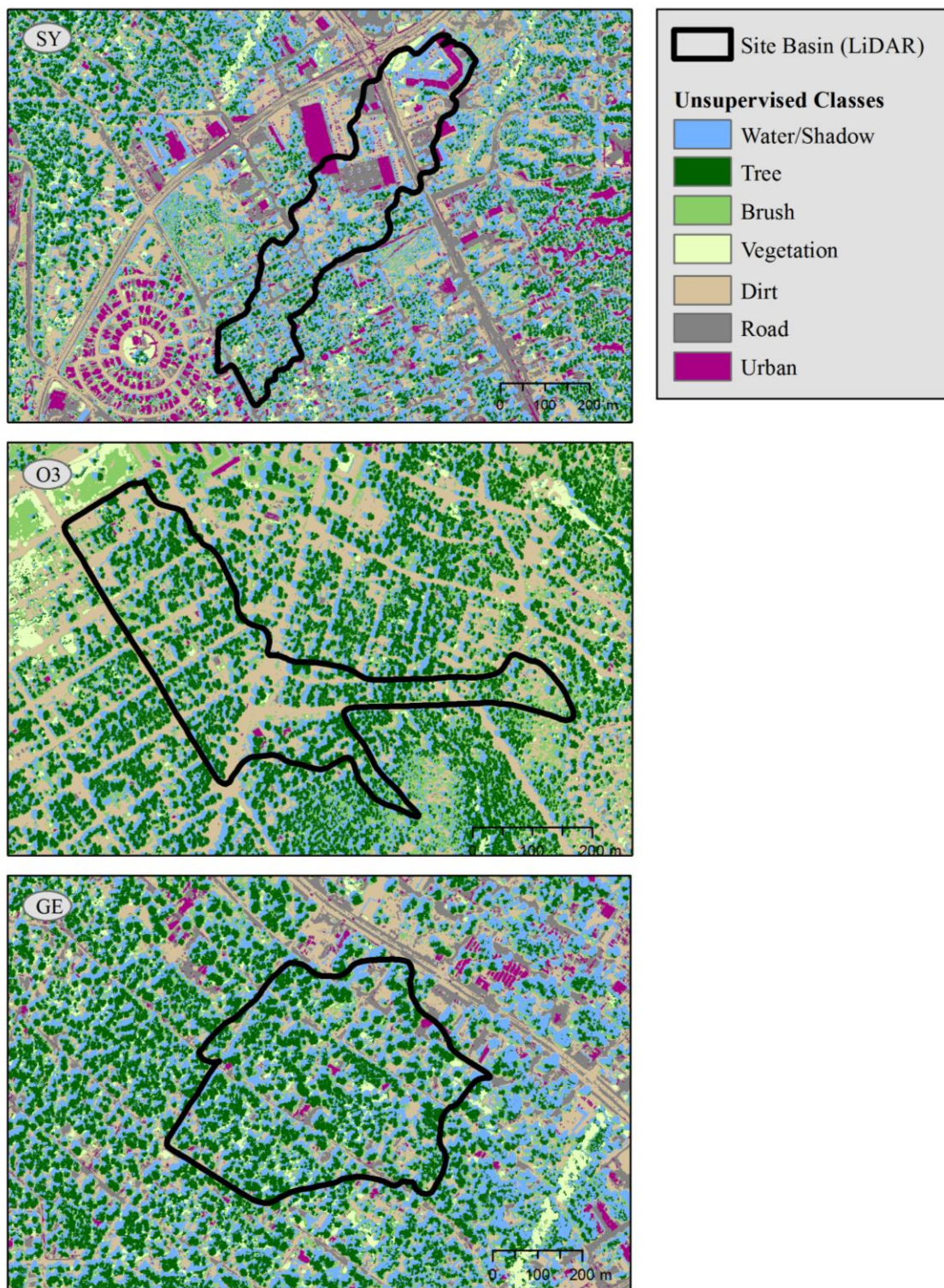


Figure 12: Unsupervised classification at study sites South Lake Tahoe Y (SY), Osgood Ave (O3) and Glorene and Eighth (GE) showing LiDAR derived basins, South Lake Tahoe, CA.

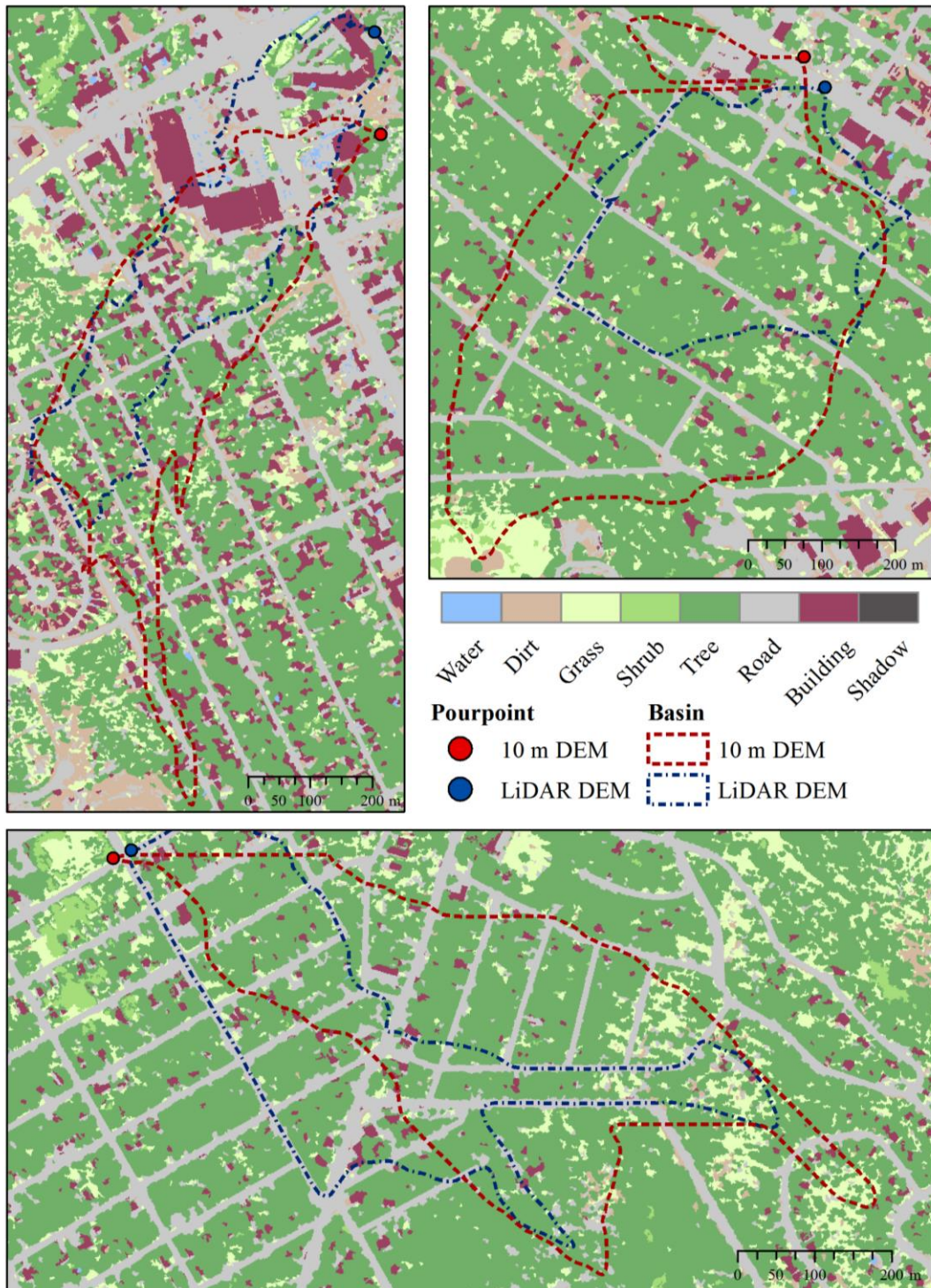


Figure 13: Final supervised classification for study sites South Lake Tahoe Y (SY), Osgood Ave (O3) and Glorene and Eighth (GE) showing derived basins and pourpoints used.

Table 12: Area and percentage of basin for each class in the supervised classification for study sites SY (a), O3 (b) and GE (c)

a) Site - South Lake Tahoe Y (SY)

<b>Class</b>	<b>LiDAR Area (m<sup>2</sup>)</b>	<b>LiDAR Area (%)</b>	<b>10-m Area (m<sup>2</sup>)</b>	<b>10-m Area (%)</b>
Water	1,403.4	0.99	1469.9	0.85
Dirt	8,770.6	6.20	10725.2	6.22
Grass	7,787.1	5.51	9489.0	5.50
Shrub	802.1	0.57	634.4	0.37
Tree	41,871.0	29.62	67964.0	39.42
Road	51,842.6	36.67	52106.2	30.22
Building	28,845.4	20.40	29948.4	17.37
Shadow	52.2	0.04	63.0	0.04

b) Site – Osgood Ave (O3)

<b>Class</b>	<b>LiDAR Area (m<sup>2</sup>)</b>	<b>LiDAR Area (%)</b>	<b>10-m Area (m<sup>2</sup>)</b>	<b>10-m Area (%)</b>
Water	36.2	0.03	31.2	0.02
Dirt	798.3	0.60	1812.5	0.92
Grass	7,827.7	5.84	13864.9	7.07
Shrub	41.0	0.03	203.0	0.10
Tree	83,995.6	62.70	132988.4	67.82
Road	35,753.2	26.69	42588.4	21.72
Building	5,504.0	4.11	4611.7	2.35
Shadow	0.0	0.00	0.0	0.00

Table 12: Area and percentage of basin for each class in the supervised classification for study sites SY (a), O3 (b) and GE (c) (continued).

c) Site – Glorene and Eighth (GE)

<b>Class</b>	<b>LiDAR Area (m<sup>2</sup>)</b>	<b>LiDAR Area (%)</b>	<b>10-m Area (m<sup>2</sup>)</b>	<b>10-m Area (%)</b>
Water	81.0	0.07	81.0	0.03
Dirt	3,212.9	2.83	7089.8	2.67
Grass	5,546.1	4.89	16673.9	6.28
Shrub	1,307.9	1.15	3288.1	1.24
Tree	82,433.4	72.72	187953.8	70.74
Road	16,158.7	14.25	39131.7	14.73
Building	4,619.6	4.08	11481.8	4.32
Shadow	0.0	0.00	0.0	0.00

### Accuracy Assessment

Table 13 shows details of the accuracy assessment for the final supervised classes compared to NAIP imagery. The classification proved least accurate when identifying dirt and grass and most accurate in the identification of water. While the overall classification accuracy was 75.9 percent, this study was most interested in the identification of impervious areas such as buildings and roads. The users accuracies for these two classes are both above 82 percent. User and producer accuracy values improve when classes are reduced to a binary impervious/pervious categorization (Table 14). Regrouped classes were again compared to the NAIP imagery this time evaluating only if the point fell on impervious or pervious area (as identified in the NAIP imagery) and

resulted in an overall accuracy of 93.5 percent. While most areas classified as impervious were indeed impervious (97.3 percent) only 78.3 percent of the actual impervious areas were correctly classified. Consequently, there is clearly an underestimation of impervious surface in the basins that could be as high as 21.7 percent.

Table 13: Accuracy assessment for all classes in the supervised classification. Overall classification accuracy is 75.88%.

<b>Class Name</b>	<b>Reference Points</b>	<b>Classified Points</b>	<b>Number Correct</b>	<b>Producers Accuracy</b>	<b>Users Accuracy</b>
Water	9	11	9	100.00%	81.82%
Dirt	26	34	23	88.46%	67.65%
Grass	47	31	27	57.45%	87.10%
Bushes	12	9	7	58.33%	77.78%
Tree	31	48	27	87.10%	56.25%
Road	29	25	24	82.76%	96.00%
Buildings	16	12	12	75.00%	100.00%
Shadow	0	0	0	---	---
<b>Total</b>	<b>170</b>	<b>170</b>	<b>129</b>		

Table 14: Accuracy assessment for pervious and impervious classes combined from supervised classification. Overall classification accuracy is 93.53%.

<b>Class Name</b>	<b>Reference Points</b>	<b>Classified Points</b>	<b>Number Correct</b>	<b>Producers Accuracy</b>	<b>Users Accuracy</b>
Pervious	124	133	123	99.19%	92.48%
Impervious	46	37	36	78.26%	97.30%
<b>Totals</b>	<b>170</b>	<b>170</b>	<b>159</b>		

## Flow Analysis

### Outlet Location

The latitude and longitude of the outlet locations identified by onsite observation revealed some potential error. Outlet points identified were between 6 and 56 meters from the location of corresponding outlets received from the Tahoe Research Group (TRG) (Table 15). Additionally, drainage area for the located sites differed by at least 7400 m<sup>2</sup> (Table 15). In the field, outlet points were located with GPS. Outlet points were also identified using a flow analysis on the DEMs. These two methods of outlet identification did not match exactly. Outlets found with flow analysis were used to place model outlet points directly on flow lines for use in the models.

Table 15: Differences in values determined with outlet coordinates reported by DRI/TGR and those recorded in the field.

<b>Site ID</b>	<b>Site Name</b>	<b>Received Area (m<sup>2</sup>)</b>	<b>Derived Area (m<sup>2</sup>)</b>	<b>Distance between outlet points (m)</b>
SY	SLT-Y	147,492	140,047	55.5
O3	Osgood Ave	96,786	116,583	6.8
GE	Glorene and Eighth	4,115	112,841	42.2

### Flow Patterns and Basin Characteristics

Flow patterns resulting from the 10-meter DEMs differed dramatically from the LiDAR derived DEMs (Figure 14). When contrasted with classified images, the LiDAR derived flow lines improved our understanding of where water flows over impervious surfaces (Figure 15). LiDAR resulted in more sinuosity in the flow lines than the 10-

meter drainages. Although drainage densities were similar when area drained at the start of the network is 500 m<sup>2</sup>, 10-meter networks had more variation between sites ranging from 0.043 to 0.075 (Table 16). LiDAR networks drainage ratios only ranged from 0.054 to 0.068. Figure 15 shows that while drainage densities were comparable, LiDAR drainages attained this through greater sinuosity as a result of flowing around objects or with the detailed differences in landscape. 10-meter networks at this scale often had several drainages that ran parallel to each other depicting the general flow surface without detail. With the drainages used for the model simulations, LiDAR networks had higher drainage densities and more sinuosity in all sites (These flow patterns also resulted in different sizes and shapes of the basin contributing to each outlet (Figure 13). The 10-meter derived basins were larger than LiDAR derived basins at the same site (Table 17). Site GE showed the largest discrepancy between basin sizes. Despite larger basin sizes, sites SY and O3 had lower percentages of DCIA in the 10-meter basins than in the LiDAR basins (7.7 % and 10.9 % respectively). Site GE had a slightly higher percent DCIA in the 10-meter basin

Table 17).

Table 16: Total drainage length per square meter for each site. Drainages begin with a collection area of 500 m<sup>2</sup>.

<b>Drainage Resolution</b>	<b>Watershed</b>	<b>Network Length (m)</b>	<b>Basin Area (m<sup>2</sup>)</b>	<b>Drainage Length per Area (m/m<sup>2</sup>)</b>
10-meter	SY	7423.2	172400	0.043
	GE	16,264.4	265700	0.061

	O3	14,799.5	196100	0.075
LiDAR	SY	7712.5	113359.5	0.068
	GE	8752.8	133956	0.065
	O3	7614.8	141374.5	0.054

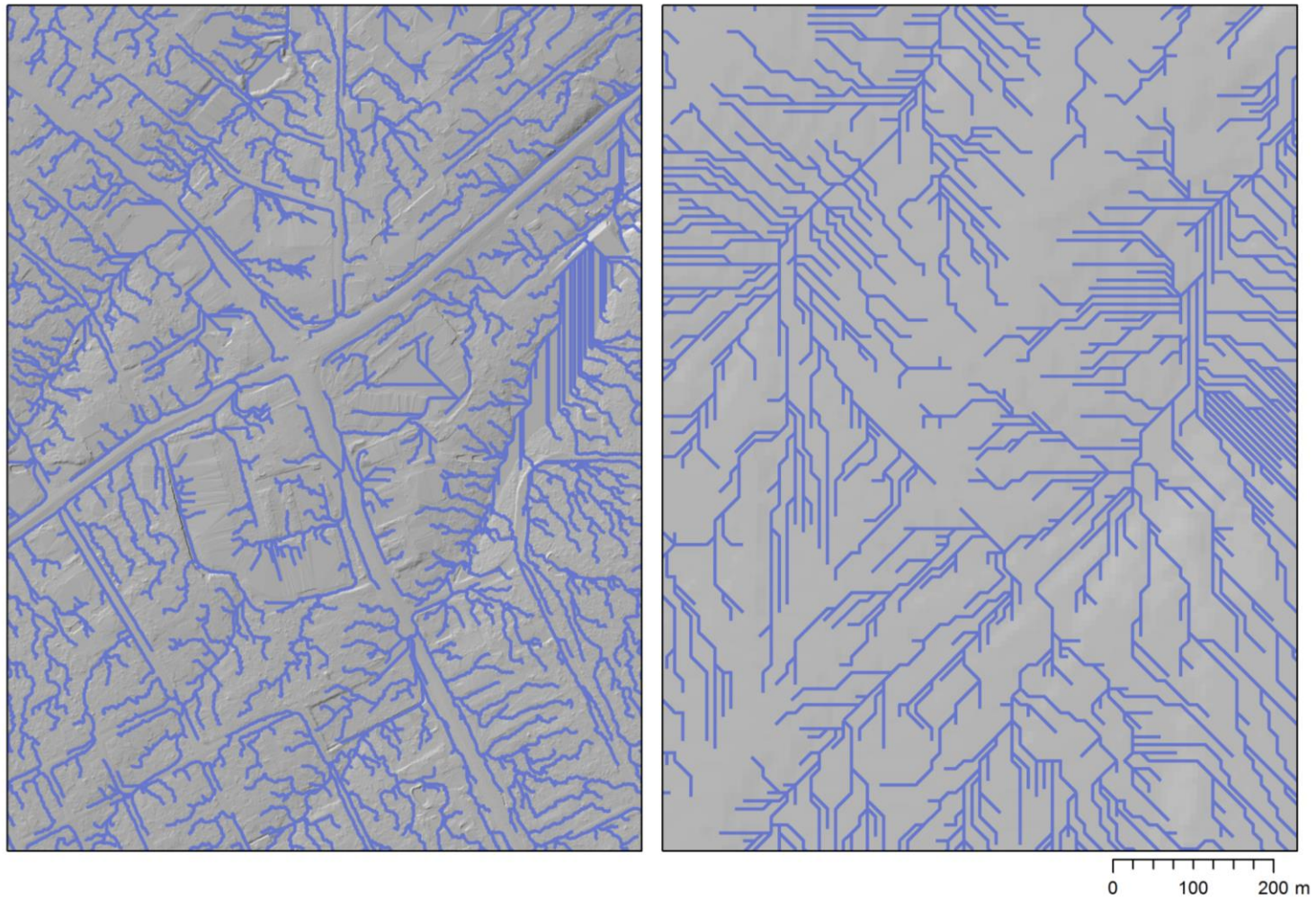


Figure 14: Flow lines derived from LiDAR (a) and 10-meter (b) DEMs. Flow begins when an area of 500 m<sup>2</sup> drains to that point.

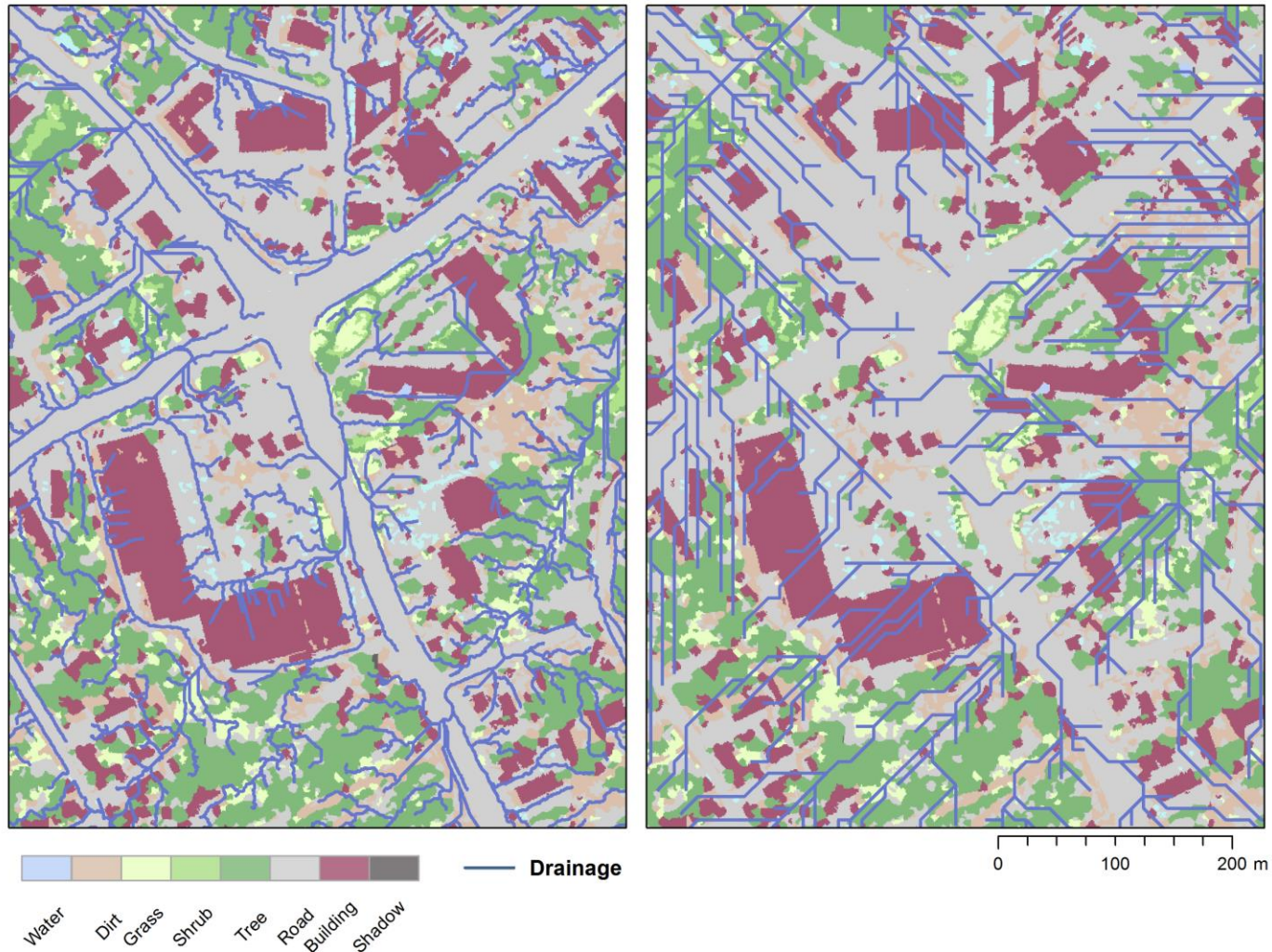


Figure 15: LiDAR (left) and 10-meter DEM (right) derived flow patterns over classified image near site SY. Flow lines represent an area of 500 m<sup>2</sup> or greater of runoff accumulation.

These flow patterns also resulted in different sizes and shapes of the basin contributing to each outlet (Figure 13). The 10-meter derived basins were larger than LiDAR derived basins at the same site (Table 17). Site GE showed the largest discrepancy between basin sizes. Despite larger basin sizes, sites SY and O3 had lower percentages of DCIA in the 10-meter basins than in the LiDAR basins (7.7 % and 10.9 % respectively). Site GE had a slightly higher percent DCIA in the 10-meter basin

Table 17: 10-meter (a) and LiDAR (b) basin attributes including area, drainage length and density, slope calculated as percent rise, and percent DCIA.

a.) 10-meter basins

Site	10-meter Basin Area (m <sup>2</sup> )	Drainage Length (m)	Drainage Density (m/m <sup>2</sup> )	Maximum Slope (%)	Average Slope (%)	DCIA (%)
SY	172,400	1,176.5	0.007	101.3	4.5	43.0
O3	196,100	813.4	0.004	131.0	9.7	19.6
GE	265,700	833.1	0.003	146.9	8.1	14.3

b.) LiDAR basins

Site	LiDAR Basin Area (m <sup>2</sup> )	Drainage Length (m)	Drainage Density (m/m <sup>2</sup> )	Maximum Slope (%)	Average Slope (%)	DCIA (%)
SY	141,380	1,230.0	0.009	114.2	4.5	53.9
O3	133,956	1,650.2	0.012	129.9	8.0	27.3
GE	113,360	1,085.7	0.010	102.9	7.8	13.4

LiDAR and 10-meter basins differed in average basin slope due to the size, shape and location of the basins and the values in the two different elevation models. These flow patterns also resulted in different sizes and shapes of the basin contributing to each

outlet (Figure 13). The 10-meter derived basins were larger than LiDAR derived basins at the same site (Table 17). Site GE showed the largest discrepancy between basin sizes. Despite larger basin sizes, sites SY and O3 had lower percentages of DCIA in the 10-meter basins than in the LiDAR basins (7.7 % and 10.9 % respectively). Site GE had a slightly higher percent DCIA in the 10-meter basin

Table 17 shows basin minimum, maximum and average slope calculated as percent rise. Basin O3 had the largest difference in average slope between LiDAR and the 10-meter DEM. The average slope values derived from LiDAR were close to those derived from the 10-meter DEMs at sites SY and GE

## Modeling

### **Model Optimization**

Model optimization improved the similarity between observed and modeled hydrographs. LiDAR site SY, used as a basis for selecting optimization methods, showed greater improvement in flow values with the Nelder-Mead simplex as an operating method than with the univariate gradient method. Most sub-methods showed only small variation in flow outputs. The sub-methods that showed the greatest improvements were peak-weighted root mean square error (PWRMS) and percent volume error (PVE). PWRMS showed the most improvement in peak values while PVE showed the most improvement in volumes.

Three of the four models were optimized on the same storm. Sites SY and GE are relatively close together and both use the City Lab storm gage. Site O3 is located closer to the **Sierra House** storm gage and made use of precipitation values from that gauge which varied slightly from those at City Lab. The fourth optimization was run on the December 5<sup>th</sup> storm for a second grouping of site SY storms. Output hydrographs for all storm events can be found in Appendix C.

#### *South Lake Tahoe Y (SY)*

A total of 0.39 in (9.91 mm) of rain fell during the storm beginning on the 27<sup>th</sup> of May that led to May that led to two observed peaks at 1:40 am and 5:40 am on May 28<sup>th</sup>. Optimization increased the peaks of both models bringing them closer to the observed peak. It also increased the volume output from the models thereby increasing the difference between the modeled and the observed volumes (Figure C-1). Percent error for peaks and volume for each site and optimization can be found in Table 18. The 10-meter model predicted closer values to that of the major observed peak but not the minor peak. The LiDAR model also did a better job at predicting volume. Both modeled flows had longer rising and falling limbs in their hydrographs. They reacted quicker to the precipitation but did not rise as steeply as the observed flow. This leads to higher volume outputs despite smaller peaks. The peaks for the LiDAR and 10-meter models were off by 30 and 40 minutes, respectively, and occurred ahead of the observed value. Nash-Sutcliffe  $E$  and  $E_m$  values were all above zero (

Table 19).

Throughout the December 5<sup>th</sup> event a total of 0.30 in (7.62 mm) of precipitation fell as rain leaving the observed flow with two peaks occurring at 8:20 am and 12:30 pm. Optimization of the storm increases modeled peaks significantly when only increasing output output volumes slightly (Figure C-6). Optimization also increases the steepness of the raising and falling limbs of the hydrograph for both models. It does not, however, reduce the third significant peak that occurs in both models but is very small in the observed data. The models look similar to the observed flow except for the occurrence of this third peak (Figure C-6). The observed flow does not react to the last bout of rain in the same way that the modeled values do. Volumes of the LiDAR and 10-meter modeled outputs are almost twice that of the observed and the 10-meter model does slightly better at predicting it (Table 18). Both peaks for both models occurred at the same time as the observed peak. Nash-Sutcliffe efficiency values were positive for both models and showed improvement with optimization (

Table 19).

Table 18: Percent error for peak flow rates and volume outputs for LiDAR and 10-meter model outputs.

Site	Date	Start Time	Major/Minor Peak	LiDAR Peak Error (%)	10 m Peak Error (%)	LiDAR Volume Error (%)	10 m Volume Error (%)
SY	3/15/03	0:20		23	2	45	84
	7/23/03	11:30		57	46	33	66
	7/31/03	13:00		34	80	209	305
	8/21/03	4:20	Major	57	32	119	188
			Minor	24	7		
	5/27/04	21:40	Major	54	40	32	58
			Minor	18	22		
	7/22/03	15:50		16	5	63	59
	7/27/03	13:10		54	46	7	2
	8/1/03	17:20	Major	42	41	27	22
			Minor	48	42		
	12/5/03	7:10	Major	25	27	94	83
			Minor	8	8		

Table 18: Percent error for peak flow rates and volume outputs for LiDAR and 10-meter model outputs (continued).

Site	Date	Start Time	Major/Minor Peak	LiDAR Peak Error (%)	10 m Peak Error (%)	LiDAR Volume Error (%)	10 m Volume Error (%)
------	------	------------	------------------	----------------------	---------------------	------------------------	-----------------------

O3	4/16/03	13:50		67	78	35	62
	4/28/03	4:10	Major	81	88	38	64
			Minor	66	78		
	7/23/03	14:30		77	92	48	63
	8/21/03	11:20		64	85	166	6
	8/21/03	18:50		2	65	675	101
	2/16/04	8:00		478	222	1248	682
	2/17/04	23:20		335	183	1198	689
	5/27/04	22:40	Major	32	14	452	251
			Minor	25	16		
GE	2/16/04	7:00	Major	47	4	46	261
			Minor	36	2		
	2/25/04	9:00		21	136	1766	4116
	3/26/04	9:00		43	14	13	98
	5/11/04	4:00		104	200	120	438
	5/27/04	21:00	Major	1	89	104	381
			Minor	32	19		

Table 19: Nash-Sutcliffe Efficiency  $E$  and  $E_{ln}$  values for LiDAR and 10-meter models.

Site	Date	Start Time	LiDAR $E$	10 m $E$	LiDAR $E_{ln}$	10 m $E_{ln}$
SY	3/15/03	0:20	0.55	0.44	0.55	0.50
	7/23/03	11:30	0.19	0.22	0.42	0.35
	7/31/03	13:00	-1.70	-2.85	-0.40	-0.97
	8/21/03	4:20	0.00	-0.25	-0.13	-0.54
	5/27/04	21:40	0.52	0.43	0.48	0.33
	7/22/03	15:50	0.54	0.78	0.61	0.83
	7/27/03	13:10	0.74	0.84	0.80	0.90
	8/1/03	17:20	0.62	0.66	0.59	0.64
	12/5/03	7:10	0.36	0.46	0.24	0.35
	O3	4/16/03	13:50	0.10	-0.03	0.12
4/28/03		4:10	0.15	-0.02	0.21	0.03
7/23/03		14:30	0.16	0.12	0.12	0.36
8/21/03		11:20	-0.55	0.17	-1.09	0.22
8/21/03		18:50	-8.26	0.15	-7.83	0.08
2/16/04		8:00	-136.92	-37.10	-91.20	-29.78
2/17/04		23:20	-129.78	-41.21	-110.13	-37.74
5/27/04	22:40	-3.40	-0.31	-3.31	-0.41	
GE	2/16/04	7:00	0.58	-5.06	0.59	-3.89
	2/25/04	9:00	-20.07	-93.24	-20.89	-71.13
	3/26/04	9:00	0.65	0.08	0.67	0.03
	5/11/04	4:00	-1.81	-18.61	-1.27	-14.12
	5/27/04	21:00	0.51	-4.11	0.46	-3.93

### *Osgood Ave (O3)*

A total of 0.29 in (7.37 mm) fell during the May 27<sup>th</sup> optimization storm event as rain. Optimization for both models improved all peak values as well as the output volumes (Figure C-10). For this storm event, the 10-meter model provided closer values to the observed than the LiDAR model. LiDAR over predicted the flow values. The observed hydrograph showed much flashier reaction to the precipitation than either of the modeled hydrographs. As a result of its much shorter rising and falling limbs, volume output was much lower than the models suggested. In fact, during a period of light to no precipitation, the observed flow shows that flow ceases completely for a period before starting again. This does not transpire in either model. The 10-meter model did a better job of predicting peak flow and volume (Table 18). Despite improvements with optimization,  $E$  and  $E_m$  values remain below zero for both models (Table 19).

### *Glorene and Eighth (GE)*

During the May 27<sup>th</sup> storm used for optimization at Glorene and Eighth 0.39 in (9.91 mm) of (9.91 mm) of precipitation fell in a thunderstorm. This resulted in an observed flow with two two peaks surpassing 0.2 cfs (0.0057 m<sup>3</sup>/s). Optimization slightly increases the peaks and reduces reduces volume for the LiDAR improving the shape and fit of the model (Figure C-18). The 10-meter model values are drastically reduced in both peak and volume. The optimization does not improve the shape of the falling limb of the hydrograph leaving it falling much too slow to match the observed flow. The modeled flows have a small bump in flow at the start of the flow event that is not reflected at all in the observed flow (Figure C-18). The LiDAR model results in a first peak that is too low but a second peak that matches almost perfectly. In contrast, the 10-meter model results in a first peak that is similar to the observed and a second peak that is much higher. As a result the percent error in volume is lower in the LiDAR model (Table 18). Nonetheless, higher low flows and longer, slower trailing limbs on the hydrographs mean both models predict larger volume output than observed. Only the LiDAR  $E$  and  $E_m$  values of 0.51 and 0.46, respectively, are greater than zero for this model (

Table 19). Both the 10-meter model efficiency values are negative.

### **Model Outputs**

All models displayed some amount of differentiation from the observed flow data. Model results for SY appeared visually similar to observed flows during most storm events (Figure C-1 to Figure C-9). Nash-Sutcliffe efficiency values suggest that overall storms from site SY set A were represented better by LiDAR modeling while storms from site SY set B were represented slightly better by 10-meter DEM modeling (

Table 19). Site SY set B models have the best  $E$  and  $E_{ln}$  values of all sites.

Sites O3 and GE did poorly in comparison to site SY. Site O3 had some visual similarities of similarities of observed flows (Figure C-10 to Figure C-17). General shape of the output flow was similar to that of the observed flow however volumes and timings differed considerably. Percent error in peak rate and volume was fairly high for both models in all but two events (Table 18). LiDAR generally showed lower peak rate percent error while the 10-meter models showed lower volume percent error more often. O3 has the worst  $E$  values for some of its events. However, five out of eight storm events showed positive  $E$  values in at least one model (

Table 19). Three of these sites performed better with the LiDAR model.

Results for GE also had some visual similarities in flow pattern to observed flows although there although there was more separation of peak timing and volume and they did not perform as well as well when using the Nash-Sutcliffe Efficiency values (Figure C-18 to Figure C-22). Three storm events had efficiency values greater than zero for LiDAR models while only one of these storms had positive  $E$  and  $E_m$  values for the 10-meter model (

Table 19). LiDAR models showed greater values of  $E$  and  $E_{ln}$ . Percent error in peak rate and volume was only better in two for the five storms with LiDAR models.

### **Individual Storms**

#### *South Lake Tahoe Y: Group A*

The March 15<sup>th</sup> storm comprised of 0.89 in (22.61 mm) of rain/snowmelt that fell over a 12:30 over a 12:30 hour period (Figure C-2). Modeled data matches this first peak fairly well. The observed dataset has a significant gap that missed the second peak displayed in the models completely. Efficiency values and percent error calculations were carried out only on the period with observed data available. Modeled volume outputs were still higher than observed. LiDAR models had less percent error in volume but more percent error in peak than the 10-meter model. The LiDAR model received the positive  $E$  and  $E_{ln}$  values while the 10-meter model did not (

Table 19).

During the July 23<sup>rd</sup> the timing of the peak was similar to observed flows but the peak flow was underestimated (Figure C-3). A total of 0.37 in (9.40 mm) of precipitation fell during this thunderstorm. Despite smaller peaks in the July 23<sup>rd</sup> event, both LiDAR and 10-meter DEM models predicted a larger volume than the observed. Modeled peaks occurred slightly after the observed peak. They began to rise around the same time as the observed flow, but the observed flow climbed more quickly and dropped just as quickly. The 10-meter model had a lower error peak and the LiDAR model had a lower error in volume (Table 18). Nash-Sutcliffe efficiency values indicate that LiDAR model did better at predicting low flows with a positive  $E_b$  value of 0.42 but the 10-meter model predicted high flows better with a positive  $E$  of 0.22 (

Table 19).

The July 31<sup>st</sup> event had the opposite problem occur. With the LiDAR model at 12.59 cfs (0.36 m<sup>3</sup>/s) and the 10-meter DEM model at 16.93 cfs (0.48 m<sup>3</sup>/s), both modeled peaks were much higher than the observed peak of 9.39 cfs (0.27 m<sup>3</sup>/s) (Figure C-4). During this thunderstorm, 1.04 in (26.42 mm) of rain fell. LiDAR models had less percent error in both peak rate and volume output. Both models got negative  $E$  and  $E_m$  values the LiDAR model with doing slightly better than 10-meter model (

Table 19).

During the August 21<sup>st</sup> thunderstorm 0.6 in (15.24 mm) of rain fell. The rain fell in two bouts in two bouts leaving the flows with two sharp peaks (Figure C-5). The observed outflow rises and falls much faster than either model and flow disappears completely between to two peaks. This doesn't occur with either of the higher volume modeled flows. Percent error in peak rate is lower for the 10-meter model while percent error in volume is lower for the LiDAR model (Table 18). All models have negative  $E$  and  $E_{in}$  values except for the  $E$  value for the LiDAR model which is zero (

Table 19).

*South Lake Tahoe Y: Group B*

The modeled flows for the July 22<sup>nd</sup> storm event match very closely with the observed flow observed flow (Figure C-7). During this thunderstorm 0.26 in (6.60 mm) of rain fell. Models predicted similar peak values to the observed flow. They also predicted similar volumes although the drop in flow took longer and thus the volume was overestimated. The 10-meter model got slightly closer and had less error in peak rate and volume (Table 18). They had very good Nash-Sutcliffe efficiency values for both models (

Table 19).

On July 27<sup>th</sup> a thunderstorm dropped 0.17 in (4.32 mm) of rain. The models predicted peaks well below the observed peak but at a very similar time (Figure C-8). Both modeled peaks are about half the value of the observed peak. Despite lower peaks, volume outputs match pretty closely. Both models have good efficiency values (

Table 19). The 10-meter model did slightly better than the LiDAR model all around for this storm.

A total of 0.13 in (3.30 mm) fell on August 1<sup>st</sup> thunderstorm resulting in an outflow with two outflow with two major peaks. The models react to early precipitation much more than the the observed flow resulting in two mini-peaks displayed in both models (Figure C-9). The modeled peaks are a little over half of the observed peaks. Despite lower peaks, they rise and fall and fall more slowly and have slightly higher predicted volume output. The 10-meter model had model had only slightly less percent error in peak rate and volume output (Table 18). Nash-Sutcliffe efficiency values for both models are positive and very similar with a slightly higher value for the 10-meter model at 0.66 (

Table 19). LiDAR only receives an  $E$  value of 0.62.

*Osgood Ave*

In the February 16<sup>th</sup> storm event, 0.81 in (20.57 mm) of precipitation fell taking the form of rain the form of rain on snow. The modeled flows for this storm have the same general shape as the as the observed flow but at a much large magnitude (Figure C-11). The LiDAR results in values that are almost twice that of the 10-meter model which is already much greater than the observed values. The poor modeling is reflected in the lowest  $E$  and  $E_m$  values of all the models and equally poor percent errors (Table 18 and

Table 19).

Figure C-12 depicts flow for the observed and modeled event of the February 17<sup>th</sup> storm. This storm has 0.37 in (9.40 mm) of precipitation occurring as rain and graupel in two periods over 15 hours. The modeled flows maintain some of the same peaks as the observed flow but both react with much greater magnitude than the observed flow. Again, the LiDAR model predicts higher peaks and volumes than the 10-meter model (Table 18). As with the February 16<sup>th</sup> event, all the efficiency values are negative (

Table 19).

In contrast to the previous two storms, the April 16<sup>th</sup> event observed flow has a greater magnitude greater magnitude than either of the models for the same event (Figure C-13). The flow for the two models have some similarities in shape with the observed but the observed flow changes much more rapidly with higher peaks and steeper rising and falling limbs for each peak. Despite this, the LiDAR model still produces an  $E$  value of 0.30 and the 10-meter model has an  $E$  value of 0.09 (

Table 19).

The April 28 storm event models do not appear similar to the observed flow (Figure C-14). The storm contained 0.22 in (5.59 mm) of precipitation as rain/snowmelt. The observed flow reaches much higher peaks and volume than either model output. Of the two models, LiDAR values are closer to the observed than the 10-meter model. The LiDAR model results in a positive  $E$  value of 0.15 and a  $E_{ln}$  value of 0.21. The 10-meter model efficiency values are very close to zero (

Table 19).

The July 23<sup>rd</sup> event is classified as a thunderstorm and 0.88 in (22.35 mm) of precipitation fell. The general shape of a single major peak is maintained in both models but the peaks of the modeled events are much lower than the observed (Figure C-15). Despite the lower peak, the LiDAR model predicts a higher volume output due to its longer falling limb. The 10-meter model also has a slower rising and falling limb of its hydrograph, but the peak is so much lower than the observed, that the predicted output volume is also significantly lower than the observed. According to efficiency values, LiDAR does a slightly better job at predicting the peak flows than the 10-meter model but does not do as well with low flows represented by  $E_{ln}$  (

Table 19).

The thunderstorm that happened on August 21<sup>st</sup> at 11 am dropped 0.19 in (4.83 mm) of rain that mostly fell during a single 10-minute period. Similar to the July 23<sup>rd</sup> event, the general shape of the modeled flow is similar to the observed flow but the modeled peaks are not at high and the flow rises and falls slower than the observed (Figure C-16). The rising limbs of the modeled flows do not climb as quickly nor do the falling limbs drop as quickly as the observed. The lower peak of the 10-meter model produces a very similar volume output to the observed with little percent error. While the LiDAR model peak is closer to that of the observed, it also has a volume of almost three times the size. The 10-meter model has a both positive  $E$  and  $E_{ln}$  values. LiDAR efficiency values are both negative (

Table 19).

The second thunderstorm to occur on August 21<sup>st</sup> began at 6 pm and dropped at total of 0.33 in total of 0.33 in (8.38 mm) of rain (Figure C-17). Again, most of this rain fell during a single 10-minute period. The LiDAR modeled event reached a similar peak value to the observed although it took longer to reach the peak and for the falling limb to drop resulting in a very high volume. It has less than 2% error in peak but over 675% error in volume (Table 18). The 10-meter model did not even get close to the peak value and still had a long trailing limb. This resulted in higher volume as well, although not as high as the LiDAR model predicted. The Nash-Sutcliffe efficiency calculations only resulted in positive values for the 10-meter model (

Table 19). Both LiDAR values were negative.

*Glorene and Eighth*

Modeled and observed flow for the February 16<sup>th</sup> storm can be found in Figure C-19. During the storm 1.12 in (28.45 mm) of precipitation fell in the form of rain on snow. The observed data has many more spikes in flow than either of the models making it difficult to define a single peak event. Two peaks were identified for comparative purposes at 12 pm and 2:45 pm. The LiDAR-modeled flow appears to follow the observed values much closer in magnitude although it does have a longer trailing limb. This is reflected in its improved similarity in volume output compared to the 10-meter model. In contrast, the 10-meter model matches peak values more closely. Despite the lower peaks, the visual comparison of the LiDAR outflow is held up by the  $E$  and  $E_{ln}$  values with 0.58 and 0.59 for LiDAR (respectively) and -5.06 and -3.89 for the 10-meter model (model (

Table 19).

Both the models very poorly represent the February 25th storm event (Figure C-20). In this storm a total of 2.74 in (69.60 mm) of precipitation fall in the form of snow or snowmelt over 11 hours. The LiDAR model produces the peak most similar to the observed flow with only 21% error. However, peaks for both models occur over three hours before the observed peak. Furthermore the total modeled volume is grossly exaggerated with values for the LiDAR and 10-meter models surpassing 28,000 ft<sup>3</sup> while the observed value of only reaches 1,517 ft<sup>3</sup>. All this cumulates very bad percent error in volume and poor  $E$  and  $E_m$  values for both LiDAR and 10-meter models (

Table 19).

The modeled values for March 26<sup>th</sup> storm visually appear to poorly match the observed flow (Figure C-21). There is a large portion of the observed flow not represented in the models or in the precipitation. In this event, only 0.18 in (4.57 mm) of precipitation fell as snow or snowmelt. There is one major peak that occurs in all three flows. This peak alone is used for percent error and Nash-Sutcliffe efficiency values. The 10-meter model has the most similar peak but more error in volume than the LiDAR model (Table 18). The LiDAR model has  $E$  and  $E_{ln}$  values above 0.6 while both 10-meter model efficiency values hover around zero (

Table 19). It is worth noting that the observed flow drops very quickly with no trailing limb. It falls from 0.219 cfs (0.0062 m<sup>3</sup>/s) to zero in one 10-minute step while both the models trail off slowly.

Both of the models for the May 11<sup>th</sup> storm result in a much greater flow than the observed (Figure C-22). The storm comprises of 0.43 in (10.92 mm) of precipitation in the form of snow and snowmelt over almost 4 hours. Both models have higher peaks and longer trailing limbs than the observed. As a result the observed volume is less than half the amount of the volume for the LiDAR model and more than five times smaller than the 10-meter model. It is not surprising that the percent error for both peak flow and volume is high for both models (Table 18). The observed flow also has a small amount of flow that occurs before even the precipitation that is not reflected in the models. Although LiDAR does slightly better with efficiency values, all efficiency values are negative for the models (

Table 19).

## DISCUSSION

### Classification

The land use classification image had an overall accuracy of 75.9% (Table 13). The bush class had the least accuracy and was usually confused with trees or grass. Dirt, grass, and trees also did not reach accuracies above 90 and were confused with each other. Luckily, the model was interested in impervious or pervious land cover. With these classes grouped together as ‘pervious’ and the building and road classes grouped as ‘impervious’, accuracies improved reaching 97% users accuracy in the impervious class (Table 14). This indicates it is acceptable to use the classification to identify impervious surfaces for the model.

A number of issues arose during the classification process that can account for any inaccuracy. LiDAR data received did not come with a high-resolution aerial image. NAIP images were selected from the closest date to the flying of the LiDAR available. NAIP images were flown in 2010 on days with low cloud cover and the LiDAR data was flown between August 11<sup>th</sup> and 24<sup>th</sup> of the same year. Although it is possible there were some changes between when the data was taken, they are likely minor and have little effect on the study sites. The images were not ground-truthed to each other and thus their alignment did not match exactly. In some locations trees or building heights were offset slightly from the same objects in the aerial image. This in part could be due to

georeferencing or reprojection that was required to mosaic the images together. This affected the classification results, which weighed more heavily on the NAIP imagery.

High-resolution NAIP images were used to match the higher resolution LiDAR DEM. However, this introduced shadows into the process. A shadow is an area of no data in the image. The classification relied on neighboring pixels, LiDAR-derived height information and other data sources to fill in shadowed areas using neighborhood analysis and expert knowledge.

Additionally, this study focused on surface land use. Aerial images, taken from above, inherently do not depict land cover underneath tree canopy. The large amount of tree cover in this region made surface identification more difficult. Trees overhanging roads, buildings and other impervious areas affected the final amount predicted. This was somewhat mitigated by burning the road layer directly into the classified image. The road layer used was older than other data sets. However, careful inspection insured the layer matched the 2010 data as best as possible.

### Flow Analysis

Pourpoint location is a key aspect in identifying the correct contributing area for an outlet. This study found differences between site locations received with the flow data, those identified during on-site visits and pourpoints used in the DEM flow analysis (Table 7, Table 15). Error in the creation of GPS points and projection conversions could account for the difference. Additionally, onsite identification of location relied on visual identification of an outlet location. Exact point of the flow monitoring station could vary

within the culvert. For the model, outlets had to match up with a flow path from the DEM being used. This differed between the LiDAR and the 10-meter DEMs. Shifting the location of the outlet to align with a flow path can significantly alter basin size and shape but is necessary for the ArcMap flow analysis process.

There were also differences between areas calculated through the ArcMap flow analysis process and those received from the TMDL study. It is unknown how the received areas were calculated or where boundaries for their watershed lay. Thus areas calculated in ArcMap were used for the study. Variations in area, especially on the scale observed, could indicate a source of error. However since given areas are of unknown origin, it is unclear which better represents the actual basin area or if the error is from the TMDL calculations or mine.

Some selective editing based on South Lake Tahoe stormwater drainage maps was used to improve basin boundaries. Human influence to the flow path was appraised based on a map of the drainage systems provided by the city of South Lake Tahoe Public Works Engineering Division (AIMS). The map is an estimate and has not been quality controlled. However, it is the only available data of this type, and since drainages could be greatly affected by man-made drainage locations within each basin. Slight alterations in drainages were made based on these maps with consideration of potential errors (Figure 11).

Different projections of the DEM (NAD 83 and Albers) resulted in slightly different shapes and sizes of the drainage basins. Calculations in the reprojection process altered some of the elevation values enough to change the flow direction. This would be

less likely to happen on very defined landscape where the changes in elevation were greater. Despite a potential introduction of error, layers were reprojected into Albers Equal Area Conic projection to preserve area. Table 6 has details on the specific Albers projection used as it was modified to focus on the study site.

### **Flow Patterns**

Higher density of drainages, and greater detail in regards to flow paths greatly improves our knowledge of how water travels over the landscape. Figure 15 shows identified drainage pathways that collect an area of 500 m<sup>2</sup> or more for both LiDAR and the 10-meter DEM. The LiDAR drainage network had a drainage length to basin area ratio of 0.066 for a one square kilometer area centered over site GE. The same area had a ratio of 0.056 for the 10-meter drainage network. For the sites themselves, drainage densities remain similar although there is more variation observed in the 10-meter sites (Table 16). While there is not a large difference between these ratios, the reasons for these densities are different.

LiDAR drainages are more sinuous, moving around object and following small depressions in the landscape (Figure 15). They follow along roads, around buildings and down man-made drains. Alternatively, the 10-meter drainages often flow parallel to each other before meeting. They show a general flow path but loose the intricate detail of the landscape. This would work well at a larger scale or within steep basins. However, the basins in this study are relatively small and flat.

LiDAR could vastly improve our ability to identify areas where flow gathers after traveling over impervious surfaces for long distances. With this information, locations for water detention ponds and other runoff treatment structures could be effectively located. Our ability to draw these pathways can be used visually by water managers in situations where detailed accounting of where water has been is important. Incorporating LiDAR's highest hit landscapes by using building rooftops in a flow pattern could further improve management of small urban basins in detaining runoff for pollutant detainment. Another possible application of this is locating areas of improved infiltration where water naturally will flow and collect. Identifying these areas for recharging groundwater could be very important, especially in the current drought.

### **Basin Differences**

Differences in computed results are likely due to differences in basin delineation and a result of the differences in elevation values between the two data sets (W. Scharffenberg, HEC-HMS Lead Developer, personal communication, May 27, 2015). In general, the 10-meter DEM resulted in fewer drainage lines but collected runoff from a larger area. Site SY has the smallest basin size difference between the 10-meter and LiDAR basins. They still have a percent difference of 20 percent. Sites O3 and GE have percent differences in size of 38 % and 80 % respectively. Exact basin sizes can be found in These flow patterns also resulted in different sizes and shapes of the basin contributing to each outlet (Figure 13). The 10-meter derived basins were larger than LiDAR derived basins at the same site (Table 17). Site GE showed the largest discrepancy between basin

sizes. Despite larger basin sizes, sites SY and O3 had lower percentages of DCIA in the 10-meter basins than in the LiDAR basins (7.7 % and 10.9 % respectively). Site GE had a slightly higher percent DCIA in the 10-meter basin

Table 17. Larger basins produce more runoff if all other conditions are the same. Since 10-meter derived basins were larger, you would expect to see larger volume outputs in 10-meter models. In two of the three basins, SY and GE, LiDAR has lower flow peaks and less output volume. The two models are closest in output in site SY where basin size and shape were also the closest in size. The third basin, O3, has other hydrologic mechanisms acting on the model flow that could contradict the effects of basin size. Site O3 had the most differences in shape, basin location, drainage pattern and flow line lengths. These inconsistencies could account for lower volumes in the 10-meter model than the LiDAR model.

The 10-meter basins also tended to be slightly less sinuous than LiDAR derived drainages (Figure 15). A large part of this is due to the fact LiDAR flow lines follow road borders instead of crossing them. This resulted in longer flow lengths in LiDAR networks than in 10-meter networks (These flow patterns also resulted in different sizes and shapes of the basin contributing to each outlet (Figure 13). The 10-meter derived basins were larger than LiDAR derived basins at the same site (Table 17). Site GE showed the largest discrepancy between basin sizes. Despite larger basin sizes, sites SY and O3 had lower percentages of DCIA in the 10-meter basins than in the LiDAR basins (7.7 % and 10.9 % respectively). Site GE had a slightly higher percent DCIA in the 10-meter basin

Table 17). In most cases the added sinuosity likely matched truth better than the 10-meter DEM representations. There were also drainages that appeared more sinuous than they should be. These were located in areas where the drainage crossed land that was not built up. On-site inspection of some of these locations indicates that these drainage channels, although possibly modified, mimic natural stream patterns. However, LiDAR flow patterns were more sinuous than observed at these sites. The added sinuosity could affect initial model parameter estimates and the timing of the output hydrograph.

Sinuosity, drainage density and basin size can all effect how runoff reaches the outlet. Greater sinuosity increases lag time from the subbasins to the outlet, which could affect the synchronicity of the basin. Depending on the timing, this would either increase peaks and make hydrographs sharper with increased synchronicity or decrease and flatten them with decreased synchronicity. Higher drainage density can increase the amount of runoff reaching an outline. The way the model is structured, once the runoff reaches a drainage line, infiltration and other factors of attenuation no longer play a roll. The water is transported in full to the outlet. Higher density of drainage lines would allow more of the precipitation to reach the outlet. Other, more complex reach transport methods could alter the roll of this in the model by allowing water in the reach to be lost to evapotranspiration or infiltration.

### Modeling

Overall, models reacted fairly similarly using LiDAR or 10-meter models. There is some variation in peak height, volume and timing but overall shape and start of flow

remains consistent between the two models. In most cases when the models differed dramatically from the observed flow, both did so in the same way. This indicates that for these events, there is some piece of missing information from the storm or in the model setup that gets reflected in both models.

### **10-meter vs. LiDAR**

At site SY, LiDAR and 10-meter models responded similarly. In general, LiDAR models produced slightly lower peak and volumes. The 10-meter models matched a majority of the observed peaks better but less than half of observed volumes (Table 18). The December 5<sup>th</sup> optimization and storm events had the most effective modeling with all storms and both models reaching  $E$  and  $E_{ln}$  values above 0.3 with the 10-meter models consistently reaching higher efficiency than LiDAR. LiDAR consistently predicted volumes in the May 27<sup>th</sup> optimization storm set better. This site, through both storm sets, had the most similar peaks, volumes and efficiency values. It also has the best match in basin size. The 10-meter model was only 9.9% larger than the LiDAR model. The larger basin size of the 10-meter model would result in larger volumes. However, there was 10.9% more DCIA in the LiDAR basin than in the 10-meter basin. This could offset the size difference, as it would also lead to higher volumes.

At site GE discrepancy between models was much greater. For this site the 10-meter basin was much larger than the LiDAR basin. While over half of the peaks had a lower percent error than the LiDAR model, low flows were not predicted as well in this model and in only one of the five events did the 10-meter model have lower percent error

in volume than the LiDAR. Even though the Nash-Sutcliffe values for this site were not all positive, for all five events at site GE both the  $E$  and  $E_{ln}$  were better for the LiDAR model. In addition, visual inspection of hydrographs indicates that at this site the LiDAR models did a better job at predicting the flow than the 10-meter models. A good example of this can be seen in the February 16<sup>th</sup> storm in Figure C-19. The prediction of basin size and flow pattern using the 10-meter DEM is likely the largest cause for this disparity. Despite its larger size, the 10-meter basin only showed an increase in percent DCIA of 0.9% (These flow patterns also resulted in different sizes and shapes of the basin contributing to each outlet (Figure 13). The 10-meter derived basins were larger than LiDAR derived basins at the same site (Table 17). Site GE showed the largest discrepancy between basin sizes. Despite larger basin sizes, sites SY and O3 had lower percentages of DCIA in the 10-meter basins than in the LiDAR basins (7.7 % and 10.9 % respectively). Site GE had a slightly higher percent DCIA in the 10-meter basin

Table 17). Although other factors are involved and will be discussed further on a more individual event basis, the improved basin definition from the LiDAR dataset is probably an important factor in why LiDAR models matched observations better at this site.

At site O3 the LiDAR models consistently show higher peak and volume estimates than the 10-meter models. A number of these storms have other issues going on that confound factors in interpretation. The 10-meter basin is larger than the LiDAR basin by 18.8% but the optimized volume was lower than the LiDAR model. Some of this reversal is the result of the optimization. The pre-optimized hydrograph for the O3 10-

meter model is slightly larger in volume and peak than its LiDAR counterpart (Figure C-1). In addition there was 7.7% more DCIA in the LiDAR basin than in the 10-meter basin (These flow patterns also resulted in different sizes and shapes of the basin contributing to each outlet (Figure 13). The 10-meter derived basins were larger than LiDAR derived basins at the same site (Table 17). Site GE showed the largest discrepancy between basin sizes. Despite larger basin sizes, sites SY and O3 had lower percentages of DCIA in the 10-meter basins than in the LiDAR basins (7.7 % and 10.9 % respectively). Site GE had a slightly higher percent DCIA in the 10-meter basin

Table 17). Furthermore, the LiDAR basin had more subbasins and drainage lines. The 10-meter model had two main drainage lines while the LiDAR model had three larger drainage lines and three smaller ones. Higher percent DICA values result in more initial runoff being modeled. The number and length of the drainage lines also affect how the runoff is transported. Once runoff enters the modeled reach no water is lost to infiltration. Together these factors could account for why LiDAR models predicted higher peaks and flow volumes than the 10-meter models.

### **Individual Storm Assessment**

There were four common types of deviance from the observed flow. These include modeled flow that rose and fell less quickly (hydrograph flashiness), had a different volume, reacted to precipitation when the observed flow didn't, or had a peak timing that was offset by several hours. In a few cases the observed flow reacted where the models did not and there was one case affected by missing data.

### *Hydrograph Flashiness*

The observed flow fairly commonly shows a slower initial response followed by a much quicker rise and fall in flow than the modeled values. Noteworthy examples include the May 27<sup>th</sup>, July 23<sup>rd</sup>, and August 21<sup>st</sup> events for site SY group A and in April 16<sup>th</sup> and 28<sup>th</sup>, May 27<sup>th</sup>, July 23<sup>rd</sup>, and both August 21<sup>st</sup> storms for site O3. These storms have higher peak values than the models predict and yet in most cases result in a lower total runoff volume.

Five of these storms are characterized by the majority of rain falling within a fairly short period of time. In these cases, peak rates can reach over twice that of predicted values and has a shorter, faster period of climb in the hydrograph. The two events on May 27<sup>th</sup>, while not thunderstorms, occur completely as rain and have fairly similar characteristics and explanations. A likely factor in the difference between observed and modeled values is that the objective function in the optimization did not reach its global minimum. This would affect the shape of the hydrographs in various possible ways including infiltration, timing, and peak values. In all these cases, the associated optimization storm has similar flow characteristics to the disparity in question. Conversely, the SY December 5<sup>th</sup> and GE optimizations did a better job of matching the simulated rate of rise and fall in flow to the observed. Storms modeled with these optimizations have better matching rise and fall flow rates. While the July 27<sup>th</sup> and August 1<sup>st</sup> storms at site SY set B show some of these traits, the difference between

modeled and observed are minor. Either using more complex optimization processes or shifting parameter start values by hand to change the local minimum the objective function is reaching could lead to an improvement in model optimization for other modeled storms.

It is possible that the difference in the type of rainfall seen in these storms made the optimization storm an ineffective choice (Snyder, 1938). Although most of these storms have a similar amount of rainfall, within 0.23 inches, of their optimization storms, rain is more spread out. Site SY and GE optimization storms, while not classified as thunderstorms, have more similarity in precipitation pattern with a thunderstorm than O3. The most grievous examples of the magnitude offset can be found at site O3, the most pronounced of which is on July 23<sup>rd</sup>. The SY July 31<sup>st</sup> storm and O3 July 23<sup>rd</sup> storm outstrip their optimization storm in rainfall by over half an inch and are, respectively, the most poorly matched in terms of rise and fall for their grouping. Model optimization should be performed on a storm of similar return frequency to have the best results (Snyder, 1938). Using a thunderstorm with similar rainfall patterns as an optimization storm might be able to improve the models.

The shape of the observed storms in these cases suggests a couple of other possibilities. Higher magnitude and quicker rise and fall in flow in observed storms compared to predicted values could be indicative of poor accounting of directly connected impervious area. These examples show higher peak rates and steeper climbing and falling hydrograph limbs that are generally accompanied by greater amounts of DCIA (Lee and Heaney, 2003). While this may be the cause of at least some of the

discrepancy at site O3, the use of this explanation at site SY is belayed by the fact that storms in set B, using the same DCIA values, basin size, and flow patterns as those in set A, do not show the same extent of disparity between observed and predicted flow.

While this same explanation prevents erroneous basin shape from being seriously considered as the cause of the difference at site SY it could be affecting the shape and timing of a hydrograph at site O3. Site O3 was one of the most difficult of the three to isolate. If the basin edges were estimated incorrectly it would directly affect how the precipitation related to the hydrograph. While this type of error might be somewhat mitigated through optimization, a large enough difference in basin size could carry through and result in poor model outputs.

In addition to higher peaks and a quicker rise and fall in flow, the storms on April 16<sup>th</sup> and 28<sup>th</sup> stay well above modeled flow values until the trailing leg. Since they are not thunderstorms, the disparity between predicted and observed values have a different reason. They occur during the spring months and while they are rainstorms, they could include snowmelt. Peaks do not appear to have a close correlation with the timing of precipitation, likely complicated by the melting snow pack. This was not accounted for in the model. A spring snowpack has rounded coarse grains and lower capillary suction to transport water (Singh et al., 1997). However, it would likely have already gone through some metamorphosis and been conditioned to create preferential flow pathways (Singh et al., 1997). This would speed transportation of rain and melt water through the snowpack and reduce storage capacity (Singh et al., 1997; Wever et al., 2014).

Rain falling on snow can trigger large melting events especially in shallow snowpacks (Wever et al., 2014; Singh et al., 1997; Berris and Harr, 1987). The latent heat exchange from the condensation of water vapor onto the snow pack has more effect than the temperature of the rain, so melting events can occur even at fairly cold temperatures (Marks et al., 1998). Lundquist et al. (2008) found that when temperature is between 2.5 °C and 3 °C snow was equally likely to melt or accumulate. On April 16<sup>th</sup> 2003, the storm occurred between 3 pm and 11 pm and the peak temperature for that day was 2.8 °C as recorded at the South Lake Tahoe Airport roughly 7.5 km from the site with an elevation difference of around 20 meters (Table 20). The April 28<sup>th</sup> storm occurred between 2 am and 2 pm and temperatures ranged from a low for the day of -2.8 °C to a high of 5 °C (Table 20). Both storms could potential be a rain-on-snow event. Rain-on-snow events increase flow magnitude and the rate of rise in flow. As snowmelt is not included in the modeling, predicted values fail to reach peaks found in the observed flow.

There are two storms that stand out as unusual in regards to the rise and fall rates and magnitude of the hydrograph. The O3 May 27<sup>th</sup> storm observed data appears to be very flashy compared to its modeled counterparts (Figure C-10). However, the 10-meter model peaks match very well and LiDAR peaks aren't too far above them. If it weren't for the extremely quick drop in observed flow (dropping to zero at two points in the storm hydrograph) volumes might be similar to the modeled flow. This variation in the pattern could result from the optimization performed on this storm. Modeled peaks could have been brought close to the observed while global minimums for other parameters, such as infiltration, were not obtained. Since the objective function used focused on peak

values, it is likely the most accurately optimized parameter. Additionally, some other form of runoff detention or interception could play a role here.

Table 20: Maximum and minimum daily temperature for relevant dates recorded at South Lake Tahoe Airport station (USW00093230) at an elevation of 1924.5 m.

<b>Date</b>	<b>Max Temperature (°C)</b>	<b>Min Temperature (°C)</b>
3/15/03	3.9	-4.4
4/16/03	2.8	-5.0
4/17/03	5.6	-2.2
4/28/03	5	-2.8
7/22/03	31.7	10
7/23/03	27.2	13.9
7/27/03	26.1	11.1
7/31/03	26.7	12.8
8/1/03	22.2	10
8/2/03	17.2	10
8/21/03	17.8	12.2
8/22/03	21.1	9.4
12/5/03	9.4	5.6
2/16/04	7.2	0
2/17/04	7.8	0.6
2/18/04	2.8	-2.8
2/19/04	4.4	-8.9
2/25/04	5	-2.8
2/26/04	-1.1	-8.3
3/26/04	3.3	-7.2
5/11/04	8.3	-2.2
5/27/04	19.4	5.6
5/28/04	11.7	1.7

In the SY July 31<sup>st</sup> storm the magnitude of the modeled output is larger than the observed despite the quicker falling hydrograph of the observed. In this case, the peak values of both the models are much higher than the observed. This storm does not match the pattern or behavior observed in other thunderstorms. As the hydrograph rise begins at a similar time and slightly steeper rate, it is unlikely that initial loss or higher infiltration rates are the influence here. It is possible that some temporary detainment of water or other diversion reduced the size of the observed peak.

#### *Flow Volume*

A second common occurrence is a predicted flow that differs in volume greatly from the observed flow. In the events mentioned above, storm peaks exceeded modeled peaks but observed low flows also fell below modeled low flow. There are also five storms where the modeled flow values exceed the observed values consistently throughout the hydrograph leading to significantly larger predicted volume than observed. These storms are the February 16<sup>th</sup> and 17<sup>th</sup> events at site O3 and the February 16<sup>th</sup> and 25<sup>th</sup> and May 11<sup>th</sup> events at site GE. During the GE February 16<sup>th</sup> storm, the LiDAR model predicted flow values fairly well. Only the 10-meter model predicted much higher volumes.

These storms occur in winter and spring. Precipitation fell as rain on snow, snow, or snowmelt. Even the May 11<sup>th</sup> storm had rain and grauple indicating some amount of the potential runoff remained frozen. Excluding potential timing errors and flow values, the general shape of the hydrographs was similar between observed and simulated flows

and there appears to be some correlation between peaks and precipitation. The difference in magnitudes could indicate that some of the potential runoff froze and remained frozen throughout the time period of the storm. When cold rain falls on snow, especially in newer snow packs when little compaction has taken place, the water can be absorbed by capillary suction and held within the snow pack and even to a lesser degree frozen (Wever et al., 2014). Fresh snow can absorb a large amount of rainwater before runoff begins (Singh et al., 1997). When temperatures fall below 0 °C there is a 90% precipitation will fall as snow and snow will accumulate (Lundquist et al., 2008). It isn't until temperatures reach 3 °C that there is a greater change precipitation will fall as rain instead of snow and melt will occur (Lundquist et al., 2008). While maximum temperatures for all but one these storms reach above 3 °C, minimum temperatures are near or below 0 °C (Table 20). Times with most observed flow occur at a time of day when maximum temperatures are most likely reached. They correspond in length to periods where temperature was probably above 3 °C. Only the O3 February 17<sup>th</sup> storm does not have a max temperature above 3 °C. Although it starts on the 17<sup>th</sup>, which was a fairly warm day, the majority of the storm occurred on the 18<sup>th</sup> which had a high of only 2.8 °C. This is close enough that melt and runoff could occur. Since temperature and snow aren't taken into account in the models, rainfall freezing or being trapped by snow is not reflected in the predicted flows.

Magnitude variations in the February 16<sup>th</sup> storm at site GE may have more to do with modeling error. While peaks are much spikier, the general size of the LiDAR predicted flows match well with those of the observed. The 10-meter DEM model has

much larger flow values. However, this trait can be observed in other hydrographs from the same site suggesting it is related to optimization error.

### *Flow Reaction*

In five storms the models react to a precipitation input with an increase in flow when the observed flow does not. In the August 1<sup>st</sup> and 21<sup>st</sup> and May 27<sup>th</sup> storms at site SY and the May 27<sup>th</sup> storm at site GE the incident occurs at the beginning of the event. These are rain or thunderstorms that occur in the late spring or summer months. Most likely, some infiltration or interception is not accounted for in the model. Since this is not seen consistently throughout all the storms at any one site, antecedent soil moisture is the most likely culprit. Antecedent soil moisture would be lower during this time of year when rain is less frequent, temperatures are warmer and soils are drier. The model did not vary initial precipitation loss by event and therefore did not account for any changes in antecedent moisture content.

In the fifth case, the incident occurs at the tail end of the storm (Figure C-6). This storm is also the only one of the four that happens in December. In this case, the incident occurs between 2 pm and 4 pm. The peak in flow directly before the incident at 12:30 pm was much higher and matched very well by the model. The modeled 2 pm peak is very similar to the 12:30 pm peak and is the result of a similar peak in precipitation. However, at this time the observed flow barely reaches 0.2 cfs. Temperatures did not fall below 5.6 °C that day so snow is unlikely. In other regions of the hydrograph, the models fit very well showing similar inclines and peaks to the observed. One possibility is that the

observed storm simply dropped quicker than the modeled. At the lowest point in the modeled flow between those peaks, the observed flow has already reached 0 cfs. Adding more rain on top of the higher modeled flow at this point could result in the distinctive peak variance from the observed. Even with this in mind, the second peak in the modeled flows would have been higher than the much-diminished observed peak. This also does not explain how the two observed peaks could look so dissimilar when the amount of precipitation associated with the peaks is only 0.01 inches different. Since these basins and drainages are small, a relatively small disturbance could cause a significant change in flow. Most of the drainages are open to the air. As such, it would be easy for someone to leave an obstacle in one of the drains that either increased depression storage or diverted flow out of the drain.

### *Storm Timing*

Error in peak timing is common and can be expected as a result of variation in rates of rise and initial reaction times. These can vary by 20 or 30 minutes on either side of the observed peak. A number of storms had a difference in peak timing great enough to be attributed to something else. In at least four cases, the peak observed flow even occurs before the peak observed precipitation. These include the March 15<sup>th</sup> and August 21<sup>st</sup> storms at site SY and the February 16<sup>th</sup> and May 11<sup>th</sup> storms of site GE. These storm peaks are ahead of the precipitation peak by an estimated one-hour.

The observed flow data falling ahead of the observed precipitation suggests that this fault lies not with the models but within the data set itself. The models use a single

precipitation gage for each storm. Precipitation can vary within a basin. However, in this model, basin size is very small and it is unlikely there is much variation within the basins themselves. Also, the basins are between 600 meters and 4.6 km from the gage sites (Table 9). The site furthest from its associated precipitation gage (site O3), and thus the most likely to have variation from precipitation noted, did not have many examples of a distinct timing error. While some variation in timing could occur between these sites, for the peak flow to transpire an hour before the brunt of the rainfall is unlikely at that distance. The fact that these storms are consistently off by one hour suggests that some human error is involved. As the objective function did not focus on peak timing, and therefore timing might be expected to be less accurate in predicted peaks, it is simple to correct the observed time by one hour and compare models to the reevaluated observed hydrographs.

Although peaks appear out of sync in the February 16<sup>th</sup> and April 16<sup>th</sup> storms for site O3 as well, storm type and complexity reduces the certainty of a peak timing delay. Peaks fit with the rest of the data better when delayed by one hour but complexity of the hydrograph in relation to the precipitation type means there is less certainty as to whether the discrepancy can be considered data error or whether it is a result of weather patterns. Therefore, for these storms, precipitation and flow timings were not modified before evaluation.

In the April 28<sup>th</sup> storm of site O3 and February 25<sup>th</sup> storm of site GE the observed peak flow occurs considerably after the peak precipitation and the predicted peaks. The models follow general shape of the observed hydrograph but they contain much larger

flows and occur about three hours before the observed (Figure C-20). The observed peak occurs at almost 6 pm, when temperatures have probably already dropped below the day's maximum of 5 °C. However, meltwater or precipitation can take a long time to make its way through the snowpack and to the drainage. Additionally, fresh snow can detain a lot of that water (Singh et al., 1997; Wever et al., 2014)

The April 28<sup>th</sup> storm is listed as rain/snowmelt. Precipitation begins at 4:10 am and over half of the storms precipitation falls before 6 am (0.12 in). On April 28<sup>th</sup> a high of 5 °C and a low of -2.8 °C were recorded at the South Lake Tahoe Airport approximately 2.9 km from site GE (Table 20). Since the storm began in the early hours of the morning when temperatures were still likely below 0 °C, it is possible the early precipitation fell as snow. Around the globe, 90% precipitation falls as snow below 0 °C and 90% falls as rain above 3 °C (USACE, 1956). At an air temperature of 1.5 °C, only 50% of precipitation events fell as rain (Lundquist et al., 2008).

After 6 am another 0.1 inches of rain fell. Temperatures would have warmed and the precipitation may have turned to rain. Rain would pass through the porous fresh snow before emerging as runoff (Singh et al., 1997). Although results of rain-on-snow events is dependent on the state of the snow before the rain event, it could cause higher runoff levels than might be found by rainfall alone (Lundquist et al., 2008; Wever et al., 2014). This could account for the first peak of the storm. The second peak cannot be connected to any precipitation but occurs after 11 am during the warmest period of the day. Although still cold, a 5 °C temperature could induce some snowmelt which could be

particularly effective as runoff if the snowpack was conditioned by the rain to create preferential flow pathways (Singh et al., 1997).

### *Other Issues*

The March 26<sup>th</sup> and May 11<sup>th</sup> storms of site GE show instances of observed flow occurring with no similar reaction in predicted flow for either model. On March 26<sup>th</sup> the observed flow in question occurs during a prolonged period of no precipitation between 10 am and 2 pm when temperatures reached a high of 3.3 °C (Table 20). Despite the fairly low temperature, it could be enough to induce snowmelt if conditions were right (Lundquist et al., 2008). Modeling snowmelt increases complexity of the model drastically and therefore was not accounted for in this model. For comparative purposes, the March 26<sup>th</sup> storm outflow was readjusted to estimate flow, volume and peak events occurring due to precipitation (Figure C-21).

An isolated instance of ‘flash’ can be found at the end of the March 26<sup>th</sup> storm. At this point the observed flow drops from 0.219 cfs to zero in five minutes. A similar drop of this size does not occur elsewhere in the dataset. This is not likely a natural occurrence and thus is considered an error in the dataset.

On May 11<sup>th</sup>, the observed flow that is not represented in the models also happens during a period of no precipitation. This period is much shorter and falls earlier in the day between 5 and 7 am. There is a possibility that the observed flow is ahead of the precipitation and might be off by about 1hr. Even so, the period of interest falls between

6 and 8 am. Although the temperature reaches a maximum of 8.3 °C, it was likely still very cold at this early hour (Table 20). Still it is possible that the flow is snowmelt.

The site SY March 15<sup>th</sup> storm also has some missing data that led to a large discrepancy from modeled flow outputs occurring between 6:20 am and 12:40 pm. In addition the peak in flow occurs before the peak in precipitation leading to the belief that the observed flow might be offset by an hour. In this case, the portion of the storm with no observed data is discarded before it is evaluated for efficiency.

### **Sources of Error**

This model did well in some cases and managed to reasonably predict flow despite very small basin size and flow values. There were several sources of error in the model and the methods used that added to discrepancies between predicted and observed values. This includes snow, model method and parameter selection, and optimization processes.

Due to the complexity of modeling snowmelt, and the lack of detailed temperature and evapotranspiration data, snow was not included in modeled events. Most storms chosen were indicated as rain or thunderstorm events and would not be affected by snow. In some cases, lack of numerous adequate storm events meant some snow and snowmelt storm events were included. These events would show error in both models. However, as this study was a comparison between two models rather than an attempt to create a highly accurate model, relative error between models could still indicate improved value in the models.

Another source of error can be found in parameter estimation. All initial parameter estimates and final parameter values can be found in Appendix B. Models were optimized to a single storm and events were considered with no respect for the previous events. This means that initial infiltration values did not change between modeled storms. As a result early runoff values for events show some discrepancies as initial loss due to depression storage and antecedent soil moisture could be under- or overestimated.

The Snyder peaking coefficients were optimized at values well below those typically found in literature. This could be due to the unusually small size of the basins used. The HEC-HMS model uses hours as a unit and has a minimum possible value of 0.1 hours for the Snyder time to peak parameter. The small size of the basins and subbasins meant that the time to peak often should be measured in minutes instead of hours. On multiple occasions, the calculation used to estimate the parameter indicated a time to peak lower than the cutoff. During optimization these values had an initial estimate of 0.1 hours. In addition, optimization did not bring any time to peak values below that same cutoff. This could result in delayed peak values in modeled outputs for these subbasins that could delay the outlet peak or change the synchronicity of the basin. This was more typical of LiDAR watersheds since they contained more plentiful, smaller subbasins. Model outputs indicate that LiDAR models typically had more delay in peak relative to observed flow than the 10-meter models by 10 to 30 min.

Model optimization also introduced some potential error. The optimization method used for model calibrations was chosen because it performed better than other

methods within site SY, was easy to use and offered improved peak flow values which were deemed more important for this study. Since this study is aimed at comparing relative value outputs, a multi-goal oriented objective function calibration was regarded as too time consuming. Although a single objective function is usually inadequate, in this case a method based on a single desired data output was judged sufficient (Madsen et al., 2002; Yapo et al., 1998). Thus it is expected that low flow rates, overall volumes, and timing will have greater deviation from the observed since they are not the main focus of the objective function (Madsen, 2000). This type of error should occur in both LiDAR and 10-meter models in a similar manner and extent.

Global population-evolution based search procedures perform better than any local search procedure (Madsen, 2003). However, HEC-HMS only offers two local search procedures, univariate gradient and Nelder-Mead simplex (HEC, 2000). Instead the multi-start local procedure called the Nelder-Mead simplex was used as multi-start procedures perform better than pure local search procedure (Madsen, 2003). This method assumes that the function is continuous and has a unique minimum value (Nelder and Mead, 1965). Local search procedures performed on unimodal functions will reach a global minimum (Madsen, 2000). Although the storms used for optimization in this study are not unimodal, they are event based and not a continuous long-term precipitation record. They have a better chance of reaching the global minimum than such a long-term situation since there are fewer flow peaks.

## CONCLUSIONS

The purpose of this study was to compare the predictions of small urban hydrologic models with drainage areas and networks defined by LiDAR and 10-meter DEMs to see if higher resolution ground data can improve model simulation output. More detailed and accurate flow models would aid basin managers and city planners better contain, divert or utilize overland urban runoff and the pollutants contained within.

For this study LiDAR and NAIP imagery were used to create a high-resolution land cover classification and identify DCIA. Both LiDAR and 10-meter datasets were used to estimate watershed area and shape. Next, attributes from these basins were used in the HEC-HMS model to evaluate predicted runoff for each data resolution. Finally, the LiDAR and 10-meter simulation outputs were compared to each other.

Model simulations showed neither resolution had a marked improvement in flow predictions. Model output was mainly influenced by basin size and shape and drainage density. However, there were enough inherent errors in the model setup and process to confuse the results. Despite the models inability to clearly benefit from higher resolution inputs, the high-resolution data did produce a much more detailed and descriptive flow delineations that can prove useful to basin managers or city planners.

A supervised classification was successfully produced using NAIP imagery, an NDVI image and object height information obtained from the LiDAR dataset. The classification was further improved using expert knowledge in the form of identified thresholds and additional datasets such as a road map and slope image. Impervious area

was successfully estimated with an overall accuracy of 93.5%. The percentage of DCIA in each basin was estimated for the two models from this image.

In general, the model produced reasonable predictions in runoff for both LiDAR and 10-meter DEMs. However, there was a substantial amount of potential error introduced through basin delineation, storm selection, parameter estimation, and optimization methods. This led to deviations in peak, volume and timings of modeled storms. As a result, it was difficult to effectively compare the modeled outputs to each other and understand how the two initial data resolutions affected the model output.

Overall, the model resolution did not appear to make much difference in runoff using HEC-HMS. However, it is difficult to tell without better model performance. Neither LiDAR nor 10-meter models improved predictions consistently. Various factors affecting the models made it difficult to ascertain if either resolution improved results.

The most important aspect affecting the runoff volumes appears to be the size and shape of the input basin and drainages. This varied dramatically between LiDAR and 10-meter DEMs. 10-meter basins were larger with fewer drainages and lower drainage to area ratios. Site SY had the most similarity in size, although the 10-meter basin larger while the LiDAR basin had almost double drainage length to basin area ratios. Both resolutions produced fairly similar results with the 10-meter model predicting higher peaks and volumes than the LiDAR models just over half the time. At site O3 the LiDAR models predicted higher peaks and volumes across the board. Despite the smaller basin size, the LiDAR model had a higher percent DCIA, a greater number of subbasins and more drainage lines causing the increased flow values. Site GE displayed opposite results

with the 10-meter basin showing much higher peak flow and volume outputs. This site had the most drastic difference in basin size. In addition to being larger, the 10-meter basin had a slight increase in percent DCIA. Both these attributes would lead to higher runoff in the 10-meter model.

Individual storm events displayed three common differences with observed values. Many observed hydrographs had steeper rising and falling limbs and a higher peak flow than predicted hydrographs. This most commonly occurred in summer thunderstorms. Underestimation of DCIA and type of optimization storm could be why predictions did not better follow observations in these storms. Winter storms did not experience this issue. Instead, snow in an event showed three possible effects on the hydrograph. It either increased or reduced the volume compared to the models or it created flow with no precipitation. This depended on the state of the snowpack and precipitation and temperature during the storm event. Lastly, some model hydrographs show flow related to precipitation but with no observed flow occurring. This occurs at the beginning of four storms likely because of poor accounting for antecedent conditions and depression storage. In one storm, it happens at the end and the most likely scenario is a sudden increase in depression storage or a diversion of water away from the drainage during the storm. This could be something as simple as a garbage bag dropped in the gutter or a fallen tree branch that causes the water to pond up and be diverted onto open ground where it infiltrates rather than reach the outlet.

Model methods selected may not be adequate to differentiate between the two resolution inputs. A single local, direct, multistart search method and objective function

were used in the optimization of the models. This means there is a possibility that the global minimum of the function was not always reached. It was deemed more important that optimization methods remained consistent between models than that an ideal optimization was reached. Additionally, optimized parameter estimates for the Snyder's lag time often reached the minimum value allowed in the HEC-HMS model. This occurred more in LiDAR models due to the smaller subbasin sizes and could result in an overestimation of time to peak for some of the subbasins. Enough error was introduced into the model that it is difficult to say that using a finer LiDAR resolution would affect the model predictions significantly. The resolution affected the model mostly by altering the basin and flowline delineation. These differed dramatically between the two resolutions. LiDAR produced longer flow paths, smaller subbasins and more of them. Additionally, LiDAR resulted in smaller total basin sizes. Basin size, drainage density and sinuosity can affect the amount and timing of runoff that reaches the outlet.

LiDAR DEMs produced more detailed drainage delineation maps and resulted in smaller basin sizes with more subbasins. The high resolution LiDAR resulted in flow patterns that were much more detailed and precise when drainage collection area is equal. The improved details in flow patterns allow us to see water pathways across an urban landscape. Drainages follow roads, around buildings and furnish further detail on how water travels over the landscape. While the HEC-HMS model was unable to capture this added information, it may prove useful to city planners or basin managers and aid in the location of runoff detention or infiltration structures

## LITERATURE CITED

- Alley, W.M., Veenhuis, J.E., 1983. Effective Impervious Area in Urban Runoff Modeling. *J. Hydraul. Eng.* 109, 313–320.
- Allouis, T., Bailly, J.S., Pastol, Y., Roux, C.L., 2010. Comparison of LiDAR waveform processing methods for very shallow water bathymetry using Raman, near-infrared and green signals. *Earth Surf. Process. Landforms* 35, 640–650.
- Andersen, H., McGaughey, R.J., Reutebuch, S.E., 2005. Estimating forest canopy fuel parameters using LIDAR data. *Remote Sensing of Environment* 94, 441–449.
- Andersen, H., Reutebuch, S.E., McGaughey, R.J., 2006. Active remote sensing, in: *Computer Applications in Sustainable Forest Management: Including Perspectives on Collaboration and Integration*. pp. 43–66.
- American Society of Civil Engineers (ASCE), 1996. Infiltration, in: *Hydrology Handbook, Manual and Reports on Engineering Practice*. American Society of Civil Engineers, New York, pp. 91, 97.
- Barati, R., 2011. Parameter estimation of nonlinear Muskingum models using Nelder-Mead simplex algorithm. *J. Hydrol. Eng.* 16, 946–954.
- Berris, S.N., Harr, R.D., 1987. Comparative snow accumulation and melt during rainfall in forested and clear-cut plots in the western Cascades of Oregon. *Water Resources Research* 23, 135–142.
- Coats, R., Larsen, M., Heyvaert, A., Thomas, J., Luck, M., Reuter, J., 2008. Nutrient and Sediment Production, Watershed Characteristics, and Land Use in the Tahoe Basin, California-Nevada. *J Am Water Resources Assoc* 44, 754–770.
- Cochrane, T.A., Gnanagan, D.C., 1999. Assessing water erosion in small watersheds using WEPP with GIS and digital elevation models. *Journal of Soil and Water Conservation* 54, 678–685.
- Connell, J.H., 1978. Diversity in Tropical Rain Forests and Coral Reefs. *Science, New Series* 199, 1302–1310.
- Corbett, C.W., Wahl, M., Porter, D.E., Edwards, D., Moise, C., 1997. Nonpoint source runoff modeling: A comparisons of a forested watershed and an urban watershed on the South Carolina coast. *Journal of Experimental Marine Biology and Ecology* 213, 133–149. Heyvaert Heyvaert
- Cronshey, R., United States. Soil Conservation Service. Engineering Division, 1986. Urban hydrology for small watersheds, Technical release. U.S. Dept. of Agriculture, Soil Conservation Service, Engineering Division.
- Cunderlik, J.M., Simonovic, S.P., 2007. Hydrologic models for inverse climate impact modeling, in: *Challenges for Water Resources Engineering in a Changing World*. Presented at the 18th Canadian Hydrotechnical Conference, Winnipeg, Manitoba, Canada.

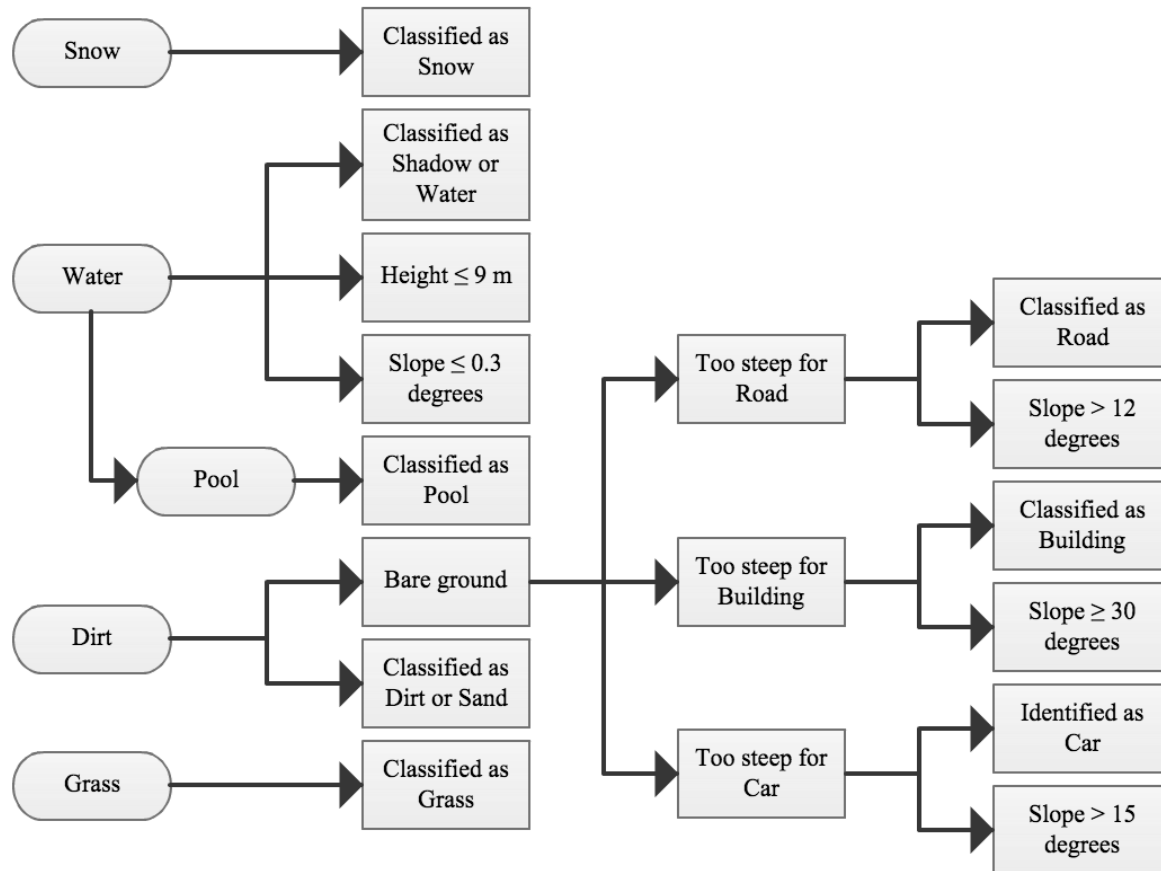
- Davies, J.R., Lagueux, K.M., Sanderson, B., Beechie, T.J., 2007. Modeling Stream Channel Characteristics From Drainage-Enforced DEMs in Puget Sound, Washington, USA. *J Am Water Resources Assoc* 43, 414–426.
- Diskin, M.H., Simon, E., 1977. Procedure for the selection of objective functions for hydrologic simulation models. *Journal of Hydrology* 34, 129–149.
- Environmental Protection Agency (EPA), 2008. Impervious Surfaces and the Hydrologic Balance of Watersheds [WWW Document]. United States Environmental Protection Agency. URL <http://water.epa.gov/learn/training/wacademy/07set.cfm> (accessed 12/08/11).
- Environmental Protection Agency (EPA), 2011. Invertebrates as Indicators [WWW Document]. Biological Indicators of Watershed Health. URL <http://www.epa.gov/bioiweb1/html/invertebrate.html> (accessed 12/13/11).
- Environmental Protection Agency (EPA), 2012. Flow alteration in urban streams [WWW Document]. EPA. URL [http://www.epa.gov/caddis/ssr\\_urb\\_hyd1.html](http://www.epa.gov/caddis/ssr_urb_hyd1.html)
- Forney, W., Richards, L., Adams, K.D., Mino, T.B., Rowe, T.G., Smith, J.L., Raumann, C.G., 2001. Land Use Change and Effects on Water Quality and Ecosystem Health in the Lake Tahoe Basin, Nevada and California (Open-File Report No. 01-418). United States Geological Survey, Tahoe Basin.
- French, J.R., 2003. Airborne LiDAR in support of geomorphological and hydraulic modeling. *Earth Surf. Process. Landforms* 28, 321–335.
- Greenhill, D.R., Ripke, L.T., Hitchman, A.P., Jones, G.A., Wilkinson, G.G., 2003. Characterization of Suburban Areas for Land Use Planning Using Landscape Ecological Indicators Derived from Ikonos-2 Multispectral Imagery. *IEEE Transactions on Geoscience and Remote Sensing* 41, 2015–2021.
- Halwatura, D., Najim, M.M.M., 2013. Application of the HEC-HMS model for runoff simulation in a tropical catchment. *Environmental Modelling & Software* 46, 155–162.
- Hydrologic Engineering Center (HEC), 2000. Hydrologic Modeling System HEC-HMS: Technical reference manual (Computer Software Technical Reference Manual). U.S. Army Corps of Engineers, Davis, CA.
- Hydrologic Engineering Center (HEC), 2010. Hydrologic Modeling System HEC-HMS: User's manual - Version 3.5 (Computer Software User's Manual No. Version 3.5). U.S. Army Corps of Engineers, Davis, CA.
- James, L.A., Watson, D.G., Hansen, W.F., 2007. Using LiDAR data to map gullies and headwater streams under forest canopy: South Carolina, USA. *CATENA* 71, 132–144.
- Jones, A.F., Brewer, P.A., Johnstone, E., Macklin, M.G., 2007. High-resolution interpretative geomorphological mapping of river valley environments using airborne LiDAR data. *Earth Surf. Process. Landforms* 32, 1574–1592.
- Kennedy/Jenks Consultants, 2010. Stormwater system, South Lake Tahoe, CA.
- Klein, R.D., 1979. Urbanization and Stream Quality Impairment. *Water Resources Bulletin* 15, 949–963.

- Konrad, C.P., Booth, D.B., 2005. Hydraulic Changes in Urban Streams and Their Ecological Significance. *American Fisheries Society Symposium* 47, 157–177.
- Krause, P., Boyle, D.P., Base, F., 2005. Comparison of different efficiency criteria for hydrological model assessment. *Advances in Geosciences* 5, 89–97.
- Kumar, D., Bhattacharjya, R.K., 2011. Distributed rainfall runoff modeling. *International Journal of Earth Sciences and Engineering* 4, 270–275.
- Lagarias, J.C., Reeds, J.A., Wright, M.H., Wright, P.E., 1998. Convergence Properties of the Nelder--Mead Simplex Method in Low Dimensions. *SIAM Journal on Optimization* 9, 112–36.
- Lee, J.G., Heaney, J.P., 2003. Estimation of Urban Imperviousness and its Impacts on Storm Water Systems. *Journal of Water Resources Planning and Management* 129, 419–426.
- Li, J., Wong, D.W.S., 2010. Effects of DEM sources on hydrologic applications. *Computers, Environment and Urban Systems* 34, 251–261.
- Lu, D., Weng, Q., 2005. Urban Classification Using Full Spectral Information of Landsat ETM+ Imagery in Marion County, Indiana. *Photogrammetric Engineering & Remote Sensing* 71, 1275–1284.
- Lundquist, J.D., Neiman, P.J., Martner, B., White, A.B., Gottas, D.J., Ralph, F.M., 2008. Rain versus snow in the Sierra Nevada, California: Comparing doppler profiling radar and surface observations of melting level. *Journal of Hydrometeorology* 9, 194–211.
- Madsen, H., 2003. Parameter estimation in distributed hydrological catchment modelling using automatic calibration with multiple objectives. *Advances in Water Resources* 26, 205–216.
- Madsen, H., 2000. Automatic calibration of a conceptual rainfall–runoff model using multiple objectives. *Journal of hydrology* 235, 276–288.
- Madsen, H., Wilson, G., Ammentorp, H.C., 2002. Comparison of different automated strategies for calibration of rainfall-runoff models. *Journal of Hydrology* 261, 48–59.
- Marks, D., Kimball, J., Tingey, D., Link, T., 1998. The sensitivity of snowmelt processes to climate conditions and forest cover during rain-on-snow: a case study of the 1996 Pacific Northwest flood. *Hydrol. Process.* 12, 1569–1587.
- Naiman, R.J., Bilby, R.E. (Eds.), 1998. *River Ecology and Management Lessons from the Pacific Coastal Ecoregion*. Springer, New York.
- National Agriculture Imagery Program (NAIP), 2011. National Agriculture Imagery Database, 2010 [WWW Document]. Cal-Atlas Geospatial Clearinghouse. URL <http://www.atlas.ca.gov/download.html> (accessed 07/11/11).
- National Climatic Data Center (NCDC), 2010. Record of climatological observations: South Lake Tahoe Airport station (1968-2010) [WWW Document]. Monthly summaries of the global historical climatology network - Daily (GHCN-d). URL <https://gis.ncdc.noaa.gov/geoportal/catalog/main/home.page> (accessed 07/02/15).
- Nelder, J.A., Mead, R., 1965. A simplex method for function minimization. *The Comp. J.* 7, 308–313.

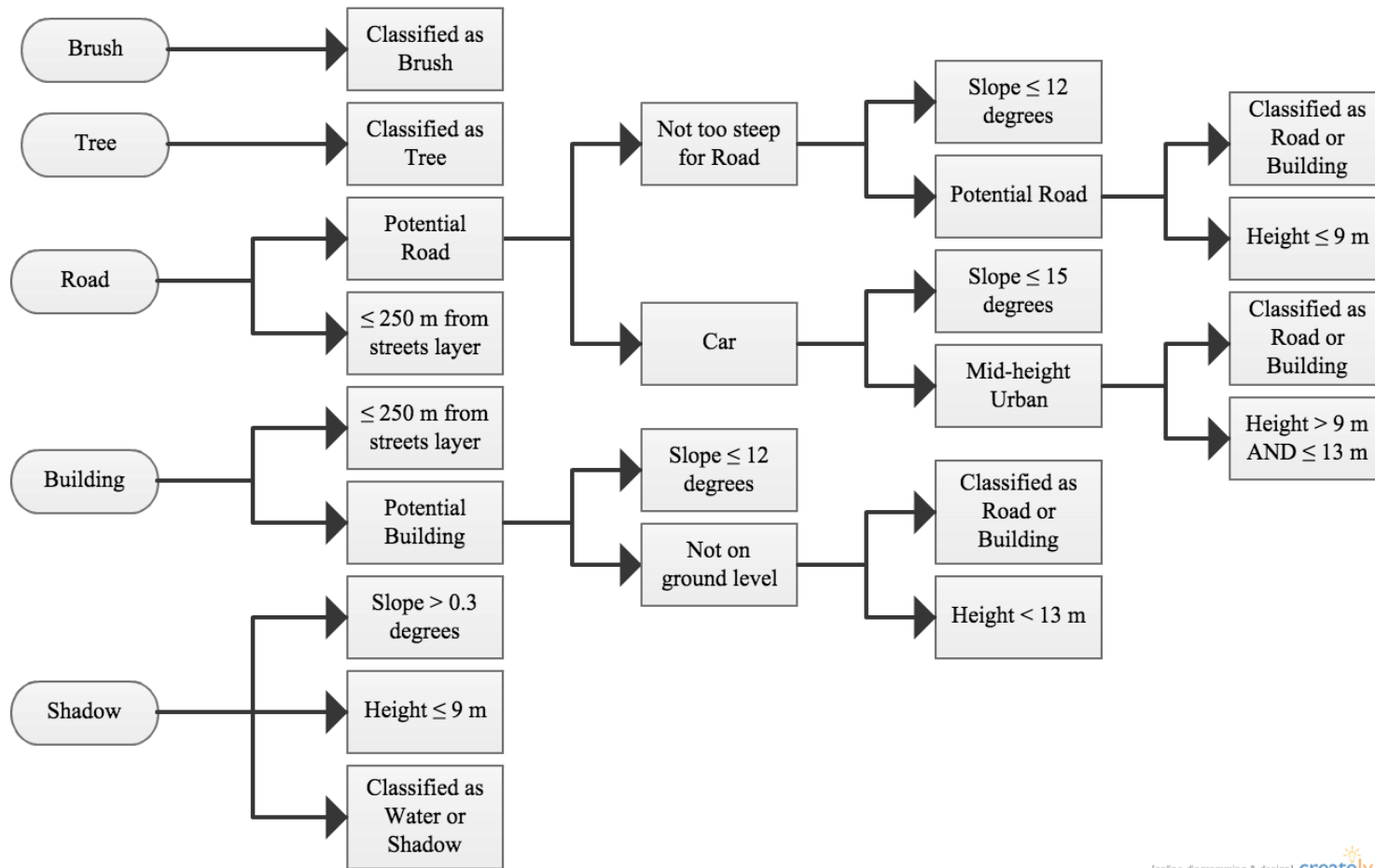
- Paul, M.J., Meyer, J.L., 2001. Streams in the Urban Landscape. *Annu. Rev. Ecol. Syst.* 32, 333–365.
- Pistocchi, A., Mazzoli, P., 2002. Use of HEC-RAS and HEC-HMS models with ArcView for hydrologic risk management. Presented at the Proc. Conference IEMSS, pp. 24–27.
- Power, M.E., Stout, R.J., Cushing, C.E., Harper, P.P., Hauer, F.R., Matthews, W.J., Moyle, P.B., Statzner, B., Wais de Badgen, I.R., 1988. Biotic and abiotic controls in river and stream communities. *Journal of the North American Benthological Society* 7, 456–479.
- Resh, V.H., Brown, A.V., Covich, A.P., Gurtz, M.E., Li, H.W., Minshall, G.W., Reice, S.R., Sheldon, A.L., Wallace, J.B., Wissmar, R.C., 1988. The role of disturbance in stream ecology. *Journal of the North American Benthological Society* 7, 433–455.
- Reutebuch, S.E., Andersen, H., McGaughey, R.J., 2005. Light Detection and Ranging (LIDAR): An Emerging Tool for Multiple Resource Inventory. *Journal of Forestry* 103, 286–292.
- Roy, A.H., Shuster, W.D., 2009. Assessing impervious surface connectivity and applications for watershed management. *JAWRA* 45, 198–209.
- Saleh, A., Ghobad, R., Noredin, R., 2011. Evaluation of the HEC-HMS methods in surface runoff simulations - Case study: Kan Watershed, Iran. *Adv. Environ. Biol.* 5, 1316–1321.
- Singh, P., Spitzbart, G., Hübl, H., Weinmeister, H., 1997. Hydrological response of snowpack under rain-on-snow events: a field study. *Journal of Hydrology* 202, 1–20.
- Skaggs, R.W., Khaleel, R., 1982. Infiltration, in: *Hydrologic Modeling of Small Watersheds*. American Society of Agricultural Engineers, St. Joseph, MI.
- Smith, A.Y., Blackwell, R.J., 1980. Development of an information data base for watershed monitoring. *Photogrammetric Engineering & Remote Sensing* 46, 1027–1038.
- Snyder, F.F., 1938. Synthetic unit- graphs. *Eos, Transactions American Geophysical Union* 19, 447–454.
- Tarboton, D.G., Ames, D.P., 2001. Advances in the mapping of flow networks from digital elevation data.
- Tahoe Environmental Research Center (TERC), 2011. Tahoe: state of the lake report 2011 (Annual). University of California, Davis.
- Tahoe Environmental Research Center (TERC), 2014. Tahoe: State of the lake report 2014 (Annual). University of California, Davis.
- Tahoe Regional Planning Agency (TRPA), 1997. Stream and ground-water monitoring program, Lake Tahoe Basin, Nevada and California [WWW Document]. Lake Tahoe Data Clearinghouse. URL <http://pubs.usgs.gov/fs/FS-100-97/> (accessed 12/12/11).
- United States Army Corps of Engineers (USACE), 1956. Snow Hydrology. U.S. Army Corps of Engineers, Portland, Oregon.

- United State Geological Survey (USGS), 2008. Facts about Lake Tahoe. [WWW Document]. Lake Tahoe Data Clearinghouse. URL <http://tahoe.usgs.gov/facts.html> (accessed 12/12/11).
- Wagener, T., Sivapalan, M., Troch, P.A., McGlynn, B.L., Harman, C.J., Gupta, H.V., Kuman, P., Rao, P.S.C., Basu, N.B., Wilson, J.S., 2010. The future of hydrology: An evolving science for a changing world. *Water Resources Research* 46.
- Wever, N., Jonas, T., Fierz, C., Lehning, M., 2014. Model simulations of the modulating effect of the snow cover in a rain-on-snow event. *Hydrology and Earth System Sciences* 18, 4657–4669. doi:10.5190/hess-18-4657-2014
- Watershed Sciences Incorporated (WSI), 2011. LiDAR remote sensing - Lake Tahoe watershed - California/Nevada. Corvallis, OR.
- Yang, X., Liu, Z., 2005. Use of satellite-derived landscape imperviousness index to characterize urban spatial growth. *Computers, Environment and Urban Systems* 29, 524–540.
- Yapo, P.O., Gupta, H.V., Sorooshian, S., 1998. Multi-objective global optimization for hydrologic models. *Journal of hydrology* 204, 83–97.
- Yusop, Z., Chan, C.H., Katimon, A., 2007. Runoff characteristics and application of HEC-HMS for modelling stormflow hydrograph in an oil palm catchment. *Water Science & Technology* 56, 41–48.

## APPENDIX A



Appendix A: Diagram and threshold rules applied with the Knowledge Engineer to improve supervised classification.



Appendix A: Diagram and threshold rules applied with the Knowledge Engineer to improve supervised classification (continued).

## APPENDIX B

Appendix B: Initial and optimized parameters for HEC-HMS model methods.

Table B-1: Initial and optimized parameter values for the initial and constant loss method.

<b>Model</b>	<b>Subbasin</b>	<b>DCIA (%)</b>	<b>Initial Loss (in)</b>	<b>Optimized Initial Loss (in)</b>	<b>Objective Function Sensitivity</b>	<b>Constant Loss Rate (in/hr)</b>	<b>Optimized Loss Rate (in/hr)</b>	<b>Objective Function Sensitivity</b>
SY 10 m	W80	77.95	0.2	0.20	0	0.336	0.439	0
	W130	27.21	0.2	0.41	0	0.320	0.563	0
	W280	20.91	0.2	0.26	0	0.263	0.336	0
	W340	48.76	0.2	0.18	0.01	0.339	0.001	0
	W350	54.88	0.2	0.18	0	0.367	0.542	0
	W400	25.95	0.2	0.28	0	0.239	0.338	0
	W500	32.95	0.2	0.40	0	0.254	0.332	0
SY LiDAR	W01	63.04	0.2	0.41	0	0.368	0.553	0
	W02	87.45	0.2	0.41	0	0.375	0.562	0
	W03	71.97	0.2	0.41	0	0.345	0.532	0
	W04	88.26	0.2	0.41	0	0.369	0.554	0
	W05	42.93	0.2	0.41	0	0.373	0.557	0
	W06	19.80	0.2	0.42	0	0.375	0.558	0
	W07	59.13	0.2	0.42	0	0.340	0.583	0

Table B-1: Initial and optimized parameter values for the initial and constant loss method (continued).

<b>Model</b>	<b>Subbasin</b>	<b>DCIA (%)</b>	<b>Initial Loss (in)</b>	<b>Optimized Initial Loss (in)</b>	<b>Objective Function Sensitivity</b>	<b>Constant Loss Rate (in/hr)</b>	<b>Optimized Loss Rate (in/hr)</b>	<b>Objective Function Sensitivity</b>	
SY LiDAR	W08	68.73	0.2	0.42	0	0.375	0.558	0	
	W09	54.69	0.2	0.42	0	0.341	0.571	0	
	W10	73.91	0.2	0.42	0	0.375	0.557	0	
	W11	28.07	0.2	0.43	0	0.371	0.557	0	
	W120	55.58	0.2	0.41	0	0.269	0.470	0	
	W121	32.77	0.2	0.41	0	0.231	0.444	0	
	W122	42.32	0.2	0.41	0	0.236	0.470	0	
	W123	58.63	0.2	0.41	0	0.375	0.550	0	
	W124	55.12	0.2	0.41	0	0.294	0.515	0	
	W13	29.21	0.2	0.41	0	0.225	0.386	0	
	W14	22.36	0.2	0.41	0	0.225	0.381	0	
	Wbbsy	33.30	0.2	0.41	0	0.375	0.618	0	
	O3 10 m	W400	23.36	0.2	0.27	0	0.130	3.196	0
		W450	16.17	0.2	0.85	0	0.094	0.078	0
O3 LiDAR	W2000	33.49	0.2	0.06	0	0.189	0.141	0	
	W2020	24.58	0.2	0.11	0	0.189	0.156	0	
	W2040	20.11	0.2	0.30	0	0.189	0.122	0	
	W2060	35.93	0.2	0.05	0	0.063	0.154	0	

Table B-1: Initial and optimized parameter values for the initial and constant loss method (continued).

<b>Model</b>	<b>Subbasin</b>	<b>DCIA (%)</b>	<b>Initial Loss (in)</b>	<b>Optimized Initial Loss (in)</b>	<b>Objective Function Sensitivity</b>	<b>Constant Loss Rate (in/hr)</b>	<b>Optimized Loss Rate (in/hr)</b>	<b>Objective Function Sensitivity</b>
O3 LiDAR	W2070	27.74	0.2	0.00	0	0.179	0.138	0
	W2080	32.36	0.2	0.04	0	0.080	0.161	0
	W2090	22.90	0.2	0.04	0	0.112	0.135	0
	W2140	27.93	0.2	0.12	0	0.036	0.197	0
GE 10 m	W70	14.82	0.2	0.01	0	0.375	0.206	0
	W120	47.86	0.2	0.25	0	0.375	0.133	-0.02
	W130	9.04	0.2	0.20	0	0.375	0.247	0
	W170	10.44	0.2	0.00	0	0.375	0.367	0
	W180	15.86	0.2	0.20	0	0.375	0.211	0
GE LiDAR	W80	39.75	0.2	0.15	0	0.375	0.361	0
	W90	21.28	0.2	0.15	0	0.375	0.353	0
	W100	22.62	0.2	0.01	0	0.375	0.435	0
	W120	14.02	0.2	0.24	0	0.375	0.344	0
	W130	7.92	0.2	0.30	0	0.375	0.335	0
	W140	8.95	0.2	0.32	0	0.375	0.272	0
	W210	9.58	0.2	0.13	0	0.375	0.243	0
	W230	17.30	0.2	0.11	0	0.375	0.266	0
W250	12.14	0.2	0.13	0	0.375	0.306	0	

Table B-2: Initial and optimized parameter values for Snyder's Unit Hydrograph method.

<b>Model</b>	<b>Subbasin</b>	<b>Snyder's Time to Peak (hr)</b>	<b>Optimized Time to Peak (hr)</b>	<b>Objective Function Sensitivity</b>	<b>Snyder's Peaking Coefficient</b>	<b>Optimized Peaking Coefficient</b>	<b>Objective Function Sensitivity</b>
SY 10 m	W80	0.14	0.28	0	0.1	0.16	0.02
	W130	0.16	0.25	0	0.1	0.23	0
	W280	0.16	0.23	0	0.1	0.22	0
	W340	0.19	0.33	-0.02	0.1	0.17	-0.02
	W350	0.13	0.18	0	0.1	0.18	0
	W400	0.19	0.30	-0.02	0.1	0.24	-0.01
	W500	0.23	0.31	-0.02	0.1	0.26	0
SY LiDAR	W01	0.16	0.61	-0.04	0.1	0.29	-0.01
	W02	0.12	0.53	-0.01	0.1	0.29	0
	W03	0.10	0.41	-0.02	0.1	0.29	0.01
	W04	0.14	0.55	-0.01	0.1	0.29	-0.02
	W05	0.18	0.47	-0.03	0.1	0.30	0
	W06	0.14	0.39	0	0.1	0.31	0
	W07	0.10	0.36	-0.01	0.1	0.30	0
	W08	0.09	0.35	0	0.1	0.30	0
	W09	0.13	0.33	0	0.1	0.32	0
	W10	0.04	0.33	0	0.1	0.33	0
	W11	0.11	0.32	0	0.1	0.37	0

Table B-2: Initial and optimized parameter values for Snyder's Unit Hydrograph method (continued).

<b>Model</b>	<b>Subbasin</b>	<b>Snyder's Time to Peak (hr)</b>	<b>Optimized Time to Peak (hr)</b>	<b>Objective Function Sensitivity</b>	<b>Snyder's Peaking Coefficient</b>	<b>Optimized Peaking Coefficient</b>	<b>Objective Function Sensitivity</b>
SY LiDAR	W120	0.07	0.32	0	0.1	0.54	0
	W121	0.13	0.34	0.01	0.1	0.40	-0.01
	W122	0.08	0.32	0	0.1	0.37	0
	W123	0.06	0.32	0	0.1	0.36	0
	W124	0.06	0.32	0	0.1	0.37	0
	W13	0.13	0.33	0.02	0.1	0.44	-0.01
	W14	0.12	0.32	0.04	0.1	0.49	-0.01
	Wbbsy	0.08	0.32	0	0.1	0.37	0
O3 10 m	W400	0.30	5.36	-0.17	0.1	0.10	0.19
	W450	0.30	0.43	-0.05	0.1	0.18	0.02
O3 LiDAR	W2000	0.16	0.19	0	0.1	0.11	0.07
	W2020	0.14	0.16	0	0.1	0.10	0.06
	W2040	0.13	0.15	0	0.1	0.21	0.03
	W2060	0.13	0.15	0	0.1	0.11	0.08
	W2070	0.15	0.18	0	0.1	0.10	0.07
	W2080	0.19	0.57	-0.12	0.1	0.11	0.11
	W2090	0.24	0.76	-0.1	0.1	0.10	0.12
W2140	0.23	0.53	-0.16	0.1	0.10	0.13	

Table B-2: Initial and optimized parameter values for Snyder's Unit Hydrograph method (continued).

<b>Model</b>	<b>Subbasin</b>	<b>Snyder's Time to Peak (hr)</b>	<b>Optimized Time to Peak (hr)</b>	<b>Objective Function Sensitivity</b>	<b>Snyder's Peaking Coefficient</b>	<b>Optimized Peaking Coefficient</b>	<b>Objective Function Sensitivity</b>
GE 10 m	W70	0.14	0.38	-0.03	0.1	0.10	0.03
	W120	0.23	2.54	-0.39	0.1	0.10	0.28
	W130	0.25	0.49	-0.11	0.1	0.12	0.04
	W170	0.15	0.27	-0.04	0.1	0.18	0.07
	W180	0.20	0.28	-0.15	0.1	0.14	0.1
GE LiDAR	W80	0.09	0.11	0	0.1	0.62	-0.02
	W90	0.14	0.12	0	0.1	0.11	-0.03
	W100	0.18	0.11	0	0.1	0.12	-0.06
	W120	0.12	0.33	0	0.1	0.14	0
	W130	0.22	0.56	-0.08	0.1	0.10	0.07
	W140	0.12	0.13	0	0.1	0.23	-0.04
	W210	0.15	0.75	-0.03	0.1	0.10	0.05
	W230	0.08	0.29	0	0.1	0.13	0
	W250	0.08	0.20	0	0.1	0.11	0

Table B-3: Initial and optimized parameter values for the lag routing method.

<b>Model</b>	<b>Reach</b>	<b>Reach Lag Time (min)</b>	<b>Optimized Lag Time (min)</b>	<b>Objective Function Sensitivity</b>
SY 10 m	R10	7.5	7.56	0
	R110	5	5.08	0
	R30	5	5.16	0
	R360	7.5	7.34	0
	R450	7.5	7.62	0
SY LiDAR	R10	3.5	3.59	0
	R100	7.5	7.72	0
	R110	7.5	7.71	0
	R111	7.5	7.70	0
	R120	7.5	7.68	0
	R130	7.5	7.68	0
	R140	7.5	7.74	0
	R20	3.5	3.67	0
	R21	3.5	3.66	0
	R22	3.5	3.66	0
	R30	3.5	3.66	0
	R40	3.5	3.65	0
	R50	3.5	3.65	0
	R60	3.5	3.52	0
	R70	7.5	7.67	0
	R80	7.5	7.67	0
	R90	7.5	7.67	0
Rbbsy	7.5	7.67	0	
O3 10 m	R330	5	0.00	0
O3 LiDAR	R10	5	4.90	0
	R30	5	5.07	0
	R50	5	5.34	0
	R70	5	4.87	0

Table B-3: Initial and optimized parameter values for the lag routing method (continued).

<b>Model</b>	<b>Reach</b>	<b>Reach Lag Time (min)</b>	<b>Optimized Lag Time (min)</b>	<b>Objective Function Sensitivity</b>
	R80	5	4.93	0
GE 10 m	R10	5.0	5.87	0
	R20	3.5	2.67	0
	R30	5.0	4.22	0
	R50	3.5	6.82	0
GE LiDAR	R10	7.5	7.50	0
	R220	7.5	7.63	0
	R30	7.5	7.48	0
	R40	7.5	7.40	0

APPENDIX C

Appendix C: Precipitation, observed and modeled hydrographs, peak flow rates and volume outputs for all storm events.

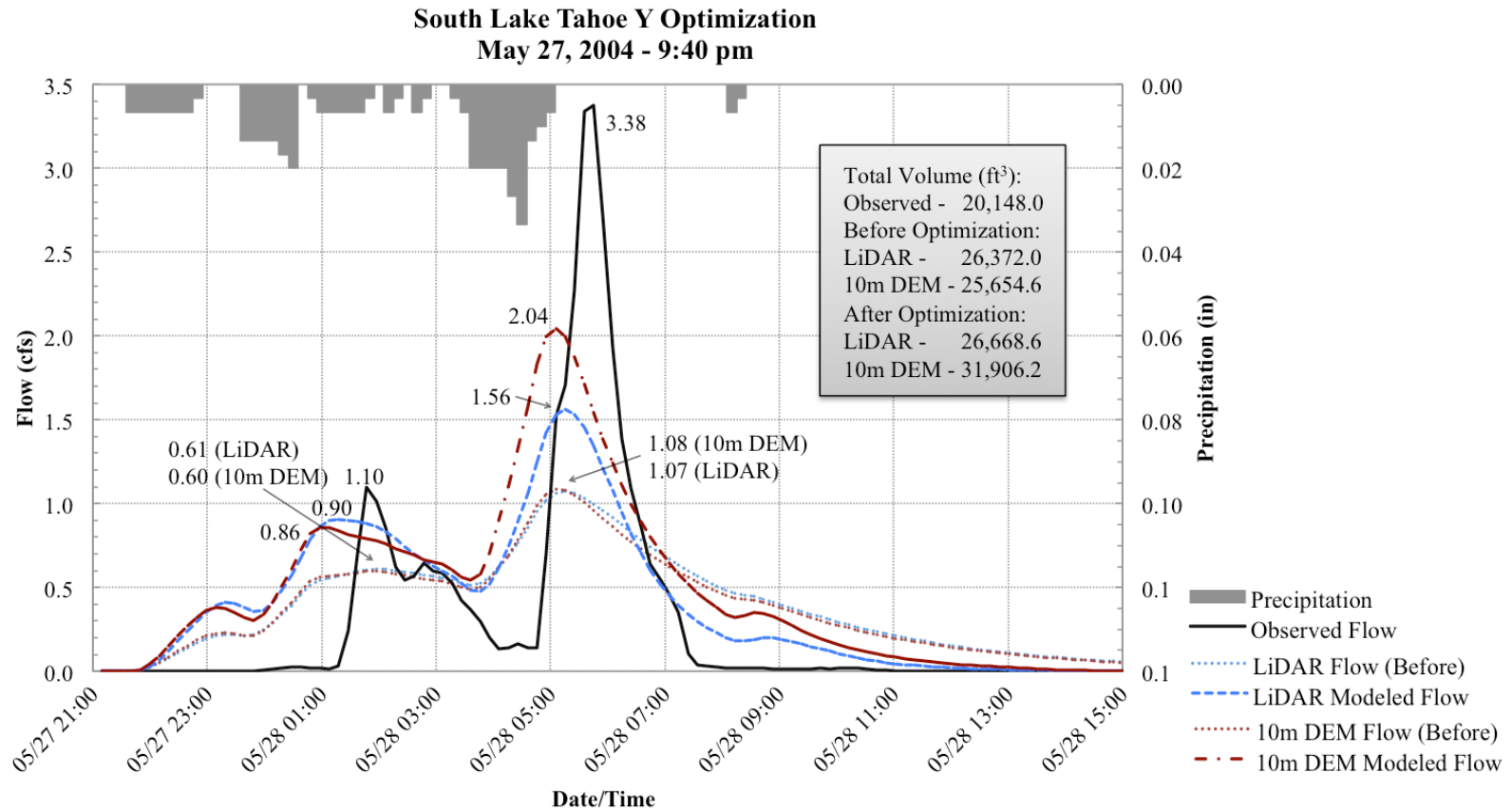


Figure C-1: Observed flow and HEC-HMS model output hydrographs (before and after optimization) for the South Lake Tahoe Y (SY) optimization storm beginning on May 27<sup>th</sup> at 9:40 pm (group A), located in South Lake Tahoe, CA.

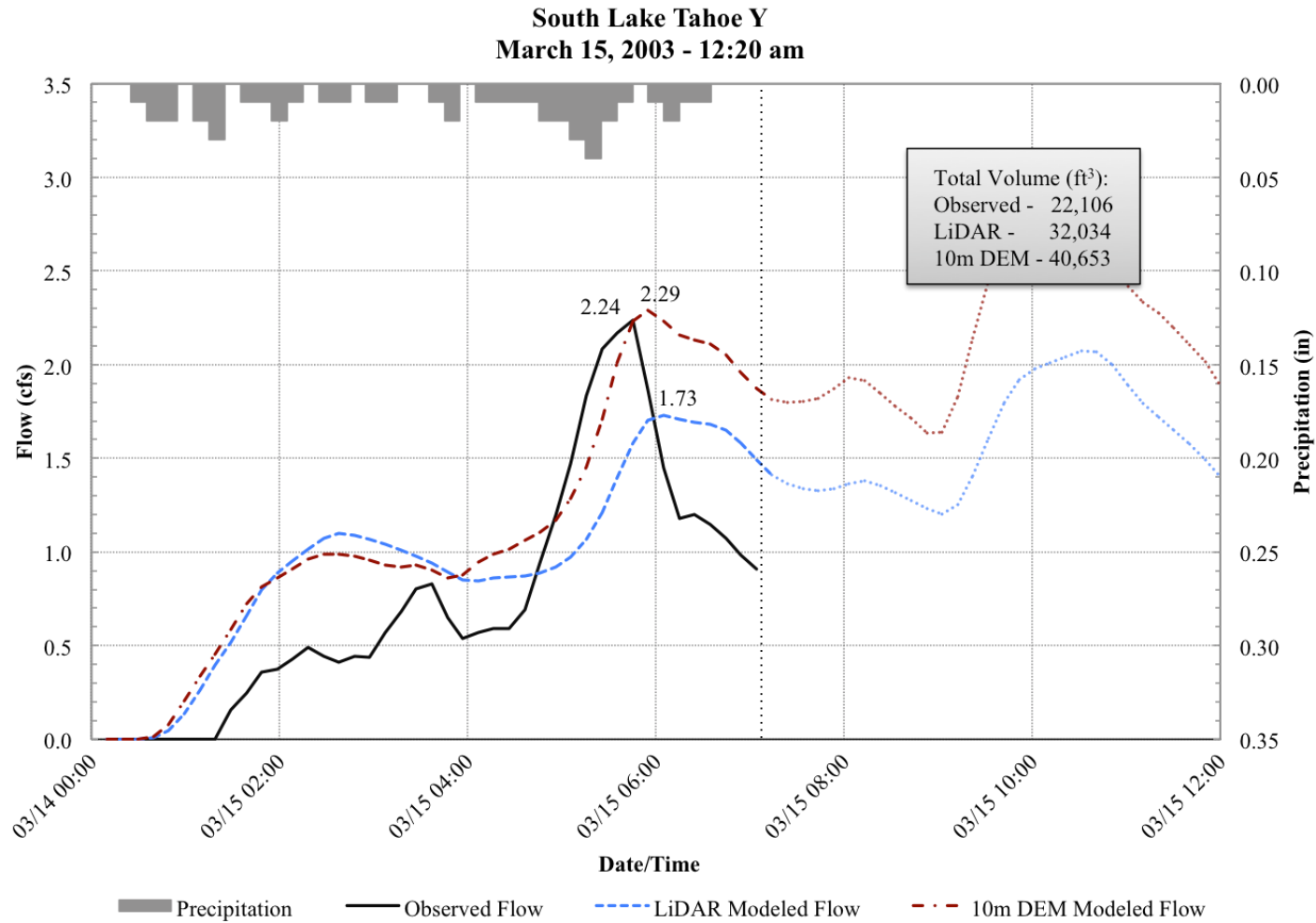


Figure C-2: Observed and HEC-HMS modeled hydrographs for the storm beginning on March 15<sup>th</sup> at 12:20 am (group A) at site SY, located in South Lake Tahoe. Only the period with available observed data was used for analysis (occurring before the dotted line). Observed hydrograph has been shifted forward one hour to account for dataset error.

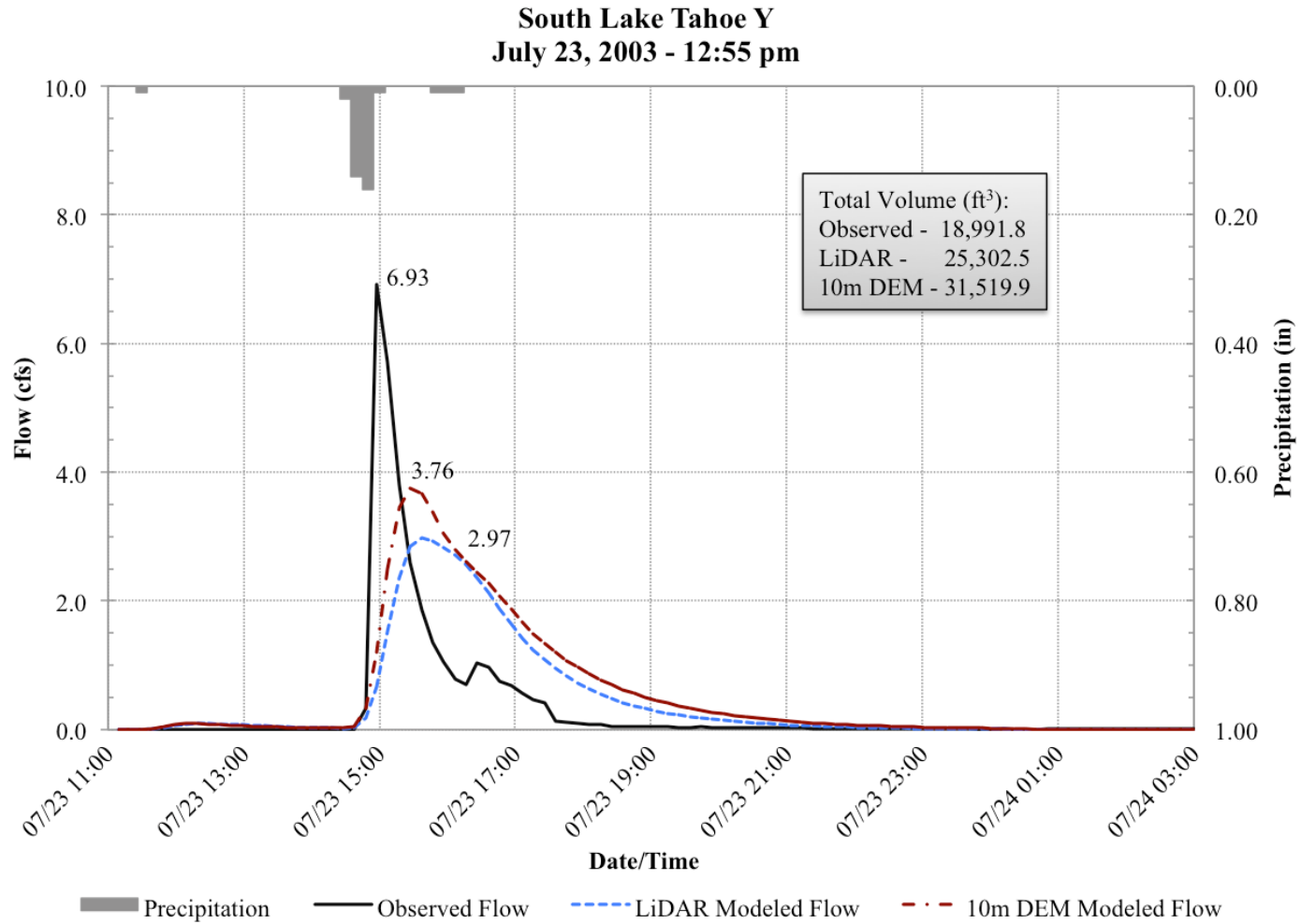


Figure C-3: Observed and HEC-HMS modeled hydrographs for storm event beginning on July 23<sup>rd</sup> at 12:55 pm (group A) at site SY, located in South Lake Tahoe.

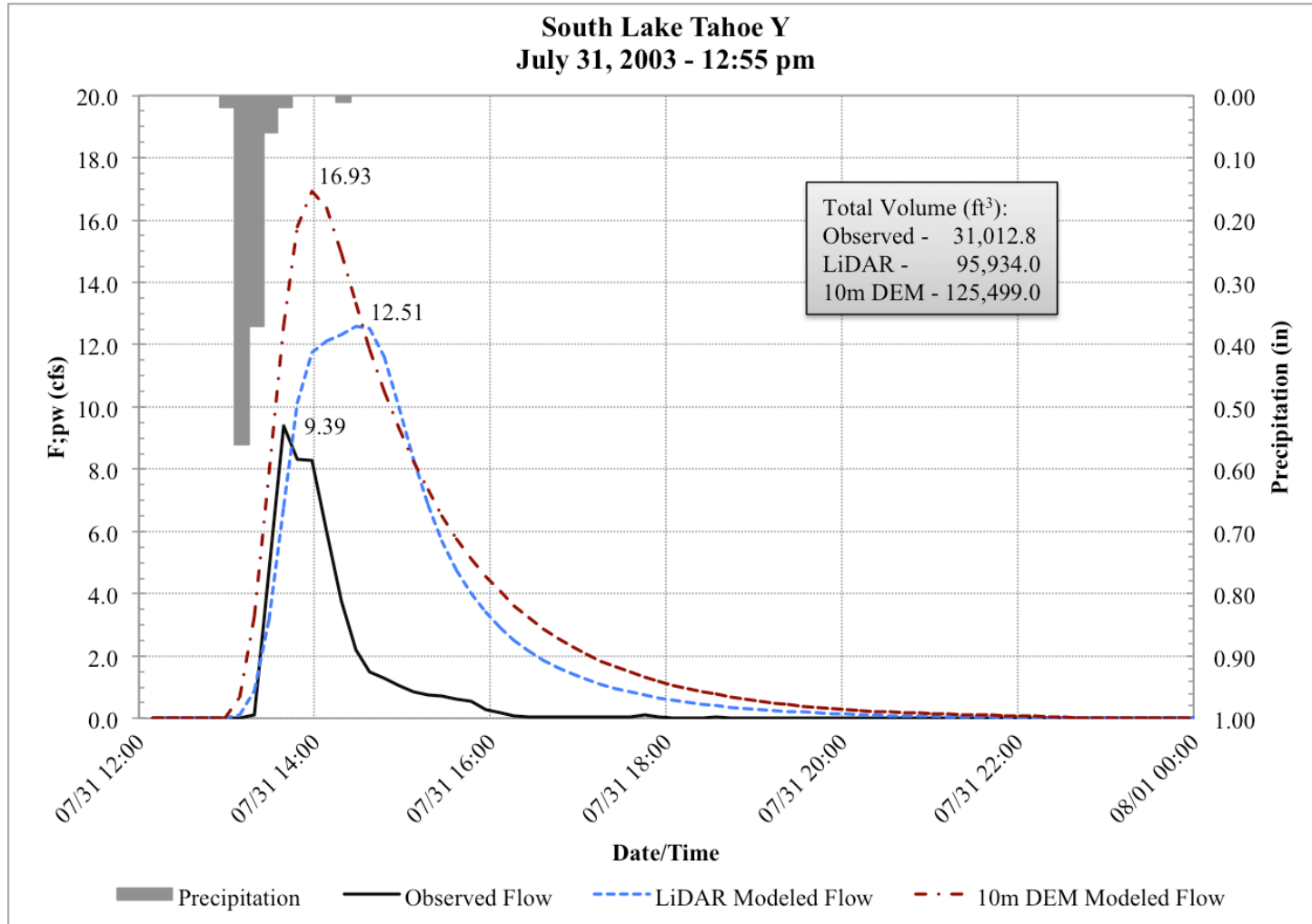


Figure C-4: Observed and HEC-HMS modeled hydrographs for storm event beginning on July 31<sup>st</sup> at 12:55 pm (group A) at site SY, located in South Lake Tahoe.

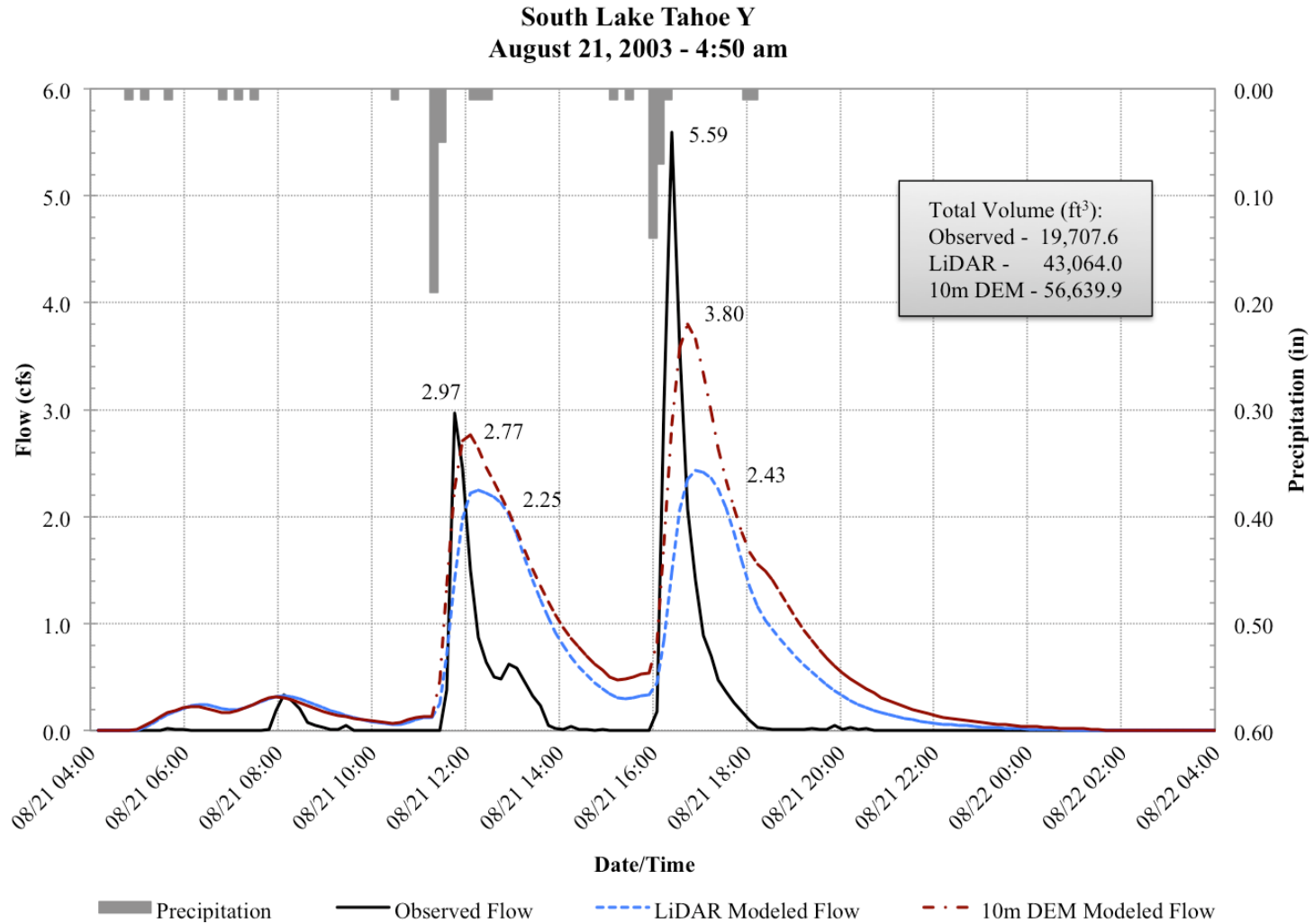


Figure C-5: Observed and HEC-HMS modeled hydrographs for the storm beginning on August 21<sup>st</sup> at 4:50 pm (group A) at site SY, located in South Lake Tahoe. Observed hydrograph has been shifted forward one hour to account for dataset error.

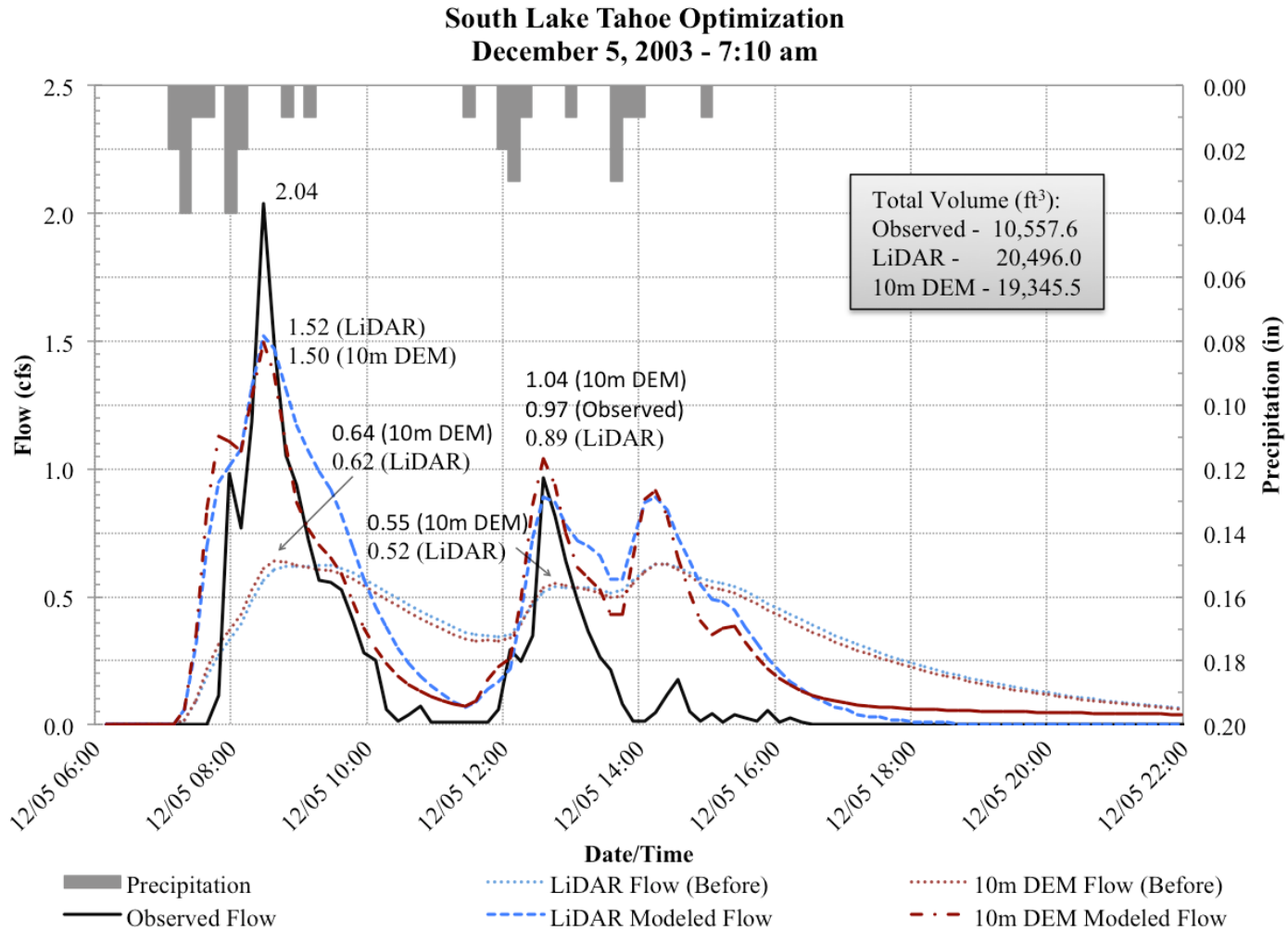


Figure C-6: Observed and HEC-HMS modeled hydrographs (before and after optimization) for the South Lake Tahoe Y (SY) optimization storm beginning on December 5<sup>th</sup> at 7:10 am (group B), located in South Lake Tahoe.

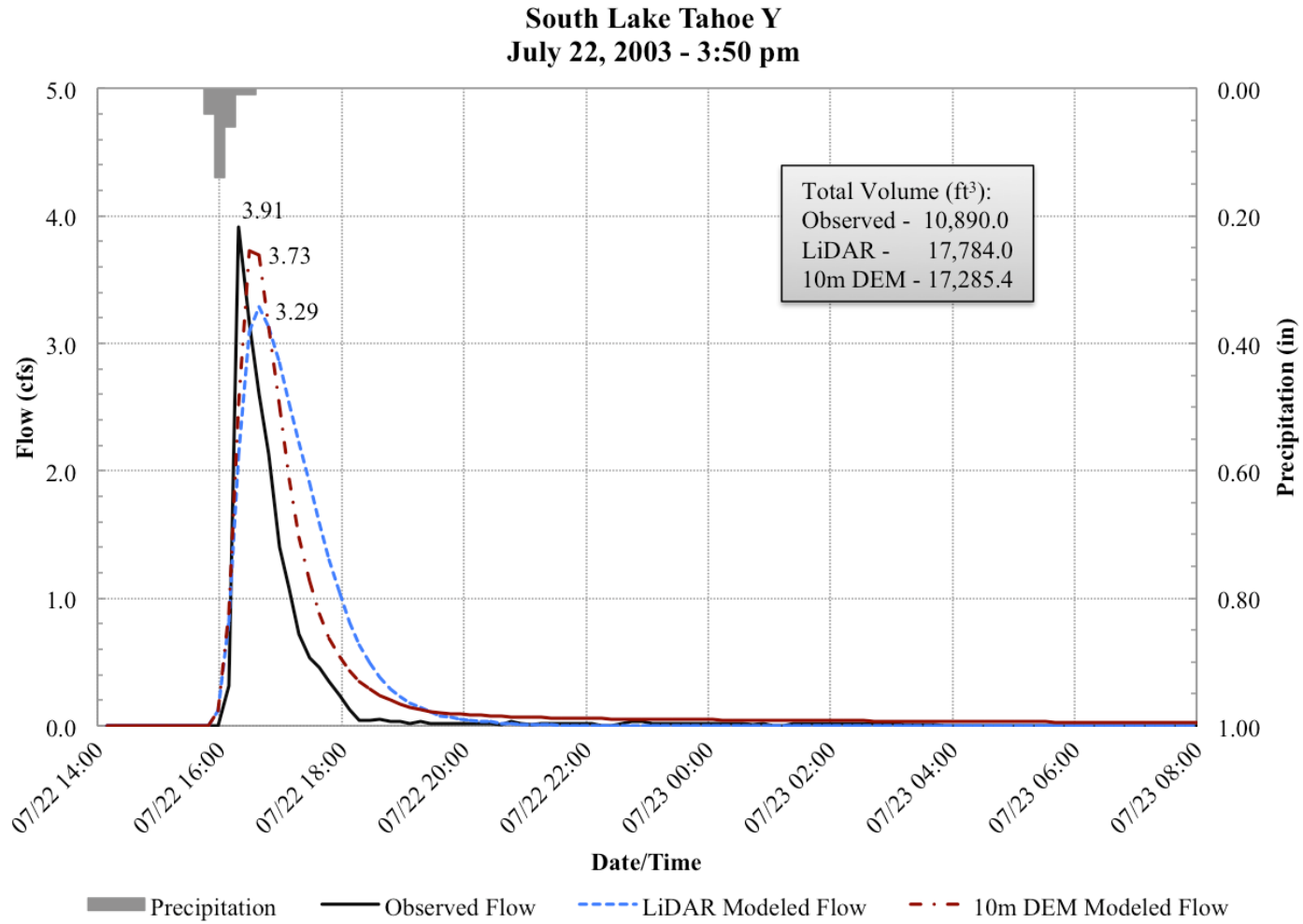


Figure C-7: Observed and HEC-HMS modeled hydrographs for the storm beginning on July 22<sup>nd</sup> at 3:50 pm (group B) at site SY, located in South Lake Tahoe.

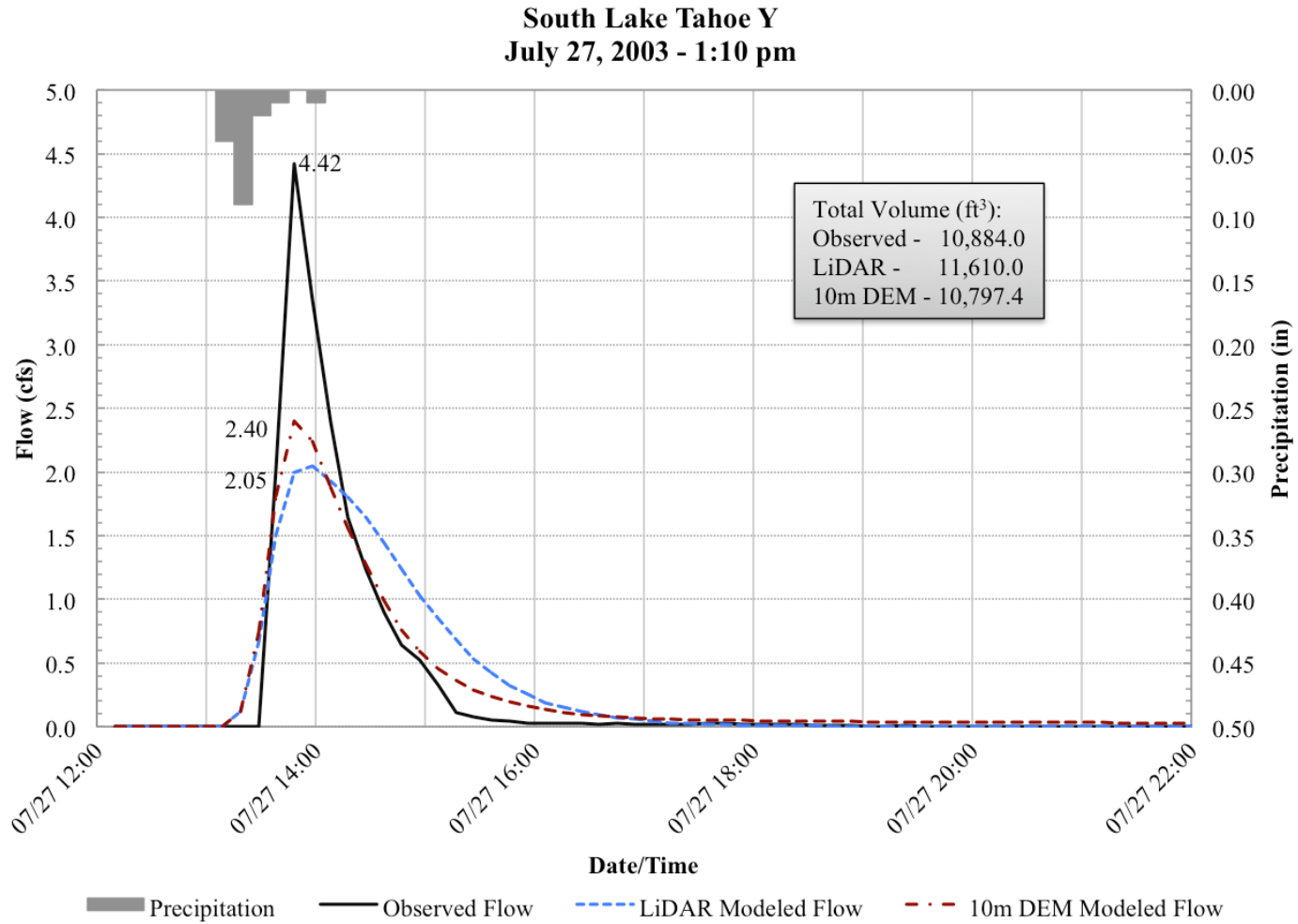


Figure C-8: Observed and HEC-HMS modeled hydrographs for the storm beginning on July 27<sup>th</sup> at 1:10 pm (group B) at site SY, located in South Lake Tahoe.

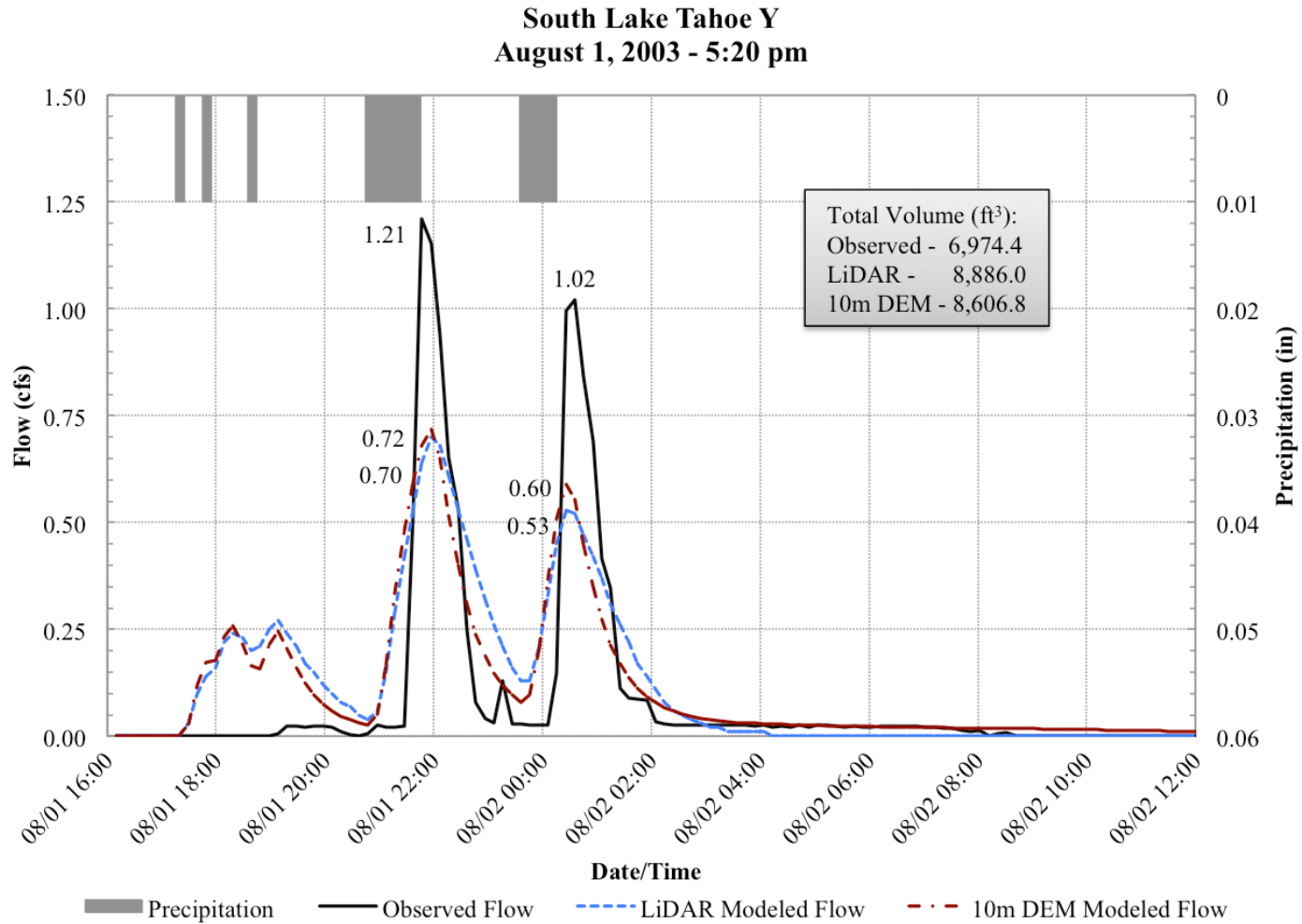


Figure C-9: Observed and HEC-HMS modeled hydrographs for the storm beginning on August 1<sup>st</sup> at 5:20 pm (group B) at site SY, located in South Lake Tahoe.

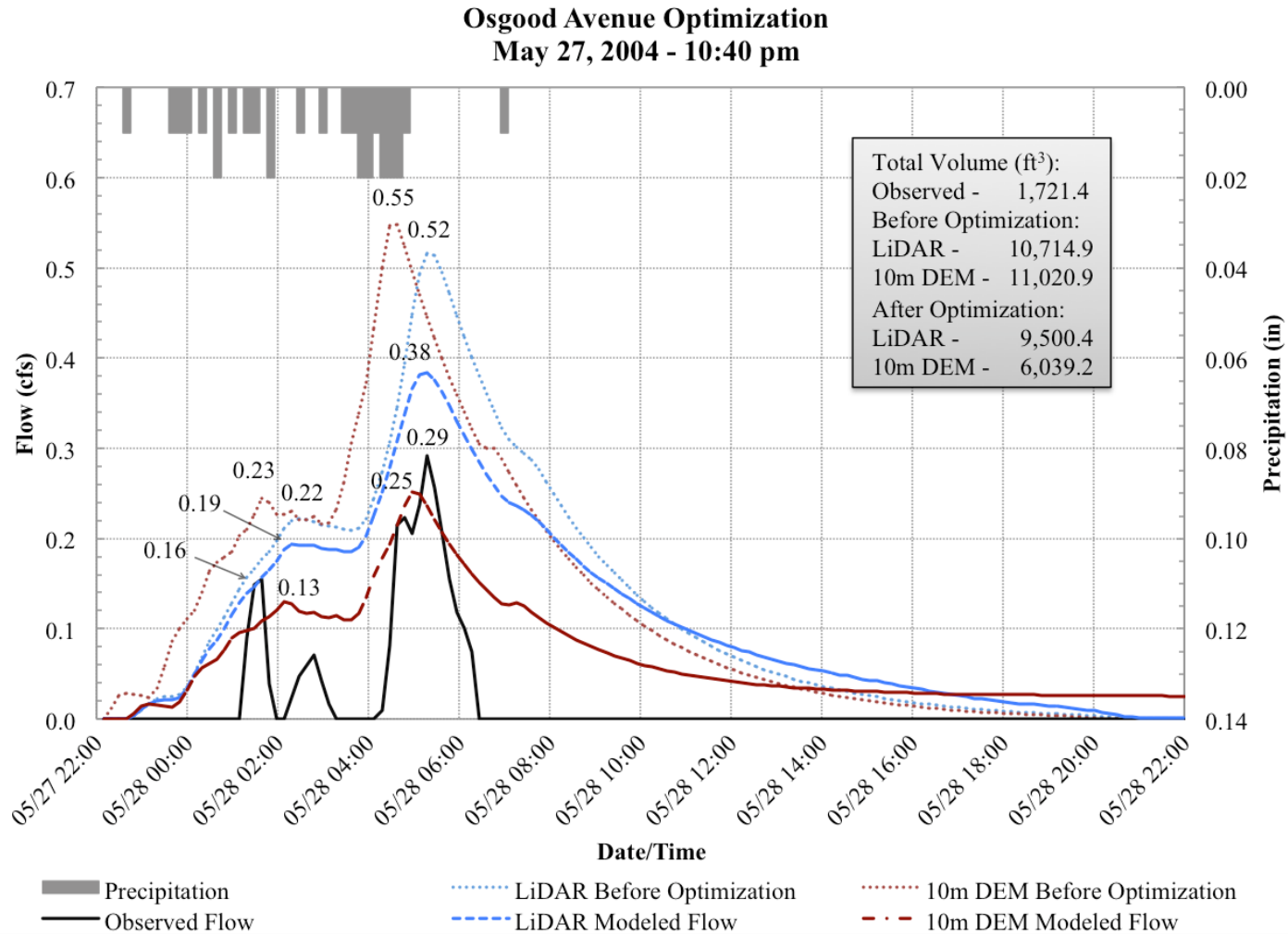


Figure C-10: Observed and HEC-HMS modeled hydrographs (before and after optimization) for the Osgood Ave (O3) optimization storm beginning on May 27<sup>th</sup> at 10:40 pm, located in South Lake Tahoe.

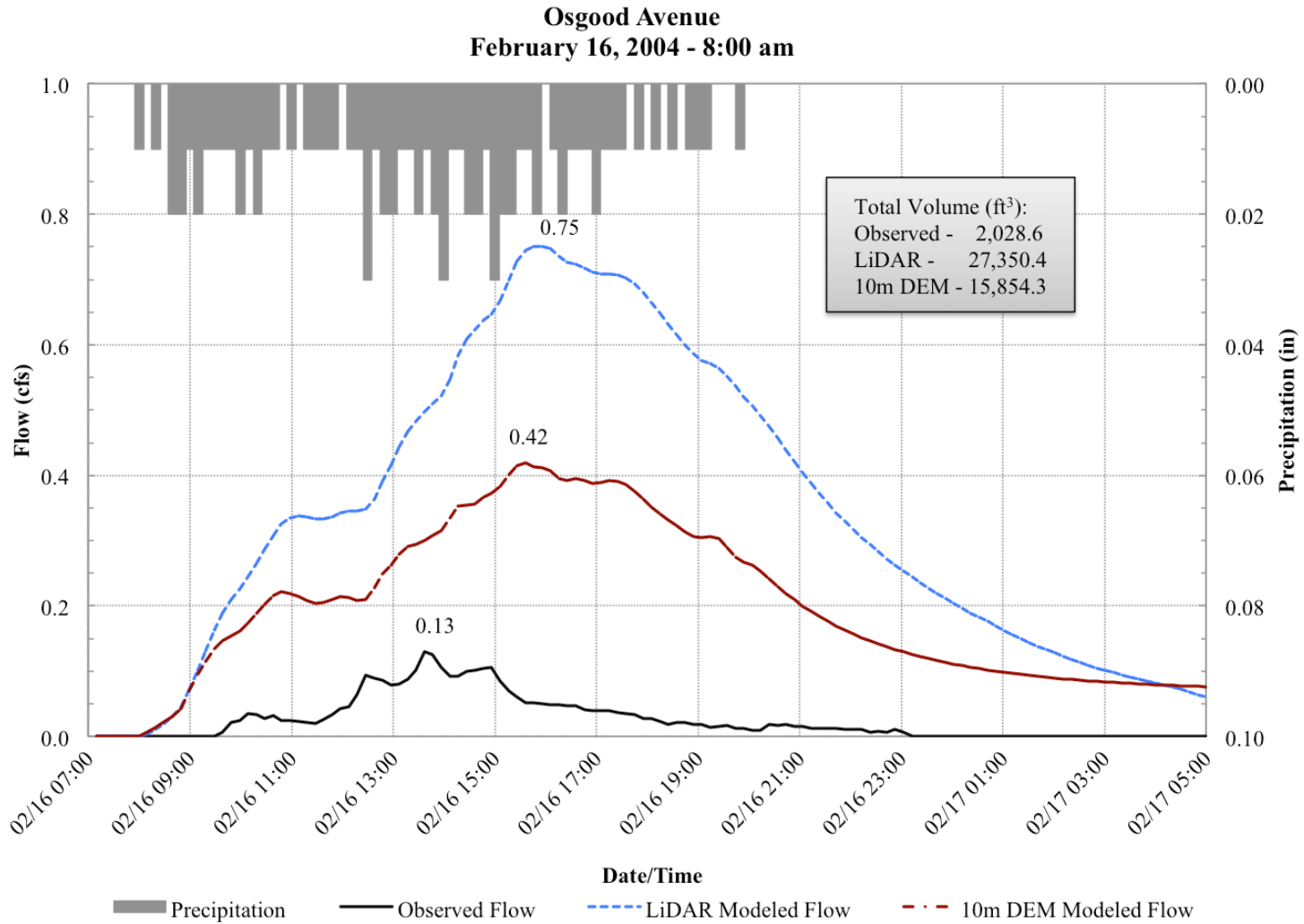


Figure C-11: Observed and HEC-HMS modeled hydrographs for the storm beginning on February 16<sup>th</sup> at 8:00 am at site O3, located in South Lake Tahoe.

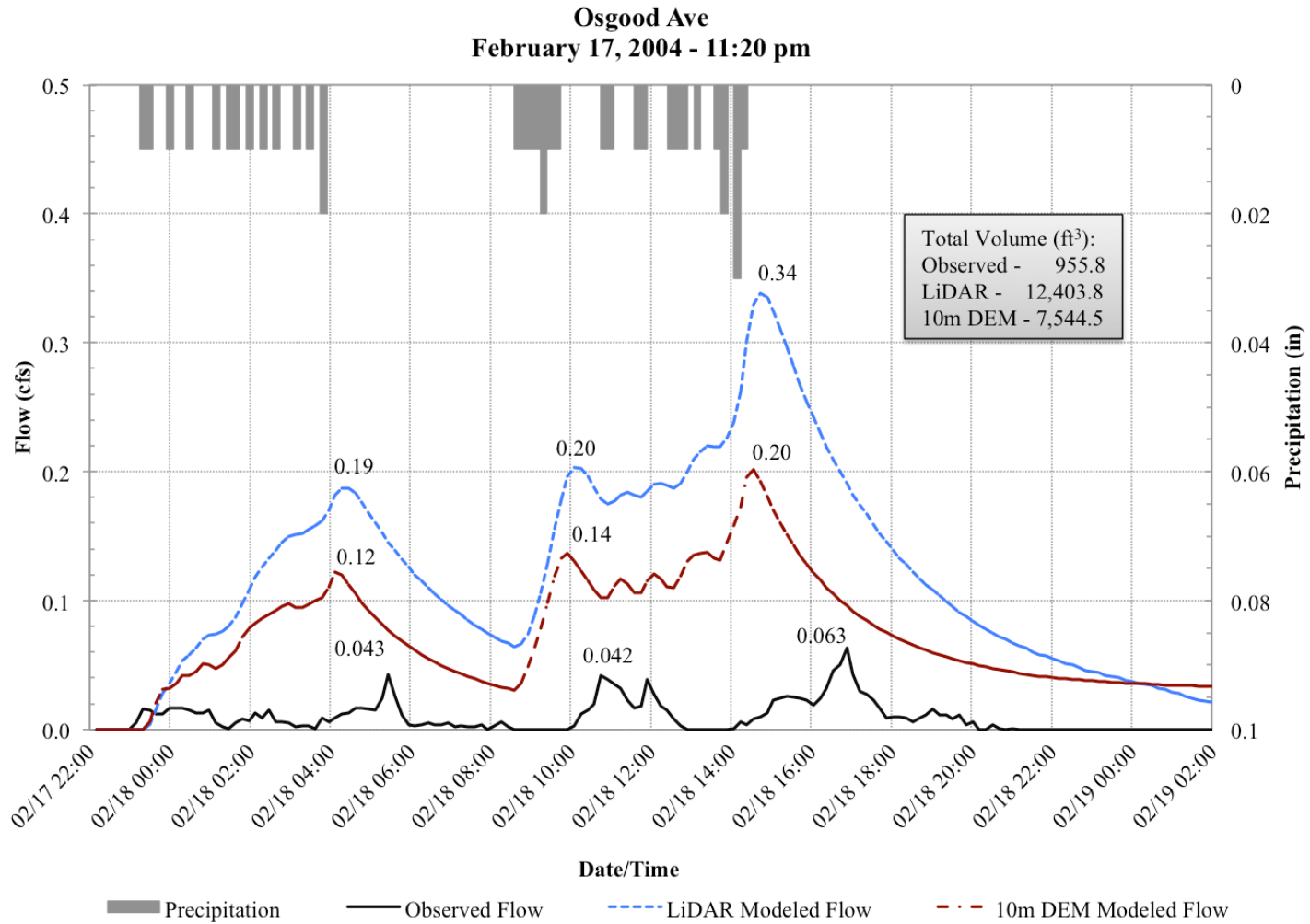


Figure C-12: Observed and HEC-HMS modeled hydrographs for the storm beginning on February 17<sup>th</sup> at 11:20 pm at site O3, located in South Lake Tahoe.

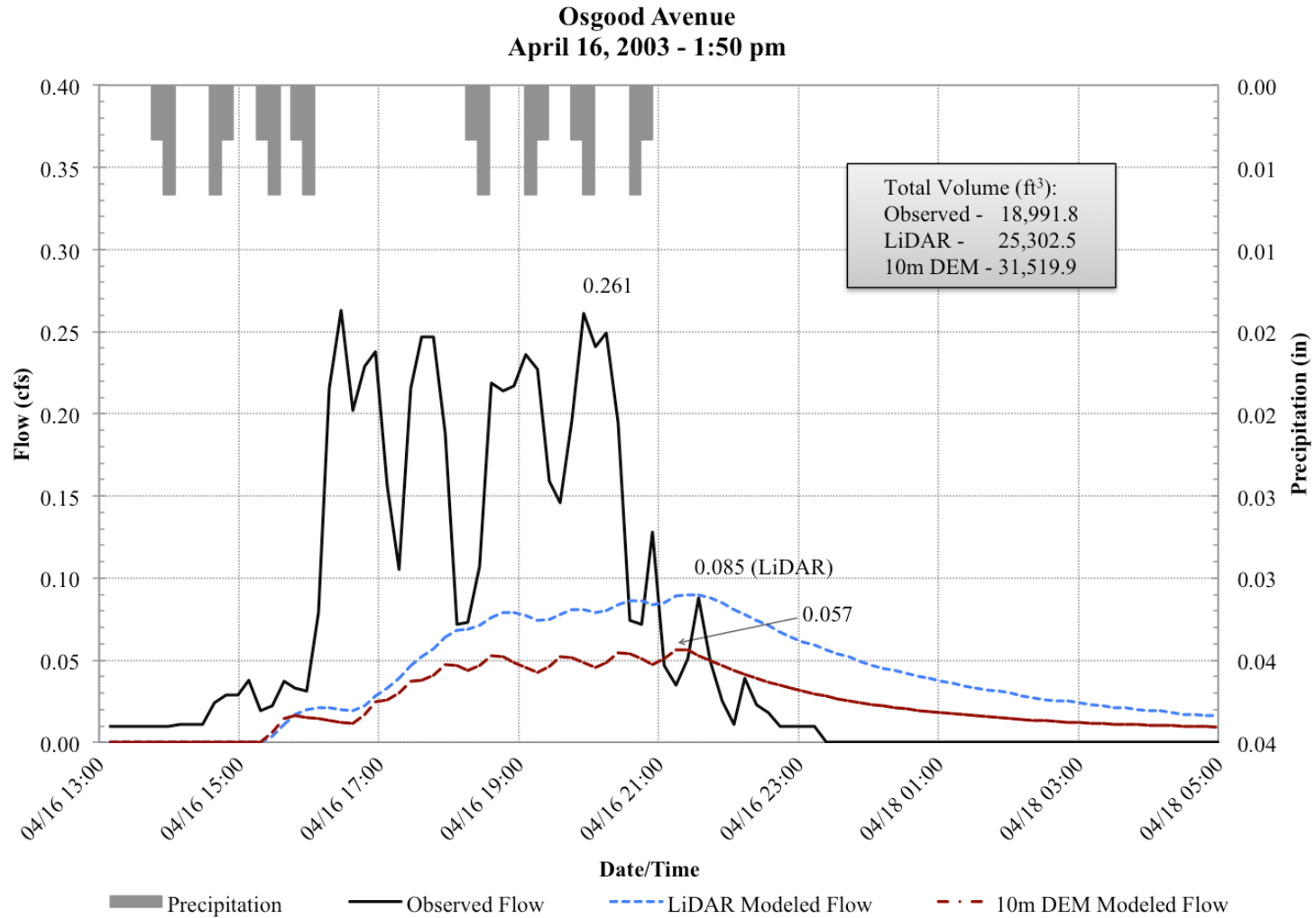


Figure C-13: Observed and HEC-HMS modeled hydrographs for the storm beginning on April 16<sup>th</sup> at 1:50 pm at site O3, located in South Lake Tahoe.

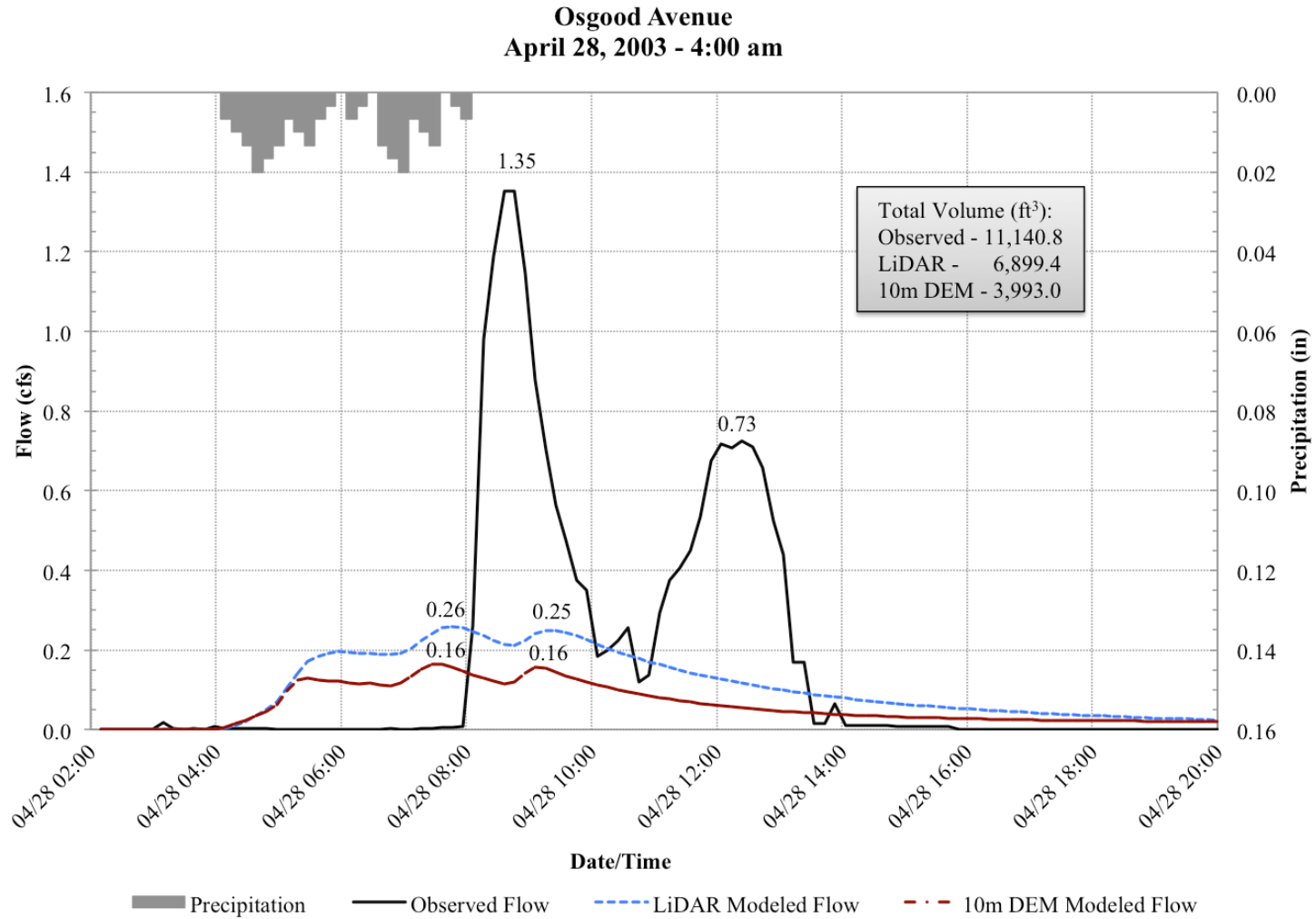


Figure C-14: Observed and HEC-HMS modeled hydrographs for the storm beginning on April 28<sup>th</sup> at 4:00 am at site O3, located in South Lake Tahoe.

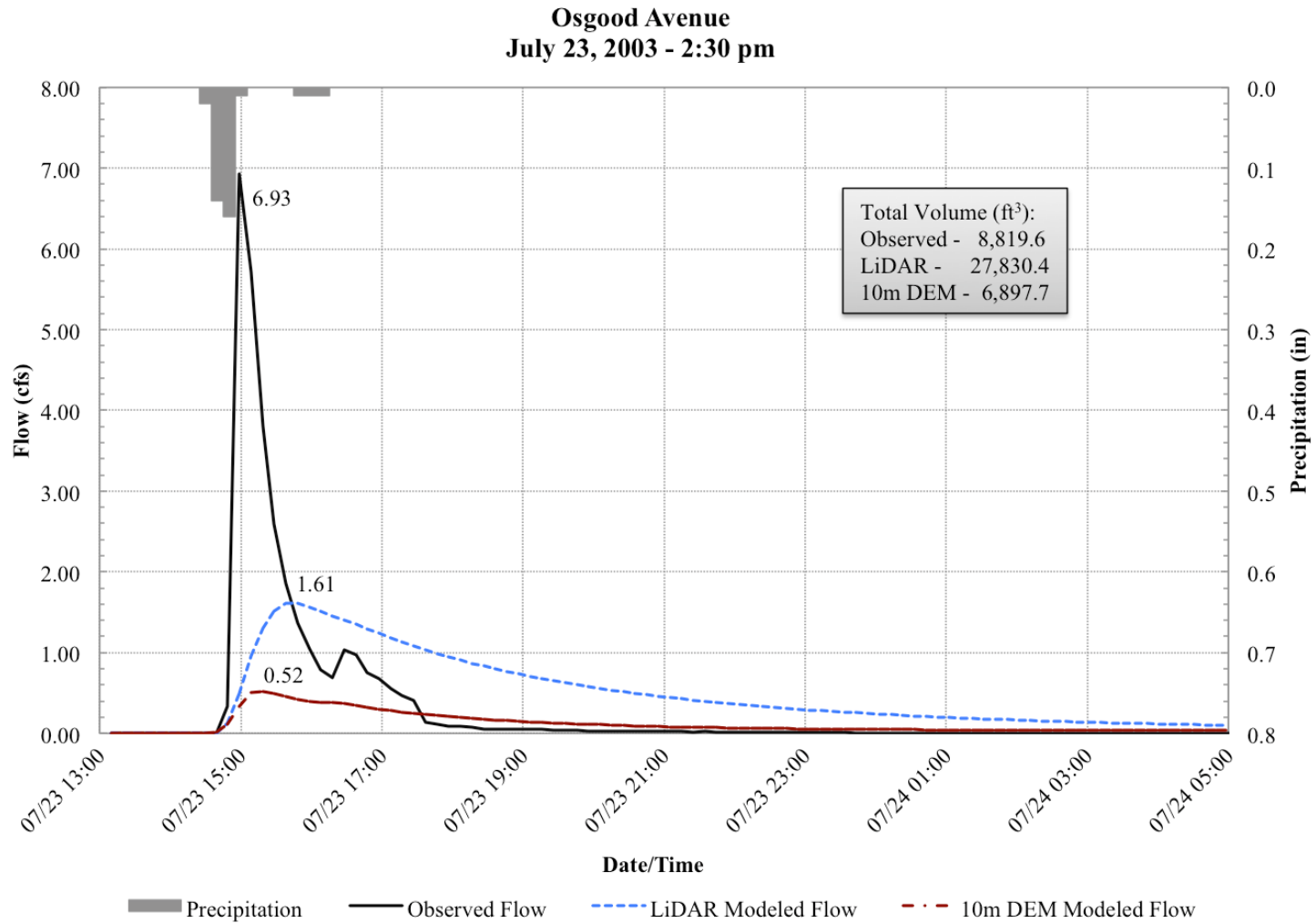


Figure C-15: Observed and HEC-HMS modeled hydrographs for the storm beginning on July 23<sup>rd</sup> at 2:30 pm at site O3, located in South Lake Tahoe.

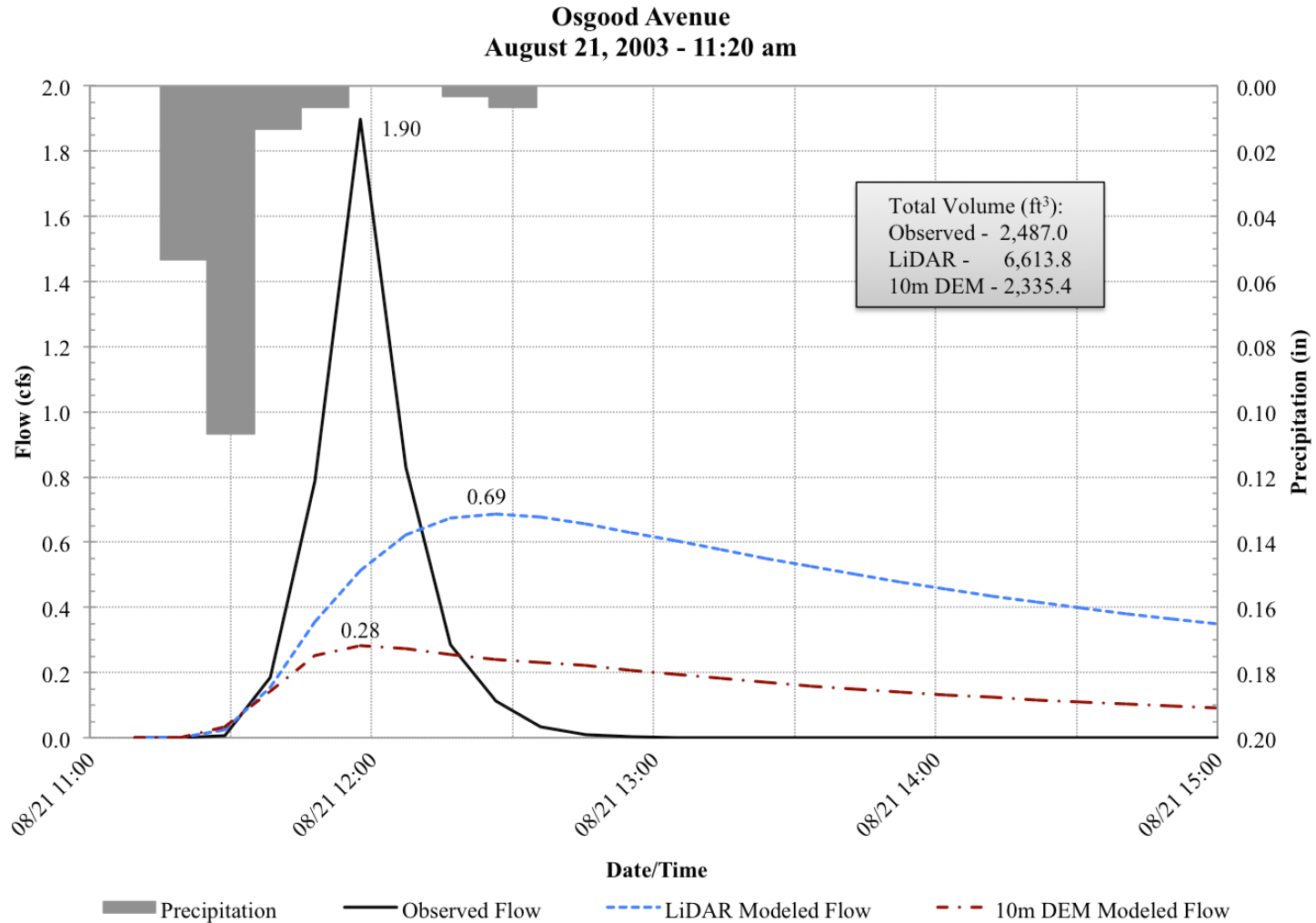


Figure C-16: Observed and HEC-HMS modeled hydrographs for the storm beginning on August 21<sup>st</sup> at 11:20 am at site O3, located in South Lake Tahoe.

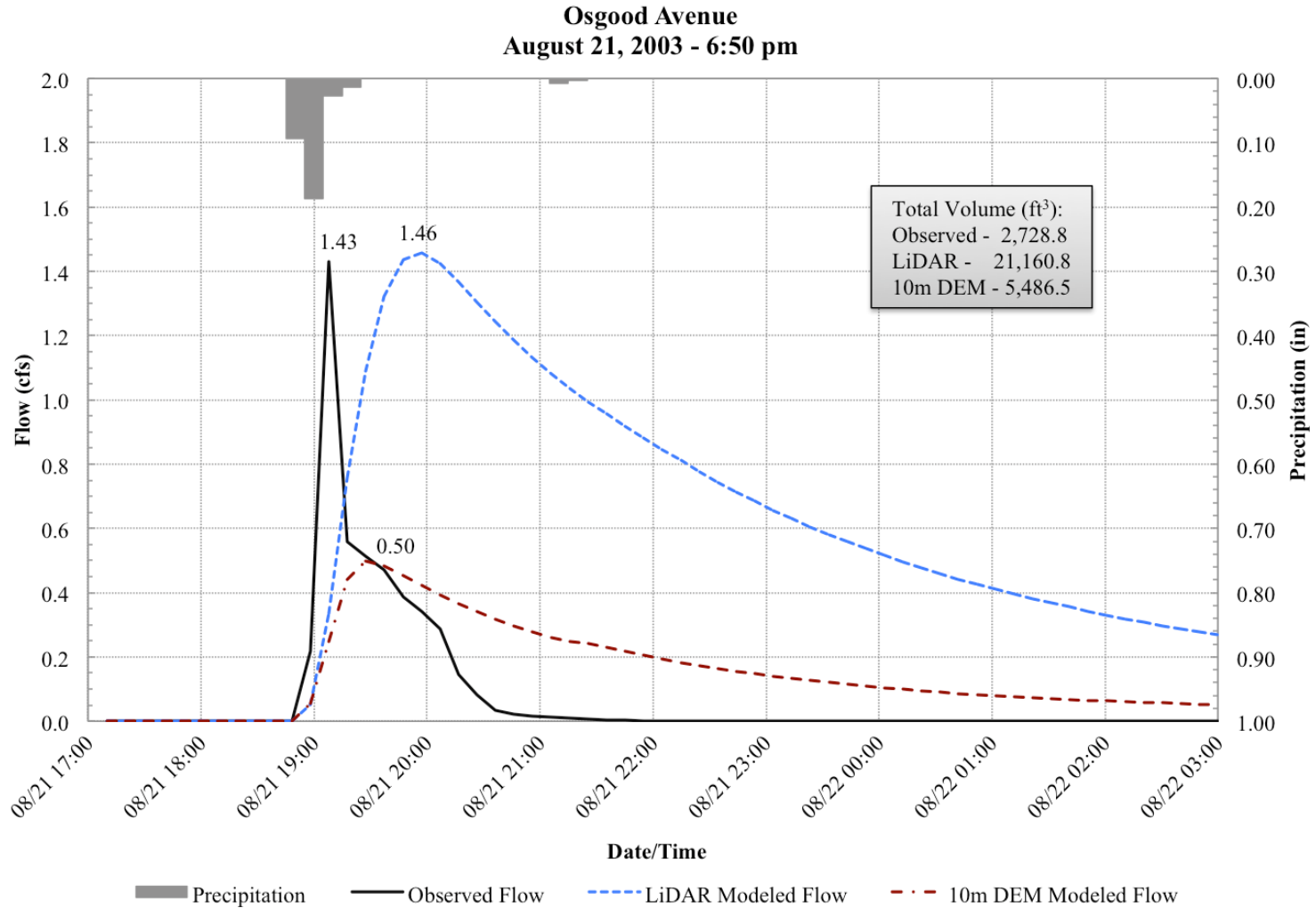


Figure C-17: Observed and HEC-HMS modeled hydrographs for the storm beginning on August 21<sup>st</sup> at 6:50 pm at site O3, located in South Lake Tahoe.

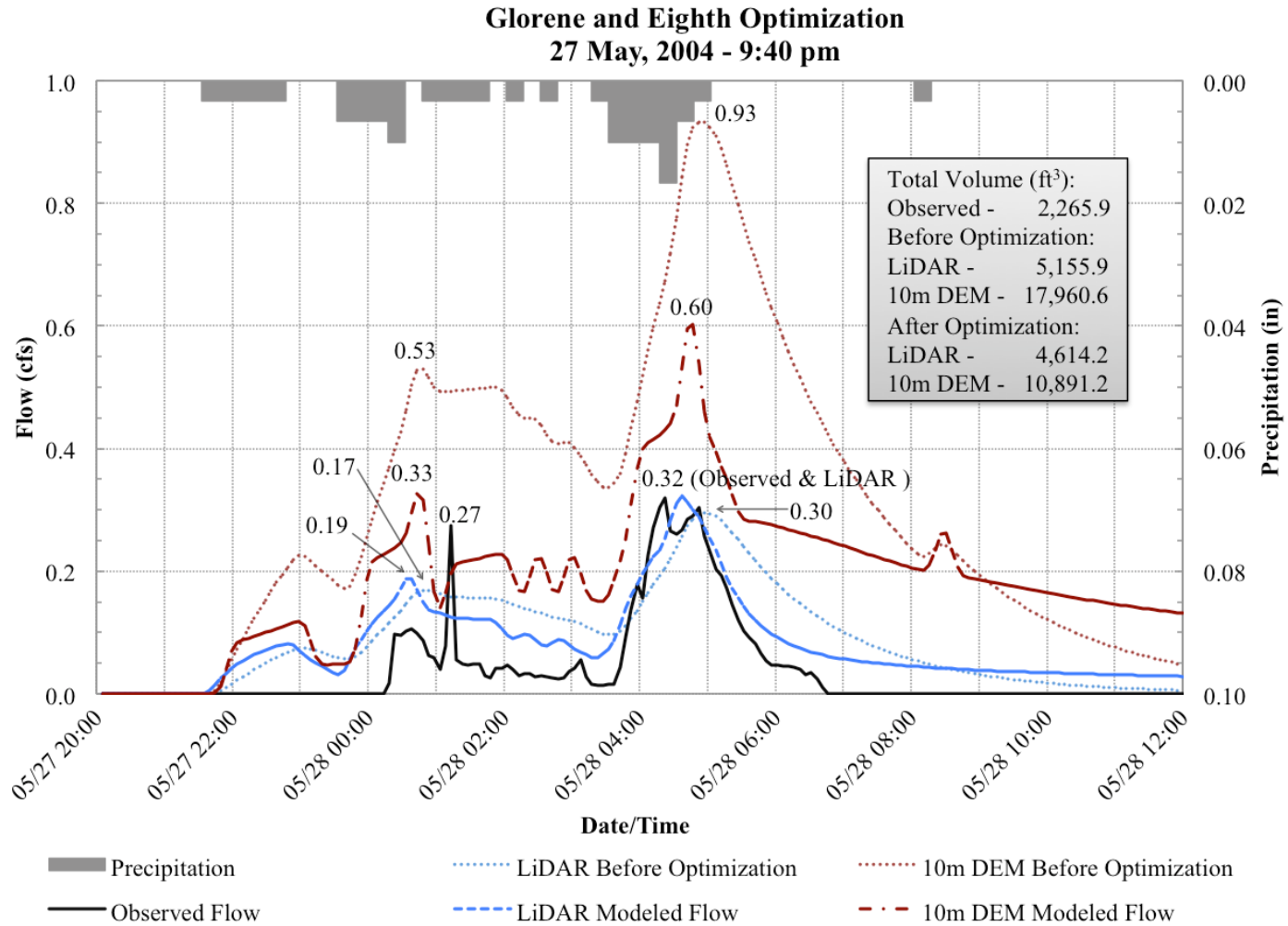


Figure C-18: Observed and HEC-HMS modeled hydrographs (before and after optimization) for the Glorene and Eighth (GE) optimization storm beginning on May 27<sup>th</sup> at 9:40 pm, located in South Lake Tahoe.

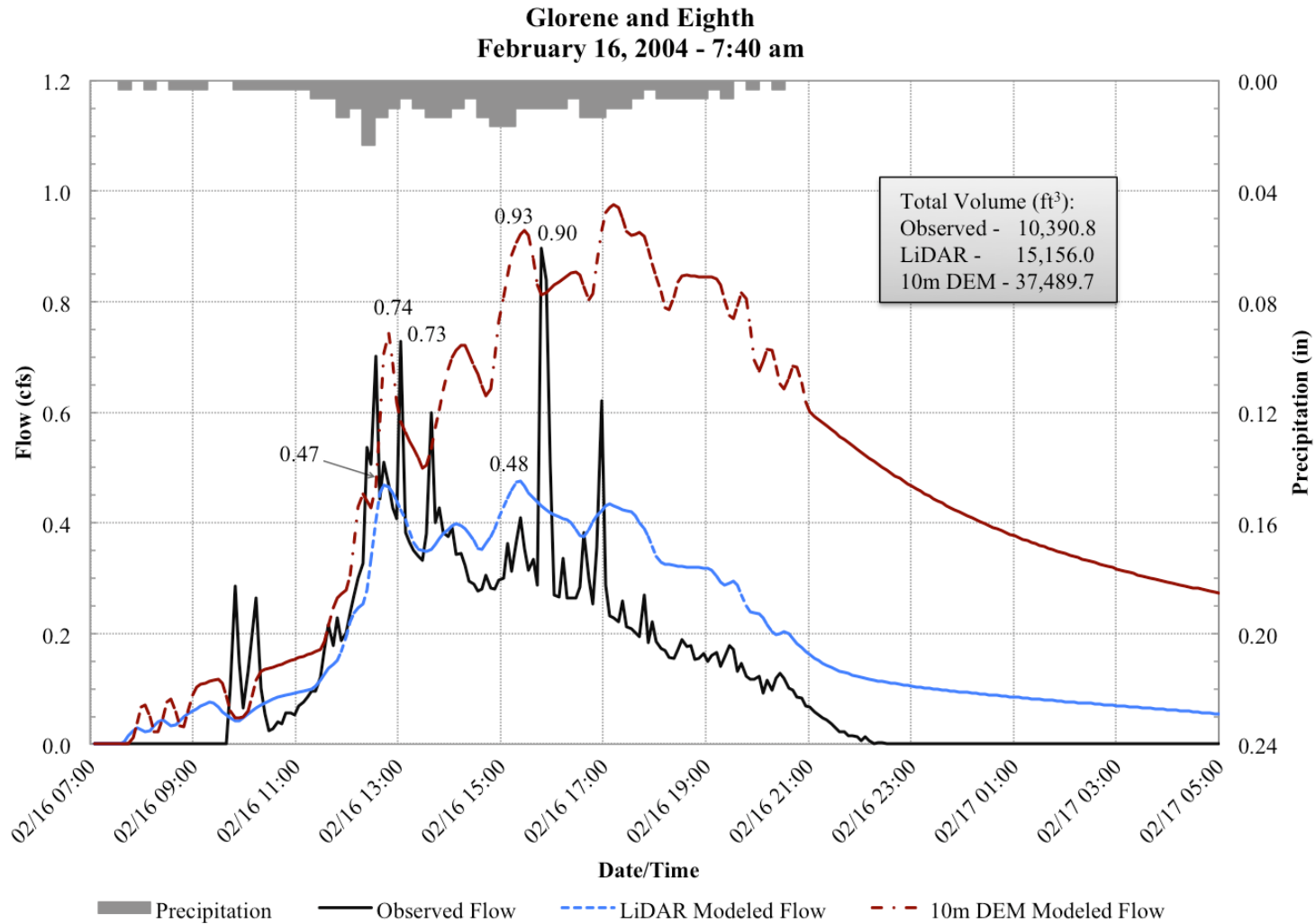


Figure C-19: Observed and HEC-HMS modeled hydrographs for the storm beginning on February 16<sup>th</sup> at 7:40 am at site GE, located in South Lake Tahoe.

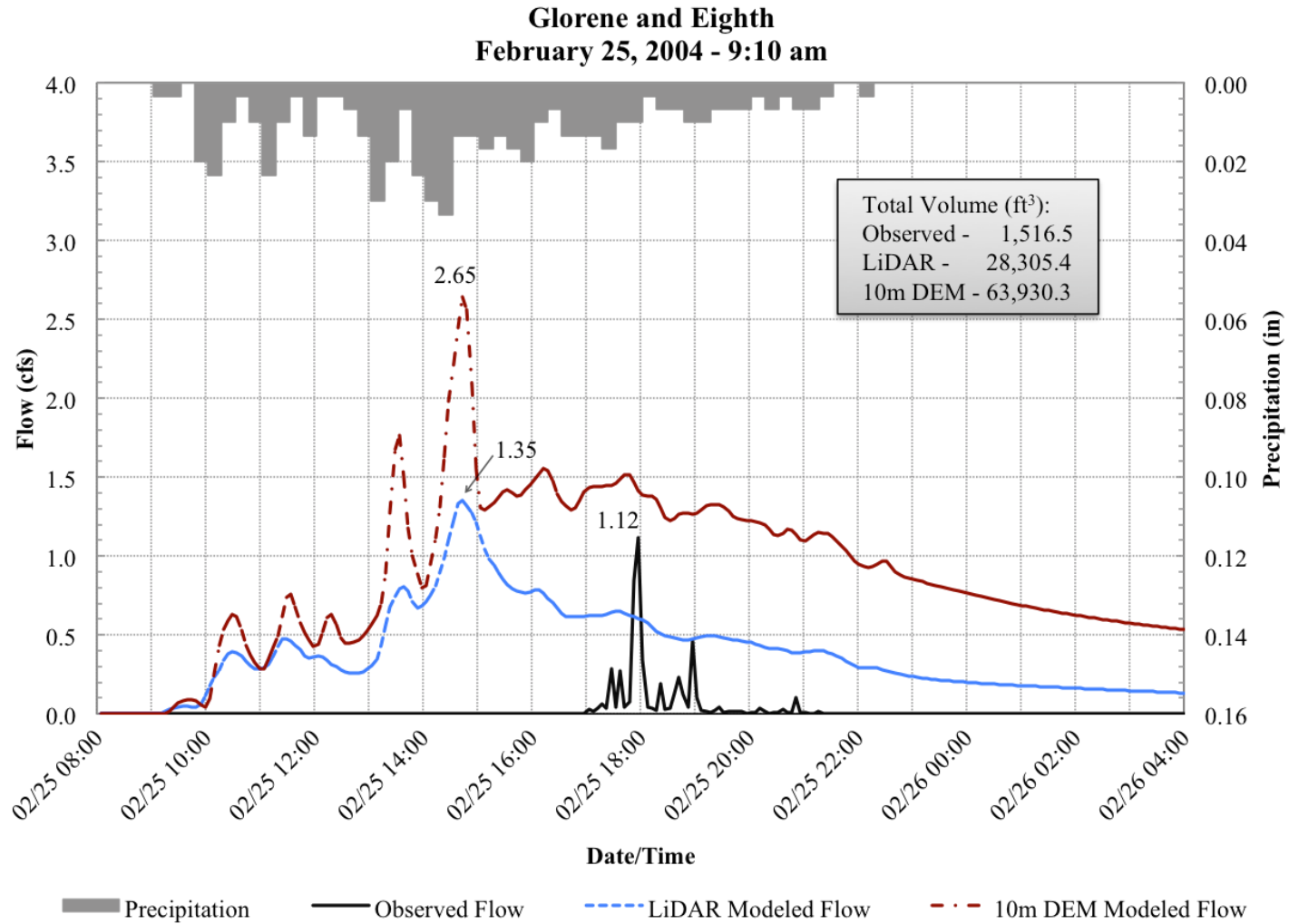


Figure C-20: Observed and HEC-HMS modeled hydrographs for the storm beginning on February 25<sup>th</sup> at 9:10 am at site GE, located in South Lake Tahoe.

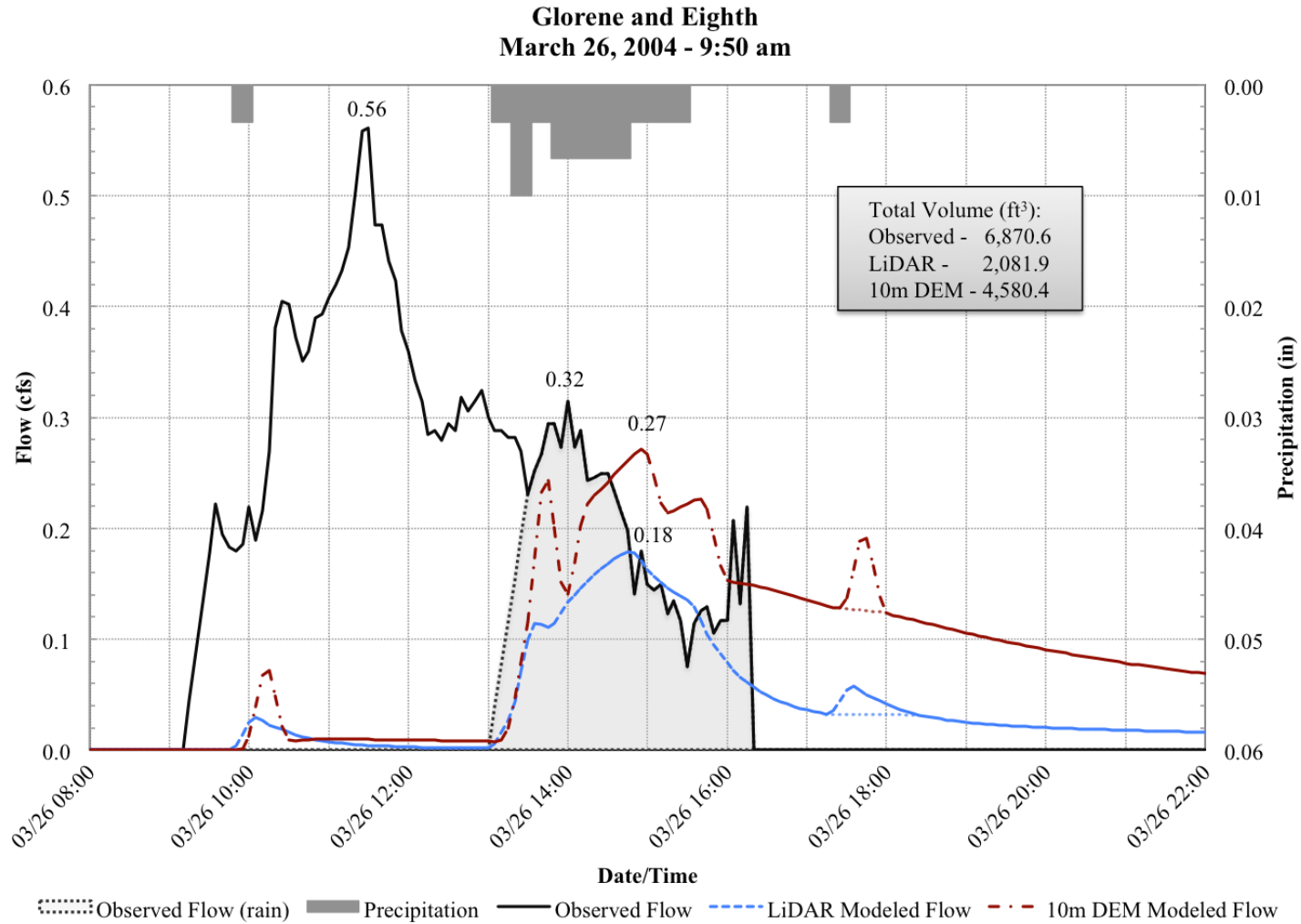


Figure C-21: Observed and HEC-HMS modeled hydrographs for the storm beginning on March 26<sup>th</sup> at 9:50 am at site GE, located in South Lake Tahoe.

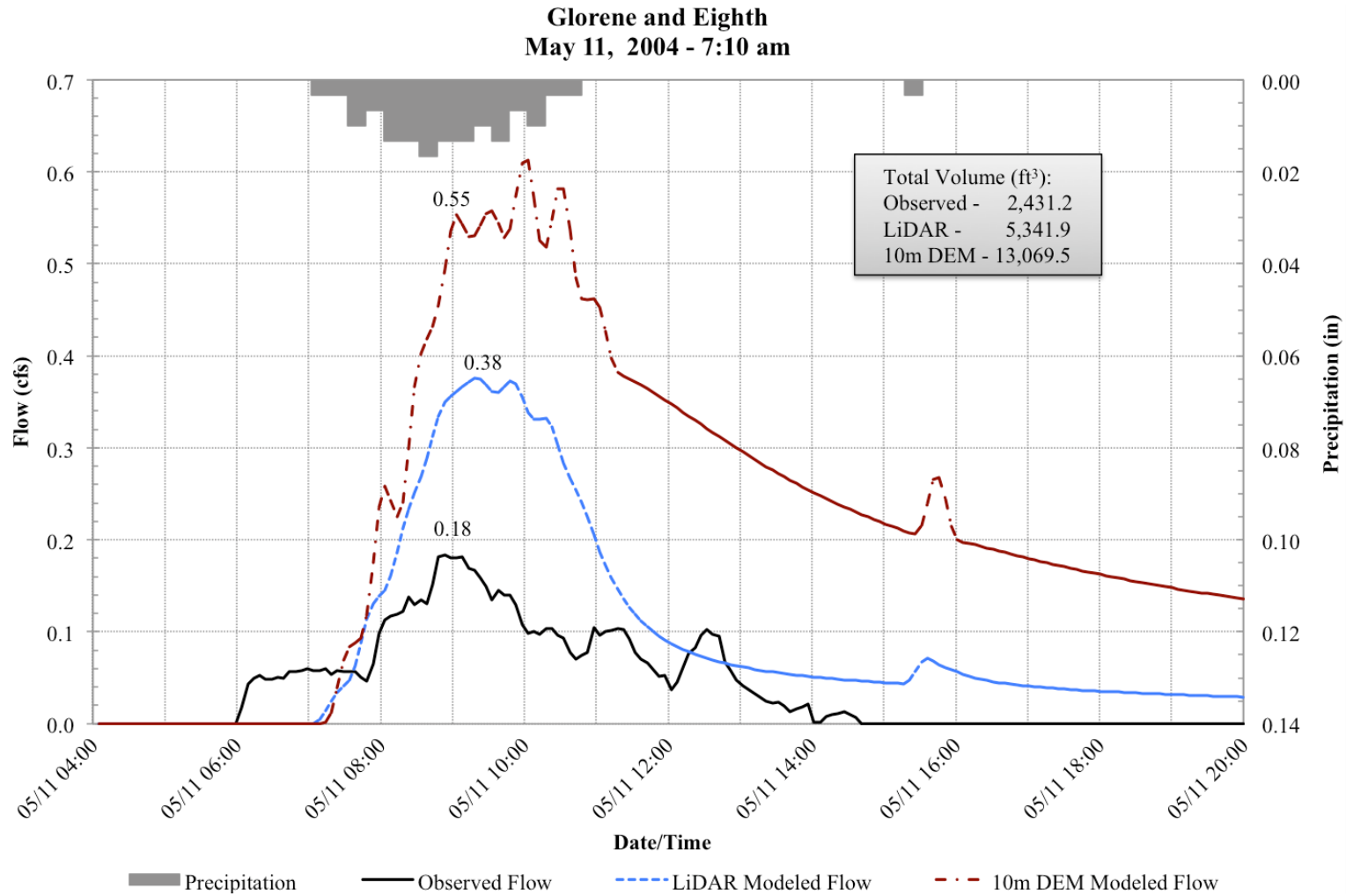


Figure C-22: Observed and HEC-HMS modeled hydrographs for the storm beginning on May 11<sup>th</sup> at 7:10 am at site GE, located in South Lake Tahoe.